Isogeometric boundary element methods for linear elastic fracture mechanics

Xuan PENG

supervisors:

Prof. Stéphane P.A. BORDAS

Dr. Pierre KERFRIDEN

A thesis submitted in fulfillment of the requirements

for the degree of Doctor of Philosophy

in the

Advanced Materials and Computational Mechanics Group

Cardiff School of Engineering

Cardiff, Wales, United Kingdom

July 3, 2016

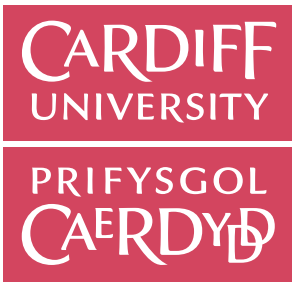

Declaration

This work has not previously been accepted in substance for any degree and is not concurrently submitted in candidature for any degree.

Signed ..... (Candidate) Date .....

STATEMENT 1

This thesis is being submitted in partial fulfilment of the requirements for the degree of PhD.

Signed ..... (Candidate) Date .....

STATEMENT 2

This thesis is the result of my own independent work/investigation, except where otherwise stated. Other sources are acknowledged by explicit references.

Signed ..... (Candidate) Date .....

STATEMENT 3

I hereby give consent for my thesis, if accepted, to be available for photocopying and for inter-library loan, and for the title and summary to be made available to outside organisations.

Signed ..... (Candidate) Date .....

Summary

We develop in this work a procedure for obtaining the fatigue life of complex structures directly from Computer-Aided Design (CAD) data, without any mesh generation or regeneration as the cracks evolve. The method relies on a standard isogeometric boundary element method (IGABEM) where the same basis functions are used to both describe the geometry of the component and approximate the displacement and traction fields. The contributions of this work include:

(1) Dual boundary integral equations have been applied to model 2D/3D fracture problems in the framework of IGA and that such simulations require no meshing or remeshing in the conventional sense;

(2) Graded knot insertion and partition of unity enrichment have been used to capture the stress singularity around the crack tip. The contour-integral based methods and the virtual crack closure integral method are adopted to extract stress intensity factors in the framework of IGABEM;

(3) Modifications on the singularity subtraction technique for (hyper-)singular integration are proposed to enhance the quadrature on distorted elements which commonly arise in IGA;

(4) A NURBS-based geometry modification algorithm is developed to simulate fatigue crack growth in 2D/3D. smooth crack trajectory and crack front are obtained;

(5) An implementation on trimmed NURBS is realized based on a localized double mapping method to perform the quadrature on trimmed elements. A phantom element method is subsequently proposed to model the surface crack (breaking crack) problem and the displacement discontinuity can be introduced without any reparametrization on the original patch.

Acknowledgements

The financial support of the Framework Programme 7 Initial Training Network Funding under grant number 289361 'Integrating Numerical Simulation and Geometric Design Technology' (INSIST) is gratefully acknowledged.

I would first like to acknowledge my supervisor, Prof. Stéphane P. A. Bordas, who is a brilliant mentor, motivated colleague and one of my best friends, for his guidance and suggestions on my research, his encouragement and help when I got stuck in programming bugs and his kind support during my illness.

I would also like to express my deep thank to: Dr. Elena Atroshchenko, who gives me much assistance in BEM from mathematical aspects. Without her help, I cannot image how I can get through the tough time during my PhD; Dr. Pierre Kerfriden, who has expertise in many advanced topics of FEM. Working with him broadens my knowledge within this field. Dr. Robert Simpson, who gives me the first knowledge on BEM and IGA. I really enjoy the talk with him on research although the time we worked together is so short; Dr. Haojie Lian, who shared almost the same research topic as me. Discussion with him gives me many useful tips on IGABEM and greatly advanced my learning process. He is also a good Chinese friend and gives much care to my life during the 4 years at Cardiff. Dr. Sivakumar Kulasegaram for his kind help in XFEM; Prof. Gang Xu for the wonderful discussion in CAD geometry and PHT splines. Prof. Sheng-Chuan Wu, who was my supervisor in China before I came to UK. He first introduced me into the area of computational mechanics and provided a lot of help for me to study abroad. Besides, many thanks will be given to my friends in the

group for their help in everything: Dr. Ahmad Akabari, Daniel Alves Paladim, Dr. Danas Sutula, Dr. Olivier Goury, Dr. Chang-Kye Lee, Dr. Octavio Andrés González-Estrada, Dr. Claire Heaney, Dr. Nguyen Vinh Phu, Dr. Chi Hoang, Xiaohan Du, Peng Yu, Pedro Bonilla, as well as my colleagues in the INSIST project. The time spent with them is quite valuable to me.

At last, I would like to express my gratitude to my parents and my brother. It is their sustained love and support that give me persistence to finish the PhD project.

List of publications

Part of the presented work in this thesis has been submitted or presented in the following journal papers and conference.

1. X Peng, E Atroshchenko, P Kerfriden and S P A Bordas. Isogeometric boundary element methods for three dimensional static fracture and fatigue crack growth. *Computer methods in Applied Mechanics and Engineering*, 2016, accepted.

2. X Peng, E Atroshchenko, P Kerfriden and S P A Bordas. Linear elastic fracture simulation directly from CAD: 2D NURBS-based implementation and role of tip enrichment. *International Journal of Fracture*, 2016, accepted.

3. X Peng, S Kulasegaram, S P A Bordas and S C Wu. An extended finite element method (XFEM) for linear elastic fracture with smooth nodal stress. *Computers & Structures*, 2015, submitted.

4. X Peng, S P A Bordas, S Natarajan. Smooth nodal stresses in the XFEM for crack propagation simulations. *Thematic conferences of the European Community in Computational Methods in Applied Sciences (ECCOMAS): XFEM 2013*, Lyon, France, 2013.

5. X Peng, E Atroshchenko, R N Simpson, S P A Bordas and S Kulasegaram. A two-dimensional isogeometric boundary element method for linear elastic fracture. *2rd International Conference on Isogeometric Analysis (IGA 2014)*, Austin, Texas, USA, 2014.

6. X Peng, E Atroshchenko and S P A Bordas. Damage tolerance assessment directly from CAD: (extended) isogeometric boundary element methods (XIGABEM). *6th International Conference on Advanced Computational Methods in Engineering (ACOMEN 2014)*, Ghent, Belgium, 2014.

7. X Peng, E Atroshchenko, R N Simpson, S Kulasegaram and S P A Bordas. Crack growth analysis by a NURBS-based isogeometric boundary element

method. *11th World Congress on Computational Mechanics (WCCM2014)*, Barcelona, Spain, 2014.

Contents

List of Figures

List of Tables

Chapter 1

Introduction

1.1 Computational fracture models

The numerical simulation of crack propagation and the prediction of fatigue life for engineering structures plays an important role in modern industrial design and remains a difficult problems. Various computational models have been proposed to fulfill the analysis of brittle fracture.

1.1.1 Continuum damage mechanics

One way to model fracture in the continuum-based methods is related to damage mechanics, where the failure occurs with the degradation of solids in the stress concentrated area due to the micro-defects of the material and can be scaled by introducing a internal damage variable into the constitutive relation of the material, thus no existing or predefined crack surfaces are needed. A simple damage model of fracture, however, suffers from spurious localization when it comes into numerical implementation. Some regularity treatments are thus needed and several methods were developed subsequently. For example, the non-local model [1][2], where the damage variable is calculated through an integration of the strain over a certain area; the gradient-based method [3], where the spatial derivative of the damage variable or the gradient of deformation, are introduced. Moës *et al* proposed a thick level set (TLS) approach to model damage growth [4]. In this method, the damage zone is separated by a level set function and the damage variable is an explicit set of the level set. This method bypassed several

difficulties in the gradient-based methods and is promising to bridge the nucleation of micro-cracks from damage mechanics to macro-propagation of the crack.

1.1.2 Linear elastic fracture mechanics and cohesive fracture

The discrete approaches or enrichment methods [5] introduce the crack (displacement discontinuity) directly into the fracture model. These methods rely on a crack surface tracking algorithm and will be further reviewed in subsequent sections. Based on the assumption of linear elastic fracture mechanics (LEFM), the discrete/enrichment approach has been applied into industrial structure design maturely. The LEFM-based analysis, also known as the damage tolerance assessment [6], considers the intensity of structure/mechanical part which allows cracks exist (crack size usually greater than 1 mm which can be given by the non-destructive detection) in the design procedure, where the crack is inserted manually into the stress concentrated area spot by stress analysis. For a working part under cyclic loading condition, if cracks are detected in the inspection routine, the rest serving life can be estimated by the crack propagation analysis coupled with fatigue rule such as the Paris law. For some material such as the concrete, the fracture process zone is non-eligible compared to the crack size, thus the linear elasticity or small field yielding assumption in LEFM fails. Then the cohesive crack model is adopted, where a displacement-traction relation is used in the cohesive zone on the crack surface. The cohesive crack model was well developed in 2D [7][8][9][10] and its extension to 3D is available in the framework of extended finite element method [11].

1.1.3 Variational fracture approach

The conventional crack growth analysis relies on the Griffith theory, where the crack will propagate once the crack driving force (stress intensity factors or J integral) exceeds the fracture energy needed for the formation of the new crack surface and this procedure is considered as a postprocess of the

finite element analysis. The variation fracture approach [12] was proposed by taking the fracture energy into the energy functional, thus the crack advance increment and angle become variables of this functional and can be obtained by the global energy minimization. The variational approach provides a fully automated way to propagate the crack and has been realized in 2D [13][14] and 3D [15][16]. The phase field method [17][18][19] provides a way to model fracture in continua by using a phase field variable to describe the crack surface implicitly. Similar to the discrete variational methods, cracks nucleate automatically when the stress reaches the critical value and the parameters for the propagation of cracks can also be found by solving the system of equations.

1.2 key challenges in linear elastic fracture mechanics

Although the LEFM appears simpler, it presents a number of unique challenges to the modelers. The first difficulty is the accurate computation of the crack driving force, namely the stress intensity factors (SIFs). The second difficulty is that the mesh used for stress analysis and hence for the detection of 'sensitive' regions in the component, where initial flaws are introduced, is typically at least one order of magnitude too coarse to provide quality SIFs. The third difficulty lies in the geometrical complexity of the domain which, if the predicted fatigue life is deemed inadequate, must be redesigned. For each new design, and for each crack configuration, a new mesh typically needs to be generated, not only to conform to the new chosen geometry, but also to properly resolve stresses in the vicinity of the crack tip (front). The requirement of reproducing the large gradients (singularities in the case of LEFM, combined with that of capturing discontinuities as they evolve implies that relatively fine meshes must be continuously regenerated as cracks propagate. Fourth, reliable and general crack growth laws remain elusive. For LEFM, the Paris law or its cousins are commonly used. Such laws compute the increment in crack advance as a proportional to some power $m(m > 1)$ of the SIFs. A small error ε in the SIFs thus leads

to an accumulated error scaling as $m\varepsilon$ at *each* of the tens of thousands of crack growth steps required for each simulation. This raises more demanding requirements on accuracy of the SIFs calculation.

1.3 Existing numerical methods for linear elastic fracture modeling

The finite element method (FEM) can be applied to simulate the crack propagation directly with certain adaptive re-meshing operation [20][21][22]. Some software packages have been developed based on this idea [23][24] and a review paper can be found in [25]. Nevertheless, meshing and re-meshing becomes one of the most human-intensive tasks for multi-cracks or for very complicated components as the complexity is increased due to the presence of cracks. Most, if not all, commercial codes do not offer completely automatic re-meshing approach for industrial fracture simulations.

The idea of partition of unity (PU) enrichment has been proposed to elliviate the mesh burden in fracture modeling [5]. Due to the additional enrichment functions, the discontinuities are introduced into the model and the representation of the crack only aims for initiating the enrichments, which makes the crack mesh independent from the component's mesh. The extended finite element method (XFEM) [26], usually coupled with the level set functions as an implicit representation of the crack, has been implemented for 3D crack growth problem [27][28][29][30] as well as for industrial applications [6][31][32]. The meshfree methods have also been proposed with the aim of further reducing the mesh burden, for instance, the element-free Galerkin (EFG) [33][34] and the extended EFG (XEFG) [35][36][37]. For more details, the readers could refer the review paper by Nguyen *et al* [38].

The fracture modeling by the boundary element method (BEM) exhibits more advantages than by FEM in terms of meshing/re-meshing efforts as

only the boundary discretization is required in BEM in order to approximate the quantity of interest. When cracks evolve, only the boundary surfaces are updated instead of re-generating the volume mesh. In order to circumvent the singular system caused by the collapsed surfaces in fracture, Hong and Chen [39] proposed the dual boundary integral representations by introducing the hyper-singular equation derived from the secondary field [40]. The use of dual boundary integral equations makes the crack propagation simulation more effective through a single domain. And the corresponding dual BEM was subsequently implemented for 2D and 3D fracture [41][42][43] and was extended to material-nonlinear fracture [44][45] and dynamic crack propagation [46]. Commercial packages based on BEM are BEASY [47] and FRANC3D [48]. Besides the dual BEM based on the collocation method, the Galerkin BEM, in particular the symmetric Galerkin BEM (SGBEM) has also drawn attention in the application for fracture analysis [49][50][51]. The symmetric matrix system of SGBEM also facilitates the coupling with FEM [52][53].

Besides the above classical FEM and BEM based approaches, versatile methods have been proposed to model fracture. The peridynamics uses integral equations to replace the partial differential equations of the classical continuum theory and can model fracture without the complications of mathematical singularities, due to the fact that the integral equations remain valid in the presence of cracks [54][55]. Kaczmarczyk *et al* presents a theory for propagating cracks based on configurational mechanics [56], where determining the direction of the propagating crack front is based on the principle of maximal energy dissipation using configurational forces. An enriched BEM was adopted for fracture analysis in [57] with accurate SIFs obtained. The scaled boundary FEM was also applied for fracture modeling, for more details, the readers can refer to [58][59][60].

Apart from the meshing/re-meshing issues in fracture simulation, the accurate evaluation of fracture parameters also attracts many researchers' attention. For example, the stress intensity factors, usually characterized as the driving force for the evolution of fatigue fracture, can be extracted from

the numerical solution. If the fracture parameters are computed based on the point-wise tips on the crack front independently, the approach can be considered as 'local'. The key factor to compute accurately the SIFs in a local approach is to avoid discretization and path dependence.

Due to the $1/\sqrt{r}$ stress singularity in the vicinity of the crack tip in LEFM, special care should be taken in the numerical methods in order to absolutely obtain more accurate SIFs. One approach to capture the asymptotics of the displacement and stress fields in the vicinity of a crack is the use of special crack tip elements; for example, quarter-point elements [61][62], which can exactly represent the $1/\sqrt{r}$ singularity in the near-tip stress field and allow a direct extraction of the SIFs [63]. The displacement correlation method [64], with or without crack-tip singular elements, is simple and fast. Nevertheless,this method is extraction path dependent. An extrapolation technique is typically performed upon a group of calculations to avoid such dependence. Another possibility is the hybrid crack element, developed in both the FEM and the BEM communities [65][66], which introduces asymptotic behavior of the stress field around crack tip into the tip-element so that the SIFs can be computed directly and accurately.

The virtual crack extension method (VCE), was applied to compute SIFs in [67][68]. The original VCE relies on the construction of a structured mesh along the crack front, which decreases mesh independence. However, it should be noted that in the same context of VCE, the variational form of the strain energy which involves the energy release rate and the crack extension has been developed for automatic crack growth [69][70]. The crack extension is given physical interpretation. The variational form minimizes the strain energy in a global sense and has recently been investigated in the framework of XFEM [71].

The virtual crack closure integral (VCCI) method, based on the virtual crack extension, is another alternative to extract SIFs in linear elastic fracture. Due to its simplicity and accuracy, the VCCI has been widely used in FEM and BEM [72]. While it should be noted that this method requires

the structured mesh near the crack front. The path-independent J integral proposed by Rice [73] is an attractive method due to its robustness regarding the relative independence in discretization and integral on domain. The method was extended into many branches based on both FEM and BEM [74][75][76][77][78]. The contour J integral is usually cast into the equivalent domain integral form in volume-based methods as stresses are discontinuous across element edges and statically admissible smoothing/recovery techniques are cumbersome. While in BEM the contour definition can be adopted directly [79]. In order to extract mixed mode SIFs, different techniques are developed. The J_x integrals ($x = 1, 2, 3$), as the components of the **J** integral, can be directly used to evaluate the SIFs. However, the evaluation of J_2 and J_3 (or G_{III}) exhibits numerical difficulties due to the singularity [80]. The J_1 integral (or J integral) can also be used to extract mixed mode SIFs, with some auxiliary operation. One approach is to decompose the displacement and stress fields into symmetric and antisymmetric portions with a structured mesh along the crack front, then the three modes of the J integral can be extracted directly [81][82][83][84]. The other method known as the M integral (or interaction energy integral), was developed by introducing asymptotic fields as an auxiliary solution [75] has been extended in (X)FEM [85][29] and BEM [86].

1.4 Isogeometric analysis

The isogeometric analysis (IGA) was first introduced by Hughes *et al* [87], as an alternative methodology to the traditional Lagrange polynomial based analyses. The IGA utilizes the same splines, that are used to exactly represent the geometry, as basis functions for the approximation of the unknown fields, which builds up a more direct link between CAD and analysis. Non-uniform rational B-splines (NURBS) based IGA has been widely investigated in many areas [88][89][90][91][92]. More flexible geometrical representation techniques, such as T-splines [93][94], PHT splines [95] and LR

Splines [96] etc., have been introduced to overcome the major difficulty of NURBS, i.e. the lack of local refinement due to its tensor product structure.

The isogeometric analysis has been applied to fracture in corporation with XFEM [97][98][99][100]. Verhoosel *et al* presented a scheme to model cohesive crack propagation by using T-splines to generate the local discontinuities [101]. Nguyen *et al* applied the B-spline based IGA to simulate the 2D and 3D delamination in composites [102]. The shape sensitivity analysis of stress intensity factors for curved cracks was performed by Choi and Cho [103]. Tambat *et al* proposed an enriched IGAFEM based on the CAD-inspired hierarchical partition of unity field compositions, and the method benefits from a robust and non-iterative numerical distance field construction [104][105]. Jeong *et al* proposed a geometrical mapping by which push-forwards of B-splines from the parameter space into the physical space such that the singularity of type $r^{1/2}$ can be captured in linear elastic cracks [106][107]. Natarajan *et al* enhanced the isogeometric analysis by the scaled boundary finite element method which inherits both advantages of FEM and IGABEM, while certain subdivision of the domain needs to be done for complicated geometry in order to obtain the scaling center [60].

However, we note that the application of IGA primarily focuses on 2D problems as the generation of the analysis-suitable 3D volume parametrization for complicated geometries is still an open question [108][109][110]. The investigation on the joint of IGA and BEM (IGABEM) has increasingly drawn attention recently since only the boundary representation of the geometry is required in IGABEM, which facilitates the integration of design and analysis. The IGABEM has already been applied in many fields [111][112][113][114][115][116][117][118], and has been further developed with more numerical aspects such as the PU enrichment [119][120], the trimmed NURBS [121][122], the fast solution [123], the Galerkin form [124][125] etc. The benefit of smoothness to boundary integrals (BIEs) brought by IGA is investigated in [126].

1.5 Introduction to the present work

In this work, the application of IGABEM in 2D/3D fracture analysis and fatigue crack growth will be explored. The advantages of the application in fracture based on the IGA framework can be concluded as:
(1) The higher-order continuity improves the accuracy of the stress field near the crack tip which is crucial to fracture analysis and the degrees of freedom is reduced compared to the C^0 Lagrange basis;
(2) The local crack tip (front) system can be constructed directly based on the spline-based curve or surface-represented cracks, which helps to accurately evaluate the fracture parameters;
(3) Combining With BEM, no volume parametrization/reparametrization is needed for crack initiation and propagation. The cracks are modeled by spline surfaces directly as external boundaries of the geometry. The concept of integration through design to analysis facilities the mechanical/structural design based on the fatigue fracture analysis.

This work outlines an IGABEM to simulate crack growth in 2D/3D linear-elastic setting. The method is based on the work of [87][112] in which NURBS based functions are used to approximate both the geometry and analysis fields. Besides using the conventional boundary integral equation as for elasticity, the hyper-singular integral equation is introduced additionally by exploiting the smoothness of NURBS geometries. An local singularity removing technique proposed by Guiggiani [127][128] is applied on the various orders of singular integrals (up to hyper-singular $O(1/r^3)$). The organization of this thesis is as following:
(1) In chapter 2, the formulations of the dual BEM for fracture modeling are briefly outlined, with more details including collocation and singular integration for 2D problems. Approaches for extraction of the SIFs, based on the M integral and the J_k integral, are studied in detail. A modified NURBS algorithm is outlined to simulate crack growth using NURBS based representation for cracks. Numerical examples are shown both for fracture analysis and crack propagation, in comparison with other popular methods

such as SGBEM, XFEM and XEFG;

(2) Chapter 3 mainly focuses on the issues of 3D implementation. A modified singular subtraction technique (SST) for (hyper-)singular integration tailored to distorted elements (or with high aspect ratio) which commonly arise in isogeometric based methods is formulated. The crack is explicitly represented by NURBS surface and the NURBS algorithm describing the crack propagation has been extended to 3D cases. The crack growth related work includes updating the crack surface geometrically, computing the stress intensity factors by M integral and virtual crack closure integral and the application of the fatigue fracture rule: the Paris law;

(3) In chapter 4, an implementation of IGABEM on trimmed NURBS surfaces is outlined. The method presented in our work is able to be applied with the closed trimming curve, thus providing a generalization scheme on non-trivial industrial geometries. Then a surface crack modeling technique is realized thanks to the developed work in trimmed NURBS. The problem of (nearly) singular integration on distorted elements is studied in detail as well as some remedies are proposed to enhance the application of IGABEM.

Chapter 5 will conclude the work and give a discussion on the problems and future work.

Chapter 2

IGABEM for 2D linear elastic fracture

Based on the paper '*Linear elastic fracture simulation directly from CAD: 2D NURBS-based implementation and role of tip enrichment*' submitted to Int. J. of Fracture

A method is proposed for simulating linear elastic crack growth through an isogeometric boundary element method directly from a CAD model and without any mesh generation. To capture the stress singularity around the crack tip, two methods are compared: (1) a graded knot insertion near crack tip; (2) partition of unity enrichment. A well-established CAD algorithm is adopted to generate smooth crack surfaces as the crack grows. The M integral and J_k integral methods are used for the extraction of stress intensity factors (SIFs). The convergence rates of SIFs by NURBS basis is $5 \sim 8$ times higher than those by discontinuous Lagrange basis.

2.1 NURBS basis functions

NURBS basis functions are the generalization of B-spline functions that allows a 'projection' from square and cubic domains to form complex geometries. So the basic concept of B-spline is first outlined. B-spline basis functions are defined over a knot vector, which is a non-decreasing sequence of real numbers given in the parameter space. A knot vector is denoted as $\Xi = \{\xi_1, \xi_2, ..., \xi_{n+p+1}\}$, where $\xi_A \in \mathbb{R}$ is the A^{th} parameter coordinate (knot), p is the order of the polynomial in B-spline basis functions, n is the

number of the basis functions. For a given order p, the B-spline basis functions $N_{A,p}$ with $1 \leqslant a \leqslant n$ are defined by the Cox-de Boor recursion:

$$N_{A,0}(\xi) = \begin{cases} 1 & \xi_A \leqslant \xi < \xi_{A+1} \\ 0 & \text{otherwise,} \end{cases} \tag{2.1}$$

then, for $p > 0$,

$$N_{A,p}(\xi) = \frac{\xi - \xi_A}{\xi_{A+p} - \xi_A} N_{A,p-1}(\xi) + \frac{\xi_{A+p+1} - \xi}{\xi_{A+p+1} - \xi_{A+1}} N_{A+1,p-1}(\xi). \tag{2.2}$$

The continuity of B-spline basis functions at ξ_A can be decreased by repeating the knot several times. If ξ_A has multiplicity k ($\xi_A = \xi_{A+1} = ... = \xi_{A+k-1}$), then the basis functions are C^{p-k} continuous at ξ_A. Particularly, when $k = p$, the basis is C^0 and $k = p + 1$ leads to a weak discontinuity at ξ_A. If the first and last knot have $k = p+1$, the knot vector is called an open knot vector. More details can be referred in [129].

Having defined the B-spline basis functions $\mathbf{N} = \{N_{A,p}\}_{A=1}^{n}$, we can describe a curve $C(\xi)$ in $\mathbb{R}^{d_s}$ (d_s is the spatial dimensionality, $d_s = 2$ in this chapter) by a group of control points $\mathbf{P} = \{\mathbf{P}_A\}_{A=1}^{n}$ with them as:

$$C(\xi) = \sum_{A=1}^{n} P_A N_{A,p}(\xi). \tag{2.3}$$

A NURBS curve is defined in the same way but by replacing the B-spline basis functions by NURBS basis functions. For example, a NURBS curve $C(\xi)$ can be described as:

$$C(\xi) = \sum_{A=1}^{n} P_A R_{A,p}(\xi), \tag{2.4}$$

where $R_{A,p}$ are the NURBS basis functions, which are defined as

$$R_{A,p}(\xi) = \frac{\omega_A N_{A,p}(\xi)}{\sum_{B=1}^{n} \omega_B N_{B,p}(\xi)}. \tag{2.5}$$

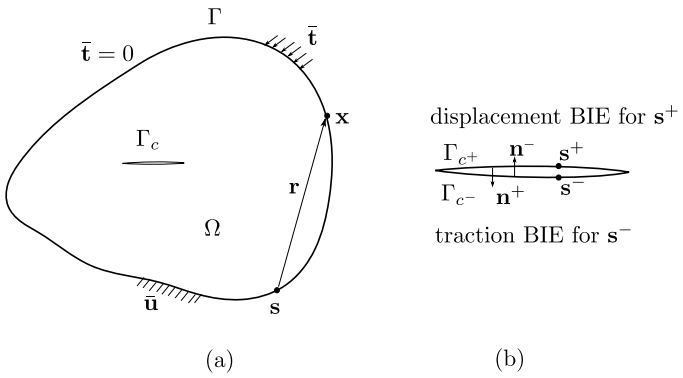

FIGURE 2.1: Crack model

ω_B is the weight associated with the B^{th} control point. Note that $R_{A,p}$ is only non-zero on the knot interval $[\xi_a, \xi_b]$) defined by $p+1$ control points.

2.2 Isogeometric BEM for fracture modeling

2.2.1 Problem formulation

Consider an arbitrary domain Ω which contains a crack as in Figure 2.1. The boundary Γ is composed of Γ_u where Dirichlet boundary conditions are prescribed (known displacement $\bar{\mathbf{u}}$), Γ_t where Neumann boundary conditions are prescribed (known traction $\bar{\mathbf{t}}$). The remaining part of the boundary is assumed to be traction free. The crack Γ_c is composed of two coincident faces: Γ_{c^+} and Γ_{c^-} is assumed also traction free. $\mathbf{s} = (s_1, s_2)$ denotes the source point and $\mathbf{x} = (x_1, x_2)$ the field point. The displacement BIE at source point $\mathbf{s}$ is given by finding $\mathbf{u}, \mathbf{t} : \Omega \to \mathbb{R}^2$ such that

$$c_{ij}(\mathbf{s})u_j(\mathbf{s}) + \fint_\Gamma T_{ij}(\mathbf{s},\mathbf{x})u_j(\mathbf{x})\mathrm{d}\Gamma(\mathbf{x}) = \int_\Gamma U_{ij}(\mathbf{s},\mathbf{x})t_j(\mathbf{x})\mathrm{d}\Gamma(\mathbf{x}), \tag{2.6}$$

where the U_{ij}, T_{ij} are called fundamental solutions and for linear elasticity (see appendix A for the expressions). Components T_{ij} exhibit a singularity of $O(1/r)$ and the sign $\fint$ implies that the corresponding integrals are understood in the sense of the Cauchy Principal Value, $|\mathbf{r}| = |\mathbf{x} - \mathbf{s}|$. and U_{ij} is weakly-singular (of order $O(\ln(1/r))$).

The traction BIE is obtained by differentiation of the displacement BIE with respect to s and multiplication by the elastic tensor E_{ijkl}:

$$c_{ij}(\mathbf{s})t_j(\mathbf{s}) + \oint\!\!\!\!\!\!= \int_\Gamma S_{ij}(\mathbf{s},\mathbf{x})u_j(\mathbf{x})\mathrm{d}\Gamma(\mathbf{x}) = \int_\Gamma K_{ij}(\mathbf{s},\mathbf{x})t_j(\mathbf{x})\mathrm{d}\Gamma(\mathbf{x}), \tag{2.7}$$

$$S_{ij}(\mathbf{s},\mathbf{x}) = E_{ikpq}\frac{\partial T_{pj}(\mathbf{s},\mathbf{x})}{\partial s_q}n_k(\mathbf{s}), \quad K_{ij}(\mathbf{s},\mathbf{x}) = E_{ikpq}\frac{\partial U_{pj}(\mathbf{s},\mathbf{x})}{\partial s_q}n_k(\mathbf{s}), \tag{2.8}$$

where S_{ij} is the hypersingular kernel ($O(1/r^2)$) and the sign $\oint\!\!\!\!\!\!=$ denotes the Hadamard finite part integrals and K_{ij} is of order $O(1/r)$. The fundamental solutions for the traction BIE are detailed in appendix A. $c_{ij}(\mathbf{s}) = 0.5\delta_{ij}$ when the source point s is on a smooth boundary.

The idea of the boundary element method is to discretize the boundary geometry and the physical fields using sets of basis functions. Subsequently, the source point is placed at the collocation points and the displacement BIE (2.6) is transformed into a corresponding system of linear algebraic equations. However, when the domain contains a crack, the collocation points on the overlapping surfaces (refer to Figure 2.1 (b)) Γ_{c^+} coincide with Γ_{c^-} and the system matrix becomes singular. Two ways to deal with this problem are given in the following sections.

2.2.2 Dual equations

The difficulty caused by the collapsed crack surfaces is circumvented through the use of dual equations, by prescribing different BIEs on either face of the crack. The displacement BIE (Equation (2.6)) is used on one face (S_{c^+}) and on the rest of the boundary S. The traction BIE (Equation (2.7)) is used on the other crack face (S_{c^-}). For the collocation point $\mathbf{s}^+$ on the crack surface

S_{c^+}, Equation (2.6) can be rewritten as,

$$\begin{aligned} c_{ij}(\mathbf{s}^+)u_j(\mathbf{s}^+) + c_{ij}(\mathbf{s}_m^-)u_j(\mathbf{s}^+) &= \int_S U_{ij}(\mathbf{s}^+,\mathbf{x})t_j(\mathbf{x})\mathrm{d}S(\mathbf{x}) \\ &- \int_S T_{ij}(\mathbf{s}^+,\mathbf{x})u_j(\mathbf{x})\mathrm{d}S(\mathbf{x}) \\ &- \int\!\!\!\!\!\!-_{S_{c^+}} T_{ij}(\mathbf{s}^+,\mathbf{x}^+)u_j(\mathbf{x}^+)\mathrm{d}S(\mathbf{x}) - \int\!\!\!\!\!\!-_{S_{c^-}} T_{ij}(\mathbf{s}_m^-,\mathbf{x}^-)u_j(\mathbf{x}^-)\mathrm{d}S(\mathbf{x}) \\ &+ \int_{S_{c^+}} U_{ij}(\mathbf{s}^+,\mathbf{x}^+)t_j(\mathbf{x}^+)\mathrm{d}S(\mathbf{x}) + \int_{S_{c^-}} U_{ij}(\mathbf{s}_m^-,\mathbf{x}^-)t_j(\mathbf{x}^-)\mathrm{d}S(\mathbf{x}). \end{aligned} \tag{2.9}$$

Analogously, the traction BIE (Equation (2.7)) on the other crack surface (S_{c^-} in Figure 2.1(b)) becomes,

$$\begin{aligned} c_{ij}(\mathbf{s}^-)t_j(\mathbf{s}^-) + c_{ij}(\mathbf{s}_m^+)t_j(\mathbf{s}^-) &= \int_S K_{ij}(\mathbf{s}^-,\mathbf{x})t_j(\mathbf{x})\mathrm{d}S(\mathbf{x}) \\ &- \int_S S_{ij}(\mathbf{s}^-,\mathbf{x})u_j(\mathbf{x})\mathrm{d}S(\mathbf{x}) \\ &- \int\!\!\!\!\!\!-_{S_{c^-}} S_{ij}(\mathbf{s}^-,\mathbf{x}^-)u_j(\mathbf{x}^-)\mathrm{d}S(\mathbf{x}) + \int\!\!\!\!\!\!-_{S_{c^+}} S_{ij}(\mathbf{s}_m^+,\mathbf{x}^+)u_j(\mathbf{x}^+)\mathrm{d}S(\mathbf{x}) \\ &+ \int\!\!\!\!\!\!-_{S_{c^-}} K_{ij}(\mathbf{s}^-,\mathbf{x}^-)t_j(\mathbf{x}^-)\mathrm{d}S(\mathbf{x}) - \int\!\!\!\!\!\!-_{S_{c^+}} K_{ij}(\mathbf{s}_m^+,\mathbf{x}^-)t_j(\mathbf{x}^+)\mathrm{d}S(\mathbf{x}). \end{aligned} \tag{2.10}$$

$\mathbf{s}_m^-$ denotes the mirror point of $\mathbf{s}^+$ on S_{c^-}, which means $\mathbf{s}_m^-$ and $\mathbf{s}^-$ share the same physical and parametric coordinates but their normal vectors are opposite. The last two terms of both equations and left hand side of Equation (2.10) are omitted due to the traction-free crack.

Remark: *due to the collapsed boundary, two jump terms arise in each BIE and each operator not only exhibits singularity on the crack surface where the collocation points are located, but also on the one where the mirror points of the collocation points are located.*

2.2.3 Crack opening displacement equation

The boundary integral equation for crack problem can also be reformulated by setting the boundary quantity as crack opening displacement (COD) over a couple of crack surfaces. Let the source point approach one crack

surface, for example $S_c = S_{c^+}$, and note that $\mathbf{n} = \mathbf{n}^+ = -\mathbf{n}^-$, we have:

$$\begin{aligned} c_{ij}(\mathbf{s}^+)u_j(\mathbf{s}^+) + c_{ij}(\mathbf{s}^-)u_j(\mathbf{s}^-) = & \int_S U_{ij}(\mathbf{s}^+, \mathbf{x})t_j(\mathbf{x})\mathrm{d}S(\mathbf{x}) \\ & - \fint_S T_{ij}(\mathbf{s}^+, \mathbf{x})u_j(\mathbf{x})\mathrm{d}S(\mathbf{x}) \\ & + \int_{S_c} U_{ij}(\mathbf{s}^+, \mathbf{x}^+)(t_j(\mathbf{x}^+) + t_j(\mathbf{x}^-))\mathrm{d}S(\mathbf{x}) \\ & - \fint_{S_c} T_{ij}(\mathbf{s}^+, \mathbf{x}^+)(u_j(\mathbf{x}^+) - u_j(\mathbf{x}^-))\mathrm{d}S(\mathbf{x}). \end{aligned} \tag{2.11}$$

The corresponding traction BIE is:

$$\begin{aligned} c_{ij}(\mathbf{s}^+)t_j(\mathbf{s}^+) - c_{ij}(\mathbf{s}^-)t_j(\mathbf{s}^-) = & \fint_S K_{ij}(\mathbf{s}^+, \mathbf{x})t_j(\mathbf{x})\mathrm{d}S(\mathbf{x}) \\ & - \fint_S S_{ij}(\mathbf{s}^+, \mathbf{x})u_j(\mathbf{x})\mathrm{d}S(\mathbf{x}) \\ & + \fint_{S_c} K_{ij}(\mathbf{s}^+, \mathbf{x}^+)(t_j(\mathbf{x}^+) + t_j(\mathbf{x}^-))\mathrm{d}S(\mathbf{x}) \\ & - \fint_{S_c} S_{ij}(\mathbf{s}^+, \mathbf{x}^+)(u_j(\mathbf{x}^+) - u_j(\mathbf{x}^-))\mathrm{d}S(\mathbf{x}). \end{aligned} \tag{2.12}$$

Equation (2.12) can be used alone if the COD alone will be used as the unknown for the fatigue crack growth problem. However if the displacement field needs to be known on the crack surfaces, Equation (2.11) should also be solved. For a infinite domain ($S \to \infty$), assuming that traction-free crack faces are assumed, we arrive at:

$$0 = t_j^\infty(\mathbf{s}) - \fint_{S_c} S_{ij}(\mathbf{s}, \mathbf{x})[\![u_j(\mathbf{x})]\!]\mathrm{d}S(\mathbf{x}). \tag{2.13}$$

$[\![u_j(\mathbf{x})]\!] = u_j(\mathbf{x}^+) - u_j(\mathbf{x}^-)$ is the crack opening displacement. All the subscripts '+' are omitted since the integral is only over a single crack surface. $\mathbf{t}^\infty$ is interpreted as the solution in the 'no crack' space.

2.2.4 NURBS discretization of the boundary integral equations

In the NURBS based isogeometric concept, the physical field is approximated by the same NURBS basis functions as those used to describe the

geometry $\Gamma = C(\xi)$. The displacement and traction fields can be approximated as follows:

$$u_i(\xi) = \sum_{A=1}^{n} R_{A,p}(\xi) d_i^A, \tag{2.14}$$

$$t_i(\xi) = \sum_{A=1}^{n} R_{A,p}(\xi) q_i^A, \tag{2.15}$$

We define an element in the parameter space as an interval between two consecutive non-repeated knots $[\xi_a, \xi_b]$. And particularly for a singular element, this knot interval is linearly mapped to interval $[-1, 1]$, which is called the parent space [87] and the number of elements is N_e. We define $\hat{\xi}$ as the parent coordinate of the field point $\mathbf{x}$ in $[-1, 1]$, $\hat{\xi}_s$ as the parent coordinate of the source point $\mathbf{s}$ in $[-1, 1]$, and $J(\hat{\xi})$ is the Jacobian transformation from physical to parent space. The transformation process for one NURBS element (the knot interval $[\xi_a, \xi_b]$) to the parent space $[-1, 1]$ is shown in Figure 2.2. And we have

$$\begin{aligned} \xi = \xi(\hat{\xi}) &= \frac{(\xi_b - \xi_a)\hat{\xi} + (\xi_b + \xi_a)}{2}, \\ J(\hat{\xi}) &= \frac{\mathrm{d}\Gamma}{\mathrm{d}\xi} \frac{\mathrm{d}\xi}{\mathrm{d}\hat{\xi}}. \end{aligned} \tag{2.16}$$

Then the above form can also be written via the elemental approximation as:

$$u_i(\hat{\xi}) = \sum_{A=1}^{p+1} N_A(\hat{\xi}) d_i^A, \tag{2.17}$$

$$t_i(\hat{\xi}) = \sum_{A=1}^{p+1} N_A(\hat{\xi}) q_i^A, \tag{2.18}$$

where

$$N_A(\hat{\xi}) = R_{I,p}(\xi). \tag{2.19}$$

And d_i, q_i are displacement and traction control variables respectively. The relation between the local index A and the global index I is given by the element connectivity [112]. Substituting the discretized displacements and

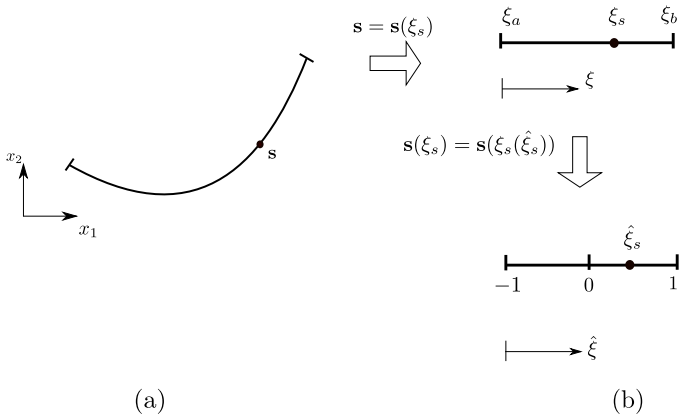

FIGURE 2.2: Coordinate system in IGABEM: (a) the element containing collocation point s in the global space; (b)the parametric space and parent space

tractions into the BIEs will give,

$$\sum_{I=1}^{p+1} C_{ij}^I(\mathbf{s}) d_j^I + \sum_{e=1}^{N_e} \sum_{I=1}^{p+1} T_{ij}^I d_j^I = \sum_{e=1}^{N_e} \sum_{I=1}^{p+1} U_{ij}^I q_j^I, \tag{2.20}$$

$$\sum_{I=1}^{p+1} C_{ij}^I(\mathbf{s}) t_j^I + \sum_{e=1}^{N_e} \sum_{I=1}^{p+1} S_{ij}^I d_j^I = \sum_{e=1}^{N_e} \sum_{I=1}^{p+1} K_{ij}^I q_j^I, \tag{2.21}$$

where the jump term and integrals of the fundamental solutions are respectively written as:

$$C_{ij}^I(\mathbf{s}) = c_{ij} R_I(\hat{\xi}_s), \tag{2.22}$$

$$T_{ij}^I = \int_{-1}^{1} T_{ij}(\mathbf{s}, \mathbf{x}(\hat{\xi})) R_I(\hat{\xi}) J(\hat{\xi}) \mathrm{d}\hat{\xi}, \tag{2.23}$$

$$U_{ij}^I = \int_{-1}^{1} U_{ij}(\mathbf{s}, \mathbf{x}(\hat{\xi})) R_I(\hat{\xi}) J(\hat{\xi}) \mathrm{d}\hat{\xi}, \tag{2.24}$$

$$S_{ij}^I = \int_{-1}^{1} S_{ij}(\mathbf{s}, \mathbf{x}(\hat{\xi})) R_I(\hat{\xi}) J(\hat{\xi}) \mathrm{d}\hat{\xi}, \tag{2.25}$$

$$K_{ij}^I = \int_{-1}^{1} K_{ij}(\mathbf{s}, \mathbf{x}(\hat{\xi})) R_I(\hat{\xi}) J(\hat{\xi}) \mathrm{d}\hat{\xi}. \tag{2.26}$$

2.2.5 Treatment of singular integrals

Integrating the weakly-singular, strongly-singular and hyper-singular kernels in Equations (2.23)-(2.26) is a major difficulty in BEM. In the present work, weakly-singular integrals are evaluated using Telles' transformation

[130]. Strongly-singular integrals in Equation (2.6) are treated in two different ways. In the first approach, the singularity in T_{ij} is removed by the regularization method, based on use of simple solutions [131][132], i.e. the rigid body motions, which satisfy Equation (2.6) with zero tractions. Adding and subtracting term $\mathbf{u}(\mathbf{s})$ in Equation (2.6), the strongly-singular equation can be transformed into the regularized form:

$$\int_{\Gamma} T_{ij}(\mathbf{s},\mathbf{x})(u_j(\mathbf{x})-u_j(\mathbf{s}))\mathrm{d}\Gamma(\mathbf{x}) = \int_{\Gamma} U_{ij}(\mathbf{s},\mathbf{x})t_j(\mathbf{x})\mathrm{d}\Gamma(\mathbf{x}). \tag{2.27}$$

After discretization, Equation (2.27) becomes

$$\sum_{e=1}^{N_e}\sum_{I=1}^{p+1} P_{ij}^I d_j^I = \sum_{e=1}^{N_e}\sum_{I=1}^{p+1} U_{ij}^I q_j^I, \tag{2.28}$$

where

$$P_{ij}^I = \int_{-1}^{1} T_{ij}(\mathbf{s},\mathbf{x}(\hat{\xi}))(R_I(\hat{\xi})-R_I(\hat{\xi}_s))J(\hat{\xi})\mathrm{d}\hat{\xi}. \tag{2.29}$$

The implementation of Equation (2.27) is simple and does not require calculation of jump term $c_{ij}(\mathbf{s})$. However, when Equation (2.27) is used at coincident points on crack surfaces, the singularity corresponding to only one of the points is removed. There have been many attempts to overcome this difficulty. For example, creating artificial integration surfaces, excluding the second singular point [133][134] is a possibility. However, the creation and evaluation along the artificial surface is expensive computationally [135] and is particularly cumbersome to deal with in the framework of isogeometric analysis. Therefore, in the present work, Equation (2.27) is used only on the non-cracked boundary, while on crack surfaces, the approach, known as the singularity subtraction technique (SST), is used [127]. SST is applied to both strongly-singular and hyper-singular integrals after the parametrization in the parent space (Equations (2.23), (2.25) and (2.26)). The essential idea of the method is to expand the production of the kernel function, the shape function and the Jacobian $J(\hat{\xi})$ into Taylor series in the vicinity of the collocation point, and split the integrands into regular and singular parts. Then the singular terms can be evaluated analytically,

while for regular terms standard Gauss quadrature is sufficient. Take the hyper-singular integral term S^e_{ijl} as an example:

$$S^I_{ij} = \int_{-1}^{1} S_{ij}(\mathbf{s}, \mathbf{x}(\hat{\xi}))R_I(\hat{\xi})J(\hat{\xi})\mathrm{d}\hat{\xi} = \int_{-1}^{1} F(\hat{\xi}_s, \hat{\xi})\mathrm{d}\hat{\xi}. \tag{2.30}$$

The function $F(\hat{\xi}_s, \hat{\xi})$ can be expanded as:

$$F(\hat{\xi}_s, \hat{\xi}) = \frac{F_{-2}(\hat{\xi}_s)}{\delta^2} + \frac{F_{-1}(\hat{\xi}_s)}{\delta} + O(1), \tag{2.31}$$

where $\delta = \hat{\xi} - \hat{\xi}_s$. The details to obtain F_{-2} and F_{-1} with a NURBS basis are given in appendix B.1 or in [127][57]. The final form of (2.30) is given by:

$$\begin{aligned}\int_{-1}^{1} F(\hat{\xi}_s, \hat{\xi})\mathrm{d}\hat{\xi} = \int_{-1}^{1} \left(F(\hat{\xi}_s, \hat{\xi}) - \frac{F_{-2}(\hat{\xi}_s)}{\delta^2} - \frac{F_{-1}(\hat{\xi}_s)}{\delta} \right) \mathrm{d}\hat{\xi} \\ + F_{-2}(\hat{\xi}_s)\left(-\frac{1}{1-\hat{\xi}_s} + \frac{1}{-1-\hat{\xi}_s} \right) + F_{-1}(\hat{\xi}_s)\ln\left| \frac{1-\hat{\xi}_s}{-1-\hat{\xi}_s} \right|.\end{aligned} \tag{2.32}$$

The first integral in (2.32) is regular and it is evaluated using standard Gaussian quadrature.

2.2.6 Partition of unity enrichment formulation

The partition of unity (PU) enrichment method [136] has been well studied in FEM to model problems with *a priori* knowledge about the solution. See Sukumar *et al* [27], Moës *et al*[29], Gravouil *et al* [28] for application of XFEM to 3D crack propagation and Bordas and Moran [6], Bordas *et al* [137], Wyart *et al* [32] for industrial damage tolerance assessment using XFEM. It was also shown in the literature that the accuracy of the stress intensity factors for 3D linear elastic fracture mechanics was insufficient for coarse meshes and always oscillatory. A posterori error estimate were derived [138][31][139][140] and implemented within the commercial software Morfeo to control the discretization error [31][139].

The approximation of the primary field by PU enrichment is decomposed by two parts: a regular part and an enriched part. The latter allows the approximation to reproduce specific information on the solution

through additional degrees of freedom. And the enrichment idea has been introduced within BEM as well [141][119]. Simpson *et al* [57] first proposed the idea of enrichment in BEM to capture the stress singularity around the crack tip. The enriched displacement approximation with a NURBS basis writes:

$$u_i(\mathbf{x}) = \sum_{I\in\mathscr{R}_I} R_I(\mathbf{x}) d_i^I + \sum_{J\in\mathscr{R}_J} R_J(\mathbf{x}) \sum_{l=1}^{4} \phi_l(\mathbf{x}) a_i^J, \tag{2.33}$$

where d_i^I are the regular DOFs. a_i^J are the crack tip enriched DOFs. See [137] for implementation details in an XFEM framework. Since in BEM the crack is explicitly modeled by two overlapping surfaces, the Heaviside enrichment is not required. $\mathscr{R}_I$ and $\mathscr{R}_J$ are the collections of regular control points and enriched control points, respectively. The crack tip enrichment functions are defined as:

$$\{\phi_l(r,\theta), l=1,4\} = \left\{\sqrt{r}\sin\frac{\theta}{2}, \sqrt{r}\cos\frac{\theta}{2}, \sqrt{r}\sin\frac{\theta}{2}\sin\theta, \sqrt{r}\cos\frac{\theta}{2}\sin\theta\right\}, \tag{2.34}$$

where (r,θ) are the polar coordinates associated with the crack tip. If the enrichment is done in a small vicinity of the crack tip, where the crack can be regarded as a straight line, i.e. in Equation (2.34) angle $\theta = \pm\pi$ and the set of four crack tip enrichment functions can be reduced to one, i.e. $\phi(r) = \sqrt{r}$. Then Equation (2.35) results in:

$$u_i(\mathbf{x}) = \sum_{I\in\mathscr{R}_I} R_I(\mathbf{x}) d_i^I + \sum_{J\in\mathscr{R}_J} R_J(\mathbf{x}) \phi(\mathbf{x}) a_i^J. \tag{2.35}$$

Substituting the above equation into (2.6) and (2.7) and discretizing with a NURBS basis, the enriched displacement and traction boundary integral equations can be obtained, respectively:

$$\sum_{I}^{p+1} C_{ij}^I(\mathbf{s})(d_j^I + \phi(\mathbf{s}) a_j^I) + \sum_{e=1}^{N_e}\sum_{I}^{p+1}(T_{ij}^I d_j^I + T_{ij}^I \phi a_j^I) = \sum_{e=1}^{N_e}\sum_{I}^{p+1} U_{ij}^I q_j^I, \tag{2.36}$$

$$\sum_{I}^{p+1} C_{ij}^I(\mathbf{s}) t_j^I + \sum_{e=1}^{N_e}\sum_{I}^{p+1}(S_{ij}^I d_j^I + S_{ij}^I \phi a_j^I) = \sum_{e=1}^{N_e}\sum_{I}^{p+1} K_{ij}^I q_j^I, \tag{2.37}$$

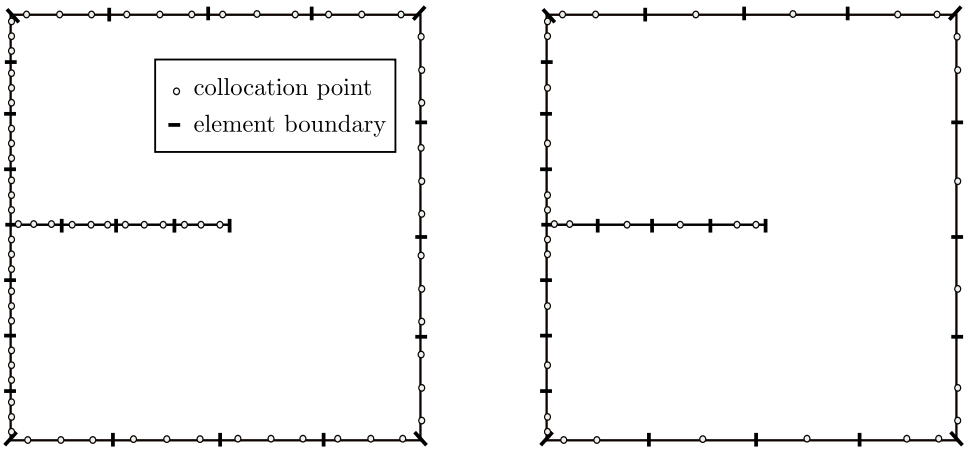

FIGURE 2.3: Mesh discretization for a mode I crack: (a) discontinuous Lagrange element ($p = 2$), (b) NURBS ($p = 2$)

where

$$T_{ij}^I\phi = \int_{-1}^{1} T_{ij}(\mathbf{s}, \mathbf{x}(\hat{\xi}))R_I(\hat{\xi})\phi(\mathbf{x}(\hat{\xi}))J(\hat{\xi})\mathrm{d}\hat{\xi},$$
$$S_{ij}^I\phi = \int_{-1}^{1} S_{ij}(\mathbf{s}, \mathbf{x}(\hat{\xi}))R_I(\hat{\xi})\phi(\mathbf{x}(\hat{\xi}))J(\hat{\xi})\mathrm{d}\hat{\xi}. \tag{2.38}$$

Note that topological enrichment is used, i.e. only the elements containing the crack tip are enriched, the enrichment terms do not need to be computed for unenriched elements. Differing from [57] where the discontinuous quadratic Lagrange elements are enriched, the enrichment for the NURBS basis will lead to blending elements due to the continuity of the basis. The singular integration for enriched elements can be done with SST as in section 2.2.5 as long as the local expansion for $\phi(r) = \sqrt{r}$ at the collocation point with respect to intrinsic coordinate is written explicitly.

2.2.7 Continuity requirements and collocation strategy

Methods for evaluating strongly-singular and hyper-singular integrals (2.23), (2.25), (2.26), described above, are implicitly or explicitly based on Taylor expansions of the integrands in the vicinity of the collocation point. Since the essential feature of the isogemetric approach is to represent displacements, tractions and the geometry using the same NURBS basis functions,

special attention should be paid to the continuity of NURBS basis functions at the collocation points where the Taylor series are expanded.

In the classical boundary element method a common way to guarantee the existence of integrals in (2.23), (2.25), (2.26) is by the so-called discontinuous quadratic Lagrange elements [41], i.e. placing collocation points inside an element, where the quadratic polynomials are C^{∞} continuous. The same approach can be implemented with NURBS parametrization, since inside the elements NURBS basis functions are infinitely smooth, i.e. the SST can be used directly to treat all singularities. In Figure 2.3 (a) and (b) examples of boundary discretization are shown for classical BEM and IGABEM respectively, where the collocation points in IGA are generated by Greville abscissae [142] and the collocation points are moved inside the elements when higher order continuity is necessary.

For the enrichment formulation, since enriched DOFs are introduced, additional source points need to be collocated to balance the number of system unknowns. The location of the source points plays an important role in the condition number of the BEM system matrix. It reveals that for crack tip enrichment, when the additional collocation points are inside the enriched element, the system condition remains small and gives accurate solutions (see [57] for more details). Nevertheless, the specific location inside the crack tip element has little influence on the final results. Hence in this work, the additional source points are inserted within the crack tip element and spread uniformly between the original collocation points. Figure (2.4) illustrates the scheme applied in this chapter for collocation on the crack surface.

However, the classical theory of boundary integral equations admits much weaker continuity requirements, i.e. the Cauchy and Hadamard integrals exist for $C^{1,\alpha}(\Gamma)(0 < \alpha < 1)$ density functions (known as Hölder continuous) [143]. Therefore, strongly singular and hyper-singular equations, and all the more so the regularized equation (2.27), can be used at collocation points located at the edges of the elements in IGABEM, provided that the NURBS basis is sufficiently smooth. However, optimal collocation

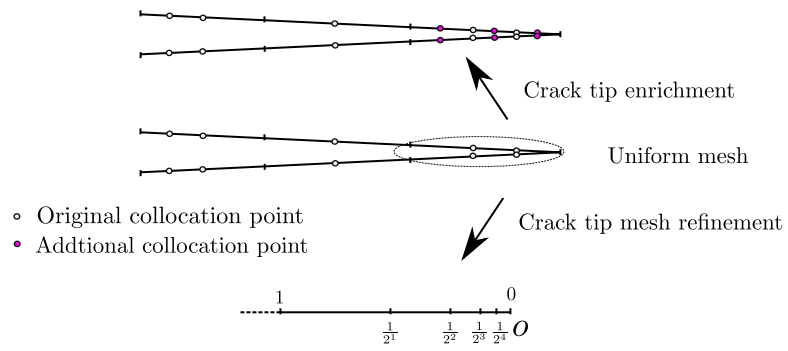

FIGURE 2.4: Mesh and collocation for crack surfaces

strategies remain the subject of further research, and require more detailed theoretical and numerical studies.

2.3 Evaluation of stress intensity factors

2.3.1 J_k-integral

In this section, two different kinds of J integral based methods for the extraction of SIFs are briefly reviewed. The first one is the J_k method proposed in [80], which is the more general case of the J integral. The definition of the J_k in 2D is given as:

$$J_k := \lim_{\Gamma_\epsilon \to 0} \int_{\Gamma_\epsilon} (W\delta_{jk} - \sigma_{ij}u_{i,k})n_j \mathrm{d}\Gamma = \lim_{\Gamma_\epsilon \to 0} \int_{\Gamma_\epsilon} P_{kj}n_j \mathrm{d}\Gamma, \tag{2.39}$$

where P_{kj} is the Eshelby tensor, $W = 1/2\sigma_{ij}\epsilon_{ij}$ is the strain energy density, n_j is the unit outward normal of Γ_ϵ. J_1 represents a special case, the J integral. Throughout the chapter we will use these two notations interchangeably. All the variables are defined in the crack tip local coordinate system (x_0, y_0) as in Figure 2.5 (a). However, from the numerical point of view, it is difficult to calculate the limit in Equation (3.19), so that the definition of J_k is usually modified in the following way. Since the integral of the Eshelby tensor is equal to zero for any closed contour, which does not contain a defect, additional contours Γ, Γ_{c^+}, Γ_{c^-} are introduced, such that

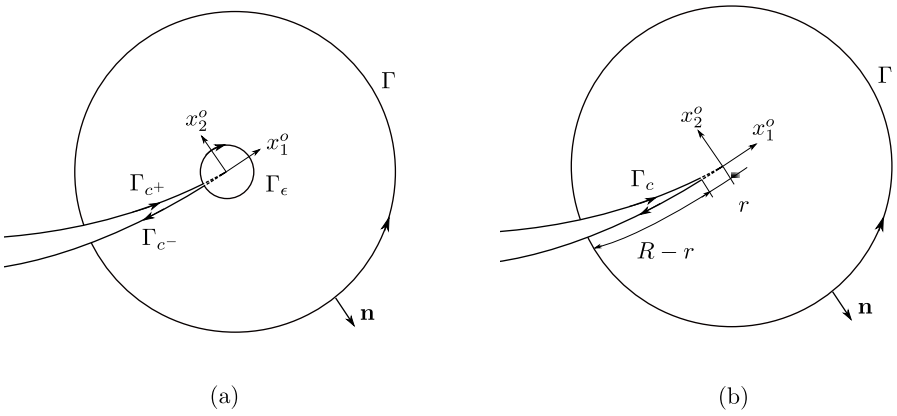

FIGURE 2.5: Path definition for J integral

Equation (3.19) can be rewritten as [144]

$$J_k = \lim_{\Gamma_\epsilon \to 0} \int_{\Gamma_\epsilon} P_{kj} n_j \mathrm{d}\Gamma = \int_{\Gamma} P_{kj} n_j \mathrm{d}\Gamma + \int_{\Gamma_{c^+}} P_{kj} n_j \mathrm{d}\Gamma + \int_{\Gamma_{c^-}} P_{kj} n_j \mathrm{d}\Gamma. \tag{2.40}$$

When $k = 1$, for a flat crack $n_1 = 0$ along the crack surfaces and thus along the contours Γ_{c^+} and Γ_{c^-} the integral is zero, and Equation (2.40) simplifies to:

$$J_1 = \int_{\Gamma} P_{1j} n_j \mathrm{d}\Gamma. \tag{2.41}$$

This expression shows the path independence of the J integral for a flat crack. But for the J_2 integral, the term associated with the crack surface cannot be omitted since $n_2 = 1$ and this term leads to a singularity in numerical evaluation.

The most general 2D scenario must account for curved cracks. The associated contribution from the crack surfaces to both J_1 and J_2 cannot in general be neglected. It should be noted that the energy density $W = O(1/r)$ when approaching the crack tip since both σ_{ij} and ϵ_{ij} tend to $1/\sqrt{r}$. The integrand along the crack surface will remain of $O(1/r)$, and this kind of singular integral cannot be treated in a regular way. In [144] and [80], the crack surface was split into a far field part and a near-tip part (Figure 2.5(b)) in order to evaluate the singular integral:

$$J_k = \int_{\Gamma} P_{kj} n_j \mathrm{d}\Gamma + \int_{R-r} [\![W]\!] n_k^+ \mathrm{d}\Gamma + \int_{r} [\![W]\!] n_k^+ \mathrm{d}\Gamma. \tag{2.42}$$

The far field part is integrated by regular Gauss quadrature. The near-tip part integral on the crack surface can be simply omitted for $J_1(k=1)$, since n_1 is mostly zero, while for $J_2(k=2)$, the near-tip part exhibits the $O(1/r)$ singularity. The energy jump $[\![W]\!]$ on the near-tip surface can be evaluated as in [144]:

$$[\![W]\!] = \frac{-4K_{II}\sigma_{x0}}{E\sqrt{2\pi r}} + O(r^{1/2}), \tag{2.43}$$

where σ_{x0} is called T-stress. Thus near-tip part of $[\![W]\!]$ can be represented as a proportion to the $r^{1/2}$

$$J_k = \int_\Gamma P_{kj} n_j \mathrm{d}\Gamma + \int_{R-r} [\![W]\!] n_k^+ \mathrm{d}\Gamma + \Lambda n_k r^{1/2}. \tag{2.44}$$

Since two unknown variables J_2 and Λ appear in the above equation, the integral cannot be evaluated at once. The splitting procedure needs to be performed several times by taking different r, and a group of values of J_2 and Λ can be found in order to extrapolate J_2 for the case of no splitting. In Equation (2.44), as long as the $O(1/r^{1/2})$ can be captured, the J_k integral can be correctly evaluated and the SIFs can be deduced (see appendix C.1). Nevertheless, the choice of the extraction radius 'r' becomes path dependent and problem dependent in real applications.

2.3.2 M integral

The M integral is another possible method to extract the SIFs. By applying the J integral under two states, the actual state (denoted with superscript '1'), and the auxiliary state (superscript '2'), and adding them together:

$$J^{(1+2)} = \int_{\Gamma_\epsilon} \Big[\frac{1}{2}(\sigma_{ij}^{(1)} + \sigma_{ij}^{(2)})(\epsilon_{ij}^{(1)} + \epsilon_{ij}^{(2)})\delta_{1j} - (\sigma_{ij}^{(1)} + \sigma_{ij}^{(2)})\frac{\partial(u_i^{(1)} + u_i^{(2)})}{\partial x_1}\Big] n_j \mathrm{d}\Gamma. \tag{2.45}$$

Rearranging the two state terms gives

$$J^{(1+2)} = J^{(1)} + J^{(2)} + M^{(1,2)}, \tag{2.46}$$

where

$$M^{(1,2)} = \int_{\Gamma_\epsilon} \left[W^{(1,2)} \delta_{1j} - \sigma_{ij}^{(1)} \frac{\partial u_i^{(2)}}{\partial x_1} - \sigma_{ij}^{(2)} \frac{\partial u_i^{(1)}}{\partial x_1} \right] n_j \mathrm{d}\Gamma, \tag{2.47a}$$

$$W^{(1,2)} = \sigma_{ij}^{(1)} \epsilon_{ij}^{(2)} = \sigma_{ij}^{(2)} \epsilon_{ij}^{(1)}. \tag{2.47b}$$

Once the M integral has been evaluated, the SIFs can be extracted directly (see appendix C.2). But we note that in Yau *et al*'s work [75], a flat crack surface is assumed. When applied to practical problems, the radius of the contour circle should be chosen 'small enough' to guarantee that within the domain bounded by Γ, the crack is 'almost' straight.

In this chapter, the M integral is adopted. A detailed comparison of both methods applied to curved cracks is provided in the forthcoming sections.

Once the SIFs have been obtained, the maximum hoop stress criterion is used to determine the direction of crack propagation. We assume that the crack propagates in the direction θ_c such that the hoop stress is maximum, which is given (see [145], for example) by the following expression. Note that the quantity of interest determining the accuracy of each propagation step is the ratio (K_{II}/K_I)

$$\theta_c = 2\arctan\left[\frac{-2(K_{II}/K_I)}{1 + \sqrt{1 + 8(K_{II}/K_I)^2}} \right]. \tag{2.48}$$

2.4 2D NURBS crack propagation

A NURBS crack propagation algorithm is outlined next. The conceptual idea for the deformation of the NURBS curve representing the crack is realised by moving the control points to make the curve satisfy the external constraints under a user-defined function [146]. For crack growth, the external constraint is the movement of the position of crack tip (or crack front in 3D). Paluszny *et al* implemented the idea in FEM to represent crack growth or intersection by updating the control points to satisfy the constraints given by fracture parameters [147]. The algorithm is briefly reviewed as follows:

- Initiation: represent the crack by the NURBS curve;
- Calculate the new physical position of the crack tip M' (the space constraint). This is determined by specified fracture criterion given in section 2.3.2;
- Specify the parametric coordinate ξ (the parametric constraint) of the old crack tip M;
- Define the influence functions f. Here for 2D fracture these functions are selected as the NURBS basis functions at the parametric constraint ξ (which is called natural deformation in [146]). $f(A) = R_{A,p}(\xi)$, $A = 1, ..., n$, n is the number of NURBS basis function of the corresponding control point P_A.
- Calculating the motion vector of each control point $\mathbf{m}(A)$: the movement of the control points is given by

$$\mathbf{m}(A) = \frac{f(A)}{\sum_{B=1}^{n} R_{B,p}(\xi) f(B)} \mathbf{e}, \quad \mathbf{e} = \overrightarrow{MM'}. \tag{2.49}$$

The process to stretch a NURBS curve to simulate crack growth in 2D is illustrated in Figure 2.6. Certain knot insertion should be done at the crack tip element in order to capture the local changes. We note that refining the crack tip element also helps improve the solution near the crack tip, and a graded mesh refinement is designed as in Figure 2.4, where the new knots are inserted consecutively at the $(1/2)^i, \quad i = 1, 2, 3, 4...$ of the distance to the crack tip in parametric space (the obtained meshes are denoted as $R1$, $R2$, $R3$, $R4$...).

2.5 Numerical examples

In this section, several numerical examples are presented to verify the proposed method for fracture analysis. We first give examples to study the behavior of the (X)IGABEM on static fracture analysis. Then the application to crack propagation by comparing against XFEM is demonstrated. A

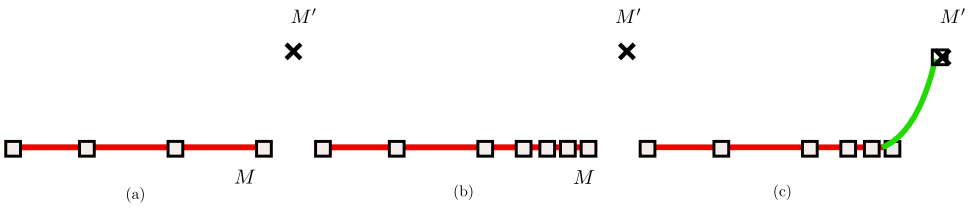

FIGURE 2.6: NURBS modification for crack growth. (a)Original crack and new crack tip M'; (b)Knot insertion to refine the crack tip element; (c)Move the control points to obtain new crack curve by the presented algorithm

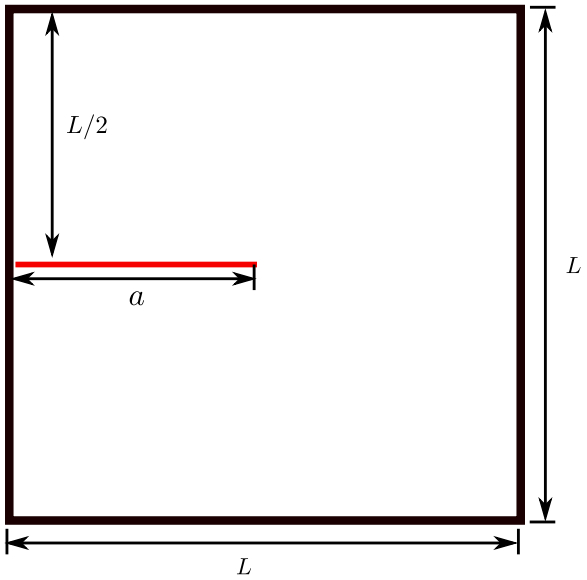

FIGURE 2.7: Edge crack

fixed number of Gauß points ($ngp = 30$) is adopted for the integration of both singular and nearly-singular integrals, although we note that it would be desirable to develop adaptive quadrature rules for the nearly-singular integrals in BEM. The order of NURBS basis and discontinuous lagrange basis is taken as 2 for all the examples.

2.5.1 Edge crack

Figure 2.7 illustrates the chosen edge crack problem. we use the first-term asymptotic solution of a crack problem [148] (refer to the auxiliary displacements in appendix C.3), which we prescribe as Dirichlet boundary condition on the outer boundaries, while keeping crack faces traction free. The parameters $E = 1$, $\nu = 0.3$, $a = 1$, $L = 2$. For a mode I crack,

$K_I = 1, K_{II} = 0$ and for a mode II crack, $K_I = 0, K_{II} = 1$. Thus the numerical displacement field on the crack as well as the SIFs can be compared to the analytical solution.

Ability of the method to capture the crack tip singularity

An accurate approximation of the solution near the crack tip is crucial to the accurate evaluation of fracture parameters such as the SIFs. Three scenarios are studied here, uniform meshes, graded refinement and enrichment of the crack tip element with function given in Equation (2.35). Figure 2.8 shows the displacement u_y along the upper crack surface for the mode I problem. The crack is discretized by 3 uniform elements. It can be observed that in all cases, the numerical displacements agree well with the analytical solution, even for coarse meshes. The graded refinement and enrichment method both give improved results near the crack tip. To further assess the accuracy of these methods, the error in the displacement L_2 norm of the displacements along the crack surfaces, given by

$$e_{L_2} = \sqrt{\frac{\int_{\Gamma_c} (\mathbf{u} - \mathbf{u}_{ext})^{\mathrm{T}} (\mathbf{u} - \mathbf{u}_{ext}) \mathrm{d}\Gamma}{\int_{\Gamma_c} \mathbf{u}_{ext}^{\mathrm{T}} \mathbf{u}_{ext} \mathrm{d}\Gamma}} \tag{2.50}$$

is plotted in Figure 2.9. We check the convergence results by inserting the knots at $(1/2)^i$ consecutively until $i = 4$ described in Figure 2.4 (the results are denoted as $R1, R2, R3$ and $R4$ respectively). It can be seen that enrichment achieves an accuracy which is intermediate between $R3$ and $R4$ graded meshes while the convergence rate is improved by 55% compared to the graded mesh refinement. In the following examples for static crack and crack propagation, the graded mesh refinement by 4 successive knot insertions is used for study further.

SIFs comparison with Lagrange basis

To evaluate the potential of IGABEM for fracture, the SIFs given by the M integral are compared to those from Lagrange elements using uniform meshes and no special treatment for the crack tip. The radius for the M

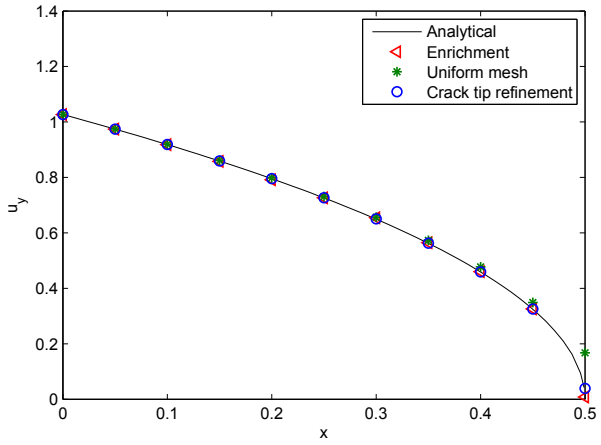

FIGURE 2.8: u_y along the upper crack surface

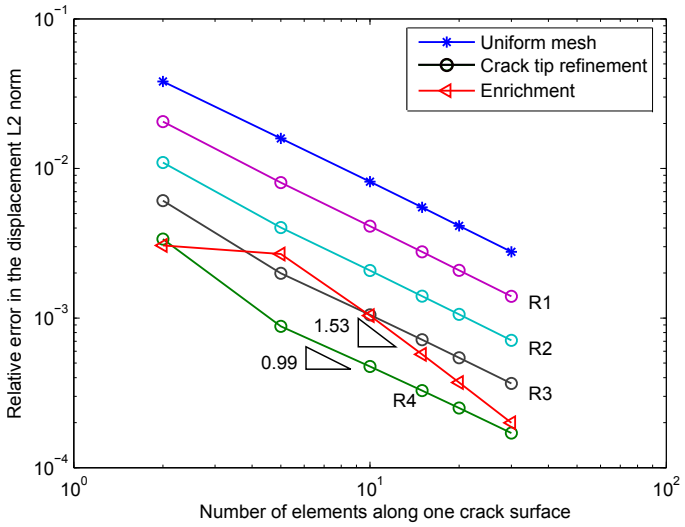

FIGURE 2.9: Relative error in L_2 norm of the displacement along the crack surface

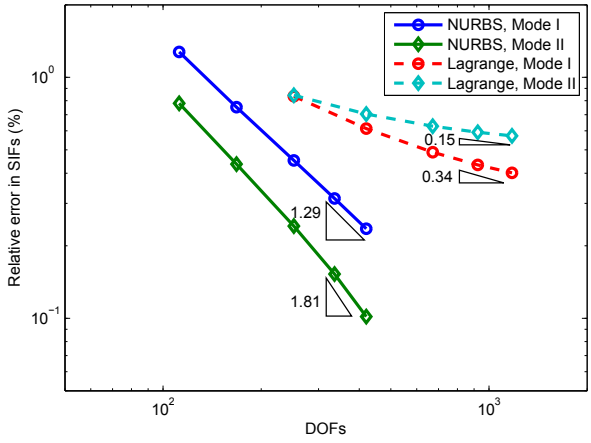

FIGURE 2.10: Convergence results of SIF for the mode I and mode II crack

integral is taken as the distance from the crack tip to the third collocation point counting from the crack tip, thus with mesh refinement, the extraction domain will shrink. A convergence check for the error in the normalized SIFs K_I, K_{II} is shown in Figure 2.10. It can be observed that the accuracy provided by NURBS basis is much higher (one order of magnitude for approximately 500 DOFs) than that of discontinuous Lagrange basis. Because discontinuous Lagrange basis typically leads to more nodes than NURBS basis for a given number of elements (as presented in Figure 2.3), the convergence results are re-plotted in terms of number of elements in Figure 2.11. For the two coarsest meshes of 4 elements per edge, the Lagrange basis is more accurate than NURBS, but with mesh refinement, the NURBS becomes superior, due to a larger convergence rate. From both figures, it is observed that the convergence rates of SIFs by NURBS basis is $5 \sim 8$ times higher than those by discontinuous Lagrange basis.

2.5.2 Inclined centre crack

In this example, The SIFs are calculated for a plate with an inclined crack under remote biaxial tension such that $\sigma = \sigma_0$ is applied in the y-direction and $\sigma = \lambda\sigma_0$ is applied in the x-direction, where λ is the load ratio and $\sigma_0 = 1$. The inclined centre crack with angle β varies from 0 to $\pi/2$, see Figure 2.12. The edge length of the plate $L = 1$, crack length $2a = 0.02$.

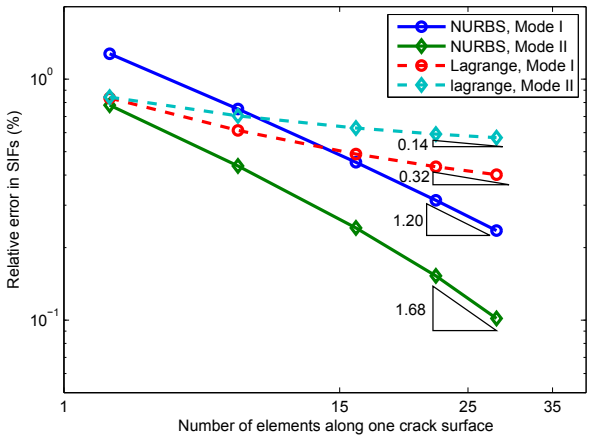

FIGURE 2.11: Convergence results of SIF for the mode I and mode II crack, plotting in terms of element number

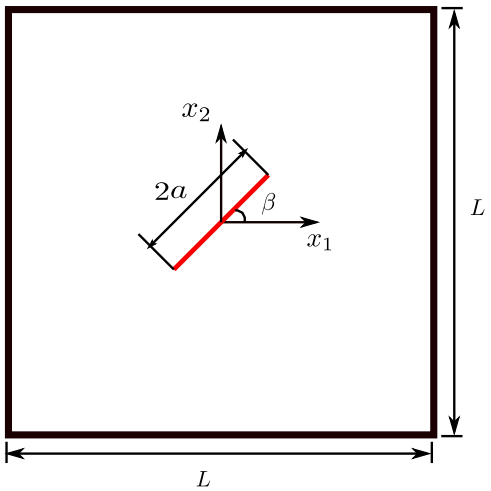

FIGURE 2.12: Physical model of an inclined center crack problem

$L >> a$ so that the numerical results can be compared with the analytical solution for an infinite plate, given in [149]. The elasticity parameters are $E = 1$, $\nu = 0.3$. The SIFs in this example obtained by the M integral can be compared to the analytical ones as follows:

$$K_I = \sigma\sqrt{\pi a}(\cos^2\beta + \lambda\sin^2\beta), \tag{2.51a}$$

$$K_{II} = \sigma\sqrt{\pi a}(1-\lambda)\cos\beta\sin\beta. \tag{2.51b}$$

The mesh of the crack surface was refined uniformly for both the discontinuous Lagrange basis BEM (LBEM) and NURBS (IGABEM). The local graded refinement for crack tip elements described in Figure 2.4 is also performed (the corresponding result is denoted as IGABEM(r), in this case no enrichment is applied). Assuming the number of elements for the crack is m, a convergence check is done with the crack angle $\beta = \pi/6$ at load ratio $\lambda = 0.5$ (biaxially loaded). The results are given in Table 2.1 and 2.2. Here the SGBEM results from uniform mesh refinement with special crack tip element [150] are also given as a reference. One can observed that SGBEM performs the best among these methods, while IGABEM with graded mesh refinement (IGABEM(r)) achieves an accuracy in the same order of SGBEM. It should be noted that SGBEM needs to deal with double integrals, which not only increase the computational cost but also add the complexity in coding, although better accuracy is shown. Thus it can be concluded that the proposed local crack tip refinement gives a very good accuracy for practical applications.

The SIFs are then compared for different angles at $\lambda = 0$ (uniaxially loaded). In this case, the crack is discretized by 4 uniform elements, and for IGABEM, the crack tip element is further refined in the same fashion. The SIFs are given in Tables 2.3 and 2.4.

	K_I/K_I^{exact}			
m	SGBEM	LBEM	IGABEM	IGABEM(r)
3	0.9913	1.00451	1.00982	1.00120
4	1.0002	1.00333	1.00769	1.00105
5	1.0001	1.00268	1.00633	1.00090
6	1.0002	1.00230	1.00539	1.00080
7	1.0003	1.00206	1.00474	1.00074
8	1.0003	1.00190	1.00426	1.00070
9	1.0003	1.00177	1.00389	1.00066
10	1.0003	1.00167	1.00359	1.00064
11	1.0003	1.00159	1.00336	1.00062
12	1.0003	1.00152	1.00316	1.00060
14	1.0003	1.00142	1.00285	1.00058

TABLE 2.1: Normalized K_I in inclined centre crack

	K_{II}/K_{II}^{exact}			
m	SGBEM	LBEM	IGABEM	IGABEM(r)
3	1.0075	1.00104	1.00647	1.00146
4	1.0009	1.00129	1.00656	1.00129
5	1.0010	1.00158	1.00607	1.00113
6	1.0009	1.00160	1.00550	1.00102
7	1.0014	1.00153	1.00500	1.00096
8	1.0005	1.00143	1.00458	1.00091
9	0.9997	1.00134	1.00424	1.00087
10	1.0009	1.00126	1.00396	1.00085
11	0.9992	1.00119	1.00373	1.00083
12	1.0013	1.00112	1.00353	1.00081
14	1.0004	1.00102	1.00322	1.00079

TABLE 2.2: Normalized K_{II} in inclined centre crack

	K_I		
β	Exact	IGABEM(r)	SGBEM
0	1.0000	$1.0006(6.0e-4)$	$1.0002(2.0e-4)$
$\pi/12$	0.9330	$0.9336(6.4e-4)$	$0.9332(2.1e-4)$
$\pi/6$	0.7500	$0.7505(6.7e-4)$	$0.7502(2.7e-4)$
$\pi/4$	0.5000	$0.5003(6.0e-4)$	$0.5001(2.0e-4)$
$\pi/3$	0.2500	$0.2501(4.0e-4)$	$0.2500(<1.e-4)$
$5\pi/12$	0.0670	$0.0670(<1.e-4)$	$0.0670(<1.e-4)$
$\pi/2$	0.0000	$0.0000(<1.e-4)$	$0.0000(<1.e-4)$

TABLE 2.3: SIFs and relative error (in brackets) for the inclined centre crack

	K_{II}		
β	Exact	IGABEM(r)	SGBEM
0	0.0000	$0.0000(<1.e-4)$	$0.0000(<1.e-4)$
$\pi/12$	0.2500	$0.2503(1.2e-3)$	$0.2502(8.0e-4)$
$\pi/6$	0.4330	$0.4336(1.4e-3)$	$0.4334(9.2e-4)$
$\pi/4$	0.5000	$0.5006(1.2e-3)$	$0.5004(6.0e-4)$
$\pi/3$	0.4330	$0.4335(1.2e-3)$	$0.4333(6.9e-4)$
$5\pi/12$	0.2500	$0.2503(1.2e-3)$	$0.2502(8.0e-4)$
$\pi/2$	0.0000	$0.0000(<1.e-4)$	$0.0000(<1.e-4)$

TABLE 2.4: SIFs and relative error (in brackets) for the inclined centre crack

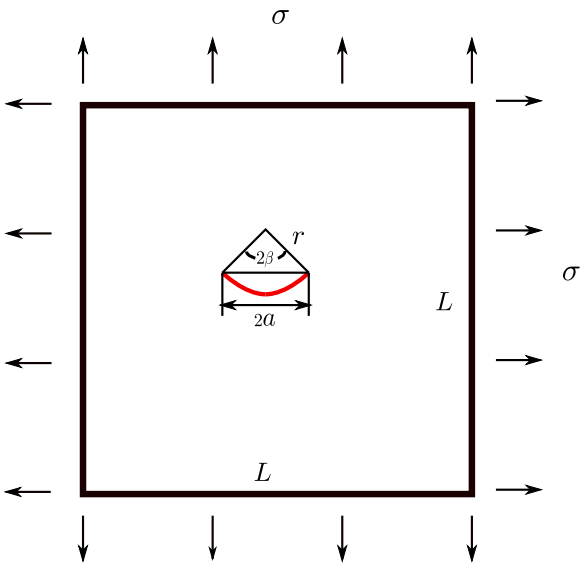

FIGURE 2.13: Physical model of the arc crack

2.5.3 Arc crack

The circular arc crack under remote uniform biaxial tension is used to further validate the effectiveness of the proposed method for curved cracks. The problem is defined in Figure 2.13. Here $L = 1$, $2a = 0.01$, $L >> a$, $E = 1$, $\nu = 0.3$. In the test $\sigma = 1, \beta = \pi/4$. The analytical SIFs are given by [151] as:

$$K_I = \sigma\sqrt{\pi a}\frac{\cos(\beta/2)}{1+\sin^2(\beta/2)}, \tag{2.52a}$$

$$K_{II} = \sigma\sqrt{\pi a}\frac{\sin(\beta/2)}{1+\sin^2(\beta/2)}. \tag{2.52b}$$

m elements are used to discretize each crack surface with crack tip elements refined as in Figure 2.4. A convergence check for the SIFs are listed in Table 2.5. Here the SIF extraction from both the J_k integral method and the M integral method are compared. Both methods use the same radius R, and the partition of the crack surface for the J_k integral is done by experience at $r = 0.03R, 0.04R, 0.05R, 0.06R, 0.07R$. The results of the two methods are comparable, differing only at the fourth digit. But we note that the J_k integral method is more computationally expensive than the M integral as (1) it needs integration on the crack surfaces; (2) the crack surface needs to be partitioned into two parts; (3) the integration needs to be performed several times as described in section 2.3.1.

	K_I/K_I^{exact}		K_{II}/K_{II}^{exact}	
m	M integral	J_k integral	M integral	J_k integral
10	1.00045	0.99972	0.97506	1.00309
14	1.00014	0.99979	0.98621	1.00248
17	1.00011	0.99982	0.98642	1.00217
20	1.00009	0.99985	0.98657	1.00195
23	1.00002	0.99987	0.99407	1.00176
26	1.00002	0.99989	0.99413	1.00163

TABLE 2.5: SIFs for the arc crack

2.5.4 Crack growth in a plate with rivet holes

The purpose of this example is to evaluate the potential of IGABEM for crack growth. The problem is chosen from the XFEM work by Moës *et*

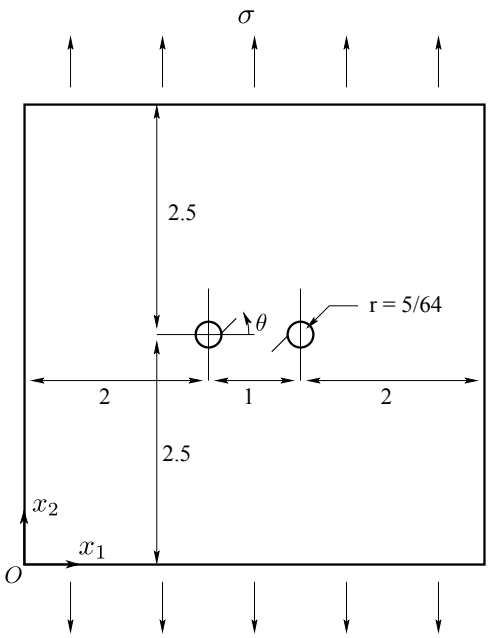

FIGURE 2.14: Physical model of rivet holes plate with initial cracks emanating from the holes. The initial crack lengths are 0.1, (Moës *et al*, 1999).

al [5]. The geometry and loading conditions are illustrated in Figure 2.14 ($\theta = \pi/4$, initial crack length $a = 0.1$). The material parameters $E = 1000$, $\nu = 0.3$. Below we compare three crack paths:

(1) the crack path, obtained by IGABEM (abbreviated as 'IGABEM');

(2) the crack path, obtained by XFEM in [5] (abbreviated as 'XFEM(M)');

(3) the crack path, obtained by the in-house double-interpolation XFEM code (abbreviated as 'XFEM*') by the author. More details regarding the proposed double-interpolation XFEM can be referred in appendix D.

For IGABEM crack growth 12 elements are used for each circle and 3 elements for each edge and for the initial cracks. The crack tip elements are further refined in the way described in section 2.4. We assume that each crack advances $\Delta a = 0.05$ at each step, which is identical to the increment chosen in [5] for the finest mesh. We grow the crack for 16 steps.

Next, all three crack paths - (1), (2) and (3) - are compared in Figure 2.15. The tip positions and SIFs for the left crack in each step are further compared in Table 2.6. It can be observed that the tip positions and the crack paths in all three cases are quasi-identical during propagation. From Figure 2.16 (a) we note that SIFs display significant difference in steps $9 \sim 12$.

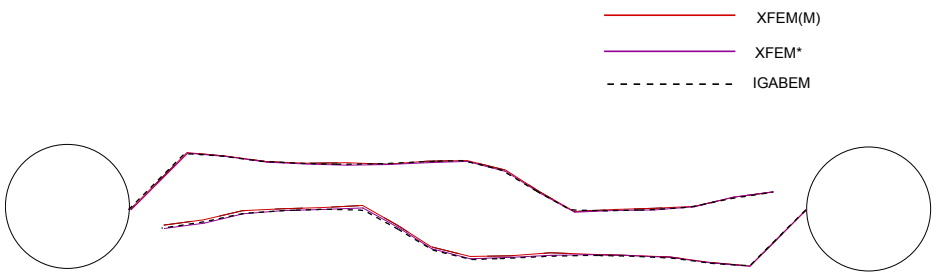

FIGURE 2.15: Crack path comparison. XFEM(M) is from Moës *et al*, 1999; XFEM* is from the in-house XFEM code

However, the crack growth direction is defined by the ratio K_{II}/K_I which is shown in 2.16 (b) and after these values of K_{II}/K_I are employed into the crack growth criteria, the final difference in the crack tip positions between all three paths does not exceed the difference in the third digital sign.

	IGABEM		XFEM*		XFEM(M)	
Step	x_c	y_c	x_c	y_c	x_c	y_c
Initial	2.1488	2.5707	2.1488	2.5707	2.1488	2.5707
1	2.1986	2.5665	2.1986	2.5662	2.1986	2.5663
2	2.2481	2.5596	2.2481	2.5593	2.2481	2.5595
3	2.2981	2.5575	2.2981	2.5570	2.2981	2.5575
4	2.3481	2.5564	2.3480	2.5556	2.3481	2.5581
5	2.3981	2.5573	2.3980	2.5564	2.3981	2.5562
6	2.4480	2.5598	2.4480	2.5587	2.4480	2.5600
7	2.4980	2.5614	2.4979	2.5604	2.4980	2.5608
8	2.5463	2.5485	2.5463	2.5477	2.5465	2.5488
9	2.5885	2.5217	2.5885	2.5209	2.5886	2.5219
10	2.6324	2.4978	2.6324	2.4968	2.6321	2.4972
11	2.6824	2.4986	2.6823	2.4990	2.6820	2.4998
12	2.7324	2.5000	2.7323	2.4997	2.7320	2.5013
13	2.7823	2.5035	2.7821	2.5036	2.7819	2.5037
14	2.8311	2.5144	2.8307	2.5157	2.8306	2.5151
15	2.8805	2.5217	2.8802	2.5223	2.8802	2.5217

TABLE 2.6: Tip position for left crack tip with $\Delta a = 0.05$. XFEM(M) is from Moës *et al*, 1999, XFEM* is from the in-house XFEM code

2.5.5 Three holes plate bending problem

A three point bending beam with three holes is simulated to further verify the robustness and accuracy of IGABEM for crack propagation. The geometry and loading conditions are illustrated in Figure 2.17. The material

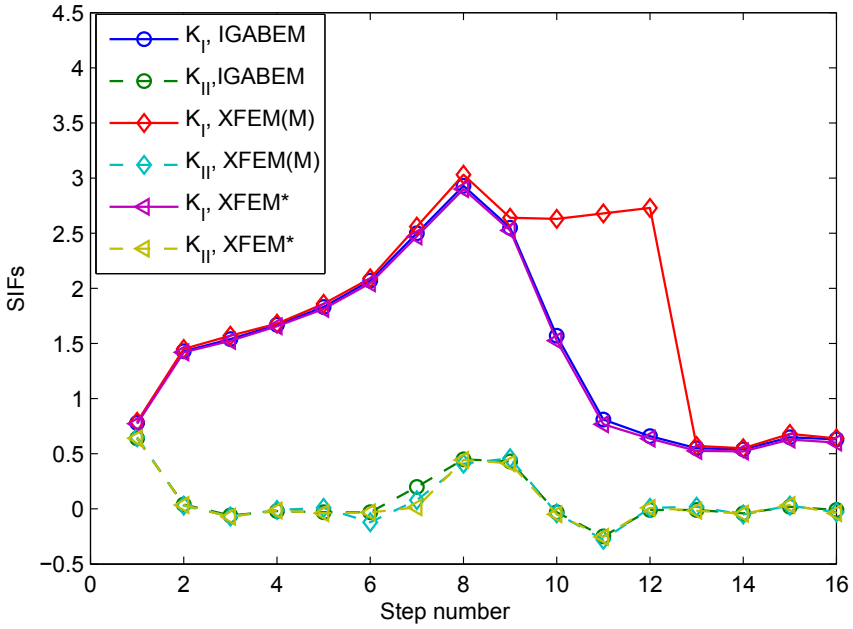

(a)

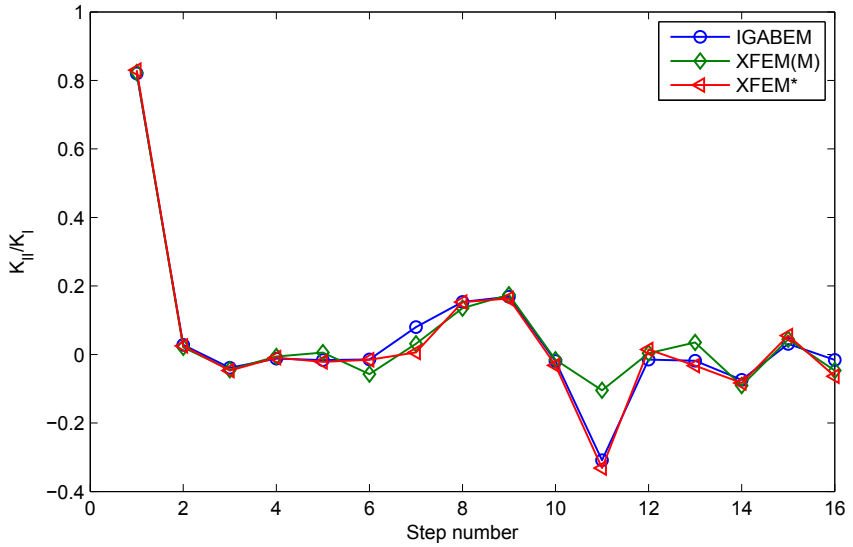

(b)

FIGURE 2.16: SIF comparison of the left crack tip for the whole process of crack propagation. XFEM(M) is from Moës *et al*, 1999, XFEM* is from the in-house XFEM code

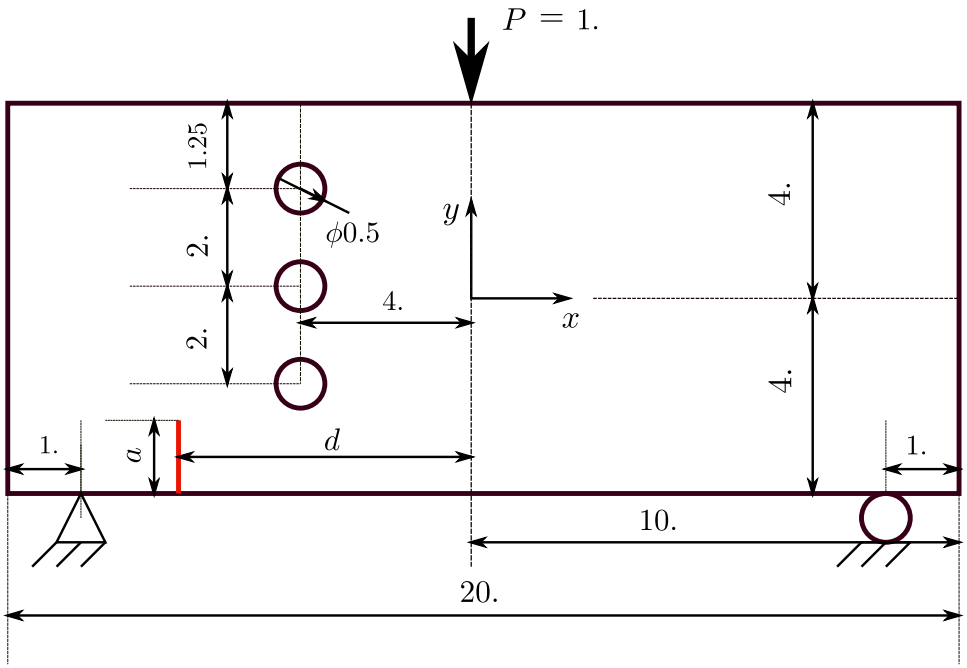

FIGURE 2.17: Physical model of the three point bending beam with 3 holes

parameters are $E = 1000$, $\nu = 0.37$. Plane strain conditions are assumed. With variation of the position of the initial crack, different crack trajectories were obtained experimentally in [152]. Here the position of the initial crack is set as $d = 5$, $a = 1.5$. This example has been solved using XFEM and XEFG [35] as well. The crack advance Δa is set to be 0.052 for both XFEM and IGABEM. The model is discretized by $27,869$ nodes and $55,604$ triangular elements for XFEM. And for IGABEM, 82 elements and 230 DOFs are used. Crack tip mesh refinement is used without enrichment. In [35], the XEFG model size is not given, but the crack increment $\Delta a = 0.1$. Figure 2.18 compares the crack growth paths using all the mentioned methods. All the crack paths agree well with the experiments. Of course, due to the differences in discretization and crack increment, the numerical results do differ. It can be observed that the IGABEM reproduces slightly better the experimental crack trajectory than the XFEM for the case when the crack passes through the first hole. Figure 2.19 compares the SIFs from XFEM and IGABEM. We note that significant difference in SIF values and the ratio of K_{II}/K_I occur when the crack passes near the first hole. A possible explanation for this could be that in XFEM, the domain used for SIF extraction is

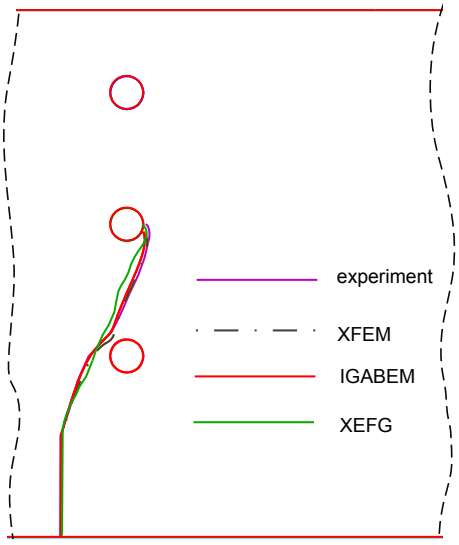

FIGURE 2.18: Crack paths (XEFG result $\Delta a = 0.1$ is from Ventura *et al*, 2002)

allowed to be intersected with the boundary of the domain.

2.5.6 Crack propagation in an open spanner

The last example consists in simulating the failure process of an open spanner due to crack propagation, in which the geometry is taken directly from CAD. The physical configuration is shown in Figure 2.20. As in industrial damage tolerance assessment [6], we assume that a small defect has initiated from the surface at the area of high stress concentration obtained from an elastostatic analysis [112]. The initial geometry including the crack is given in Figure 2.21. The crack will grow with $\Delta a = 0.1$. Figure 2.22 presents the deformed geometry with the crack. This example gives a straightforward illustration of the concept of seamless integration of CAD and failure analysis, since no mesh generator is required and the crack path is obtained directly from CAD.

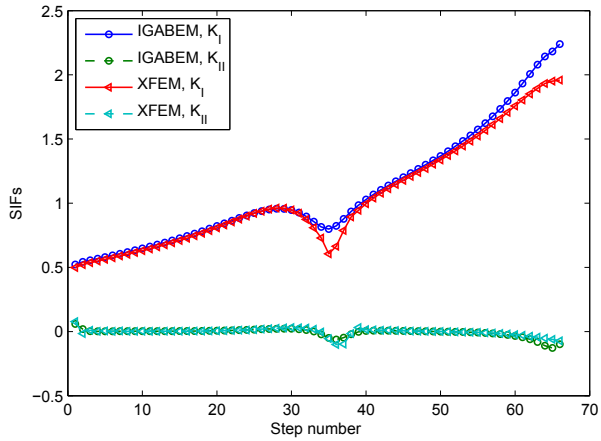

(a)

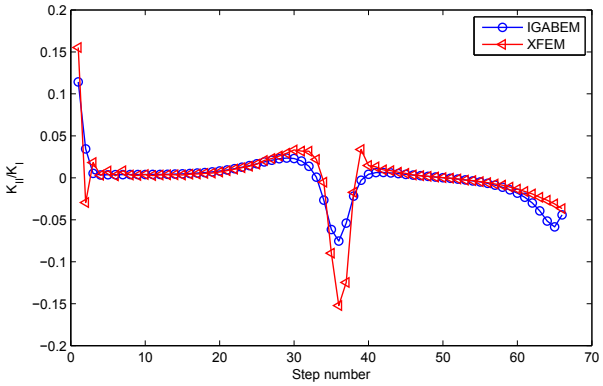

(b)

FIGURE 2.19: Comparison of the SIFs for the whole process of crack propagation

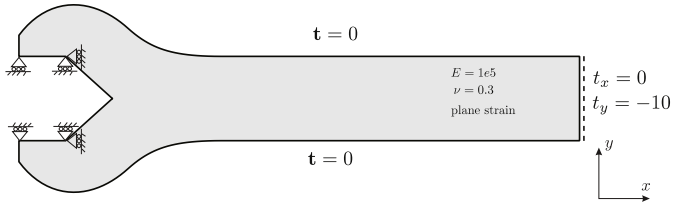

FIGURE 2.20: Boundary conditions, materials and geometry of the open spanner (Simpson *et al*, 2012)

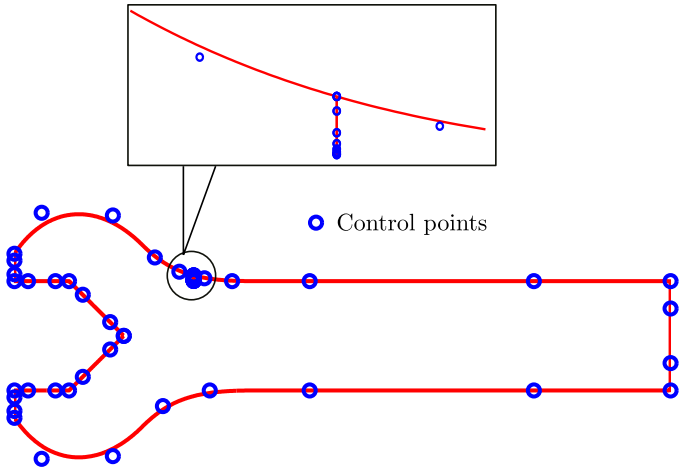

FIGURE 2.21: Control points and NURBS representation of the open spanner

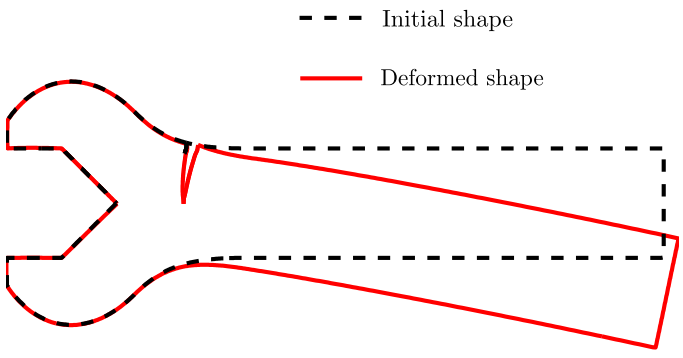

FIGURE 2.22: The deformed geometry after 10 steps of crack propagation

2.6 Conclusions

A detailed procedure to model linear elastic fracture problem using the NURBS based IGABEM is proposed in this work. The dual BIEs is introduced so that cracks can be modeled in a single domain. Different treatments for crack tip singularity are investigated including crack tip graded mesh refinement and partition of unity enrichment. The popular approaches to extract SIFs are compared in the framework of IGABEM and it proves that the M integral is more efficient for SIF extraction in IGABEM. The cracks are modeled directly by NURBS, and an algorithm for modifying the NURBS curve is implemented to describe the crack propagation. Numerical examples shows that:

(1) The IGABEM can obtain a higher accuracy than Lagrange basis based BEM for the same model size or DOFs. The convergence rate in SIFs has been improved by $5 \sim 8$ times than BEM with discontinuous Lagrange basis without any treatment to the crack tip;

(2) Both crack tip graded mesh refinement and enrichment can improve the displacement field near the crack tip, and the graded mesh refinement is selected to apply in the crack growth;

(3) The proposed crack growth procedure can lead to C^1 smooth crack trajectory and agrees well with those results from XFEM.

(4) A procedure for damage tolerance assessment directly from CAD is presented, which does not require any mesh (re)generation.

The extension of IGABEM to 3D fracture growth simulation seems more appealing due to benefit brought by the reduction of mesh burden. And the solution provided by the BEM with the smooth geometry and crack representation is expected to be helpful in SIFs evaluation. The next chapter will look into the 3D development.

Chapter 3

IGABEM for 3D linear elastic fracture

Based on the paper '*Isogeometric boundary element methods for three dimensional fatigue crack growth*' submitted to CMAME

The isogeometric boundary element method (IGABEM) based on NURBS is adopted to model fracture problem in 3D. The NURBS basis functions are used in both crack representation and physical quantity approximation. A stable quadrature scheme for singular integration is proposed to enhance the robustness of the method in dealing with highly distorted element. The convergence study in crack opening displacement is performed for penny-shaped crack and elliptical crack. Two ways to extract stress intensity factors (SIFs), the contour M integral and virtual crack closure integral, are implemented based on the framework of dual integral equations. An algorithm is outlined and validated to be stable for fatigue crack growth, thanks to the smoothness not only in crack geometry but also in stress/SIFs solution brought by IGABEM.

3.1 Boundary integral equations for crack modeling

For 3D case, the crack can be modeled by the method of dual boundary integral equations. For cracks in infinite domain, the crack opening displacement equation gives a simpler implementation. Details of the formulation can be referred in section 2.2.1 of the previous chapter.

3.2 NURBS discretization and collocation

The formulation of 1D NURBS basis functions is briefed in section 2.1. Given the knot vectors $\Xi = \{\xi_1, \xi_2, ..., \xi_{n+p+1}\}$ and $\mathscr{H} = \{\eta_1, \eta_2, ..., \eta_{m+q+1}\}$, and the control points net $P_{i,j}$. The B-spline surface $S(\xi, \eta)$ is given by the tensor-product of B-spline basis functions defined in the 2D parametric domain $[\xi_1, \xi_{n+p+1}] \times [\eta_1, \eta_{m+q+1}]$,

$$S(\xi, \eta) = \sum_{i=1}^{n} \sum_{j=1}^{m} N_{i,p}(\xi) M_{j,q}(\eta) P_{i,j}, \tag{3.1}$$

where $N_{i,p}(\xi)M_{j,q}(\eta)$ are the 2D B-spline basis functions. The NURBS basis functions can be constructed by rationalizing the tensor-product B-spline basis functions as

$$R_{i,j}(\xi, \eta) = \frac{N_{i,p}(\xi) M_{j,q}(\eta) w_{i,j}}{\sum_{k=1}^{n} \sum_{l=1}^{m} N_{k,p}(\xi) M_{l,q}(\eta) w_{k,l}}, \tag{3.2}$$

where the scalar variable $w_{i,j}$ is the weight associated with the control point $P_{i,j}$. For integration, the 2D NURBS basis functions are usually calculated in the element defined by the non-zero knot intervals $[\xi_i, \xi_{i+1}] \times [\eta_j, \eta_{j+1}]$ where the Gaussian rule can be applied [87].

The Greville abscissae has been used to generate the collocation points. For a closed domain composed by trimless and compatible NURBS patches, the number of collocation points obtained by the Greville abscissae is identical to the number of control points (or basis functions), which means one collocation point is associated with one control point.

Remark: *for those collocation points lie in the sharp edges or corners, or when discontinuous basis functions are needed, these collocation points will be offset from the original place by*

$$\begin{aligned} &\xi_{s,i} = \xi_{s,i} + \alpha(\xi_{s,i+1} - \xi_{s,i}), \quad \textit{or} \\ &\xi_{s,i} = \xi_{s,i} - \alpha(\xi_{s,i} - \xi_{s,i-1}), \quad 0 < \alpha < 1. \end{aligned} \tag{3.3}$$

Note that in this case, the associated control points should be doubled such that

the discontinuous basis functions are obtained, or the BIEs on the offset collocation points should be merged into one BIE, such that the number of equations and unknowns remains equal.

3.3 Numerical integration

Due to the singularities in BIEs, there will be singular integration and non-singular integration after discretization. For the element containing the collocation point, singular integration is performed and the element belongs to singular elements. Elements which exclude the collocation point are called non-singular elements. Singular integration needs to be carefully treated in BEM. Various numerical methods have been proposed, and one can refer to a review work in [40]. A robust technique developed in [132] can be applied to regularized all the singular terms into weakly singular terms, via the use of simple solution of BIE. The regularization technique based on simple solutions has been further developed in the framework of IGA-BEM [113][153][126]. However, this method fails when dealing with open surfaces such as cracks because of the existence of two jump terms in collapsed boundary [127]. In the present work, we use the singularity subtraction technique (SST) proposed by Guiggiani [127][128] to remove the singularities arising in both BIEs. The SST is a method for the treatment of singular integrals regardless of mesh dicretization and proved to be efficient for fracture via dual BEM [42].

3.3.1 Singularity subtraction technique (SST) for singular integrals

The SST transforms various orders of singular integration into a weakly singular one based on the intrinsic coordinate system of the singular element after discretization. Then the weakly singular integration becomes regular if the quadrature is performed in polar coordinates. By expanding the integrand into a series with respect to the intrinsic coordinates, the singularity can be represented explicitly with respected to the parametric

distance between the source point and field point ρ. Then the singular terms are subtracted from the integrand, leaving the remaining to be regular for which regular Gaussian rule is applied. the subtracted terms are added back semi-analytically. Assume that the coordinates of the point of interest are $\mathbf{x}(x_i = x, y, z)$ in physical space, $\boldsymbol{\xi}(\xi_i = \xi, \eta)$ in the parametric space of the NURBS basis functions and $\bar{\boldsymbol{\xi}}(\bar{\xi}_i = \bar{\xi}, \bar{\eta})$ in the parent space $[-1, 1] \times [-1, 1]$. For the hyper-singular integral of the form

$$I = \neq\!\!\!\!\int_S S(\mathbf{s}, \mathbf{x}(\bar{\boldsymbol{\xi}}))R(\bar{\boldsymbol{\xi}})\bar{J}(\bar{\boldsymbol{\xi}})\mathrm{d}S, \tag{3.4}$$

where $S(\mathbf{s}, \mathbf{x}(\bar{\boldsymbol{\xi}}))$ is the hyper-singular kernel, $R(\bar{\boldsymbol{\xi}})$ is the NURBS basis function and $\bar{J}(\bar{\boldsymbol{\xi}})$ is the Jacobi transformation from parent space to physical space (Figure 3.1). The polar coordinates $\boldsymbol{\rho}(\rho, \theta)$ centred at the source point are introduced in the parent space. The parent domain is subdivided into triangles for quadrature. For each field point $\bar{\boldsymbol{\xi}}$ in the sub-triangles, we have

$$\begin{aligned} \bar{\xi} &= \bar{\xi}_s + \rho\mathrm{cos}\theta, \\ \bar{\eta} &= \bar{\eta}_s + \rho\mathrm{sin}\theta, \end{aligned} \tag{3.5}$$

After the polar coordinate transformation, Equation (3.4) becomes

$$I = \lim_{\varepsilon \to 0} \int_0^{2\pi} \int_{\alpha(\varepsilon,\theta)}^{\hat{\rho}(\theta)} S(\rho, \theta)R(\rho, \theta)\bar{J}(\rho, \theta)\rho\mathrm{d}\rho\mathrm{d}\theta, \tag{3.6}$$

where $\hat{\rho}(\theta) = h/\mathrm{cos}\bar{\theta}$. h is the shortest distance from the source point to the element edge and $\bar{\theta}$ is the angle from perpendicular direction to the field point as in Figure 3.1. If we define θ_0 as the angle of the perpendicular line, then the angle to the field point can be computed as

$$\theta = \bar{\theta} + \theta_0. \tag{3.7}$$

The integrand $F(\rho, \theta) = S(\rho, \theta)R(\rho, \theta)\bar{J}(\rho, \theta)\rho$ is expanded as:

$$F(\rho, \theta) = \frac{F_{-2}(\theta)}{\rho^2} + \frac{F_{-1}(\theta)}{\rho} + F_0(\theta) + F_1(\theta)\rho + F_2(\theta)\rho^2 + \cdots = \sum_{i=-2}^{\infty} F_i(\theta)\rho^i. \tag{3.8}$$

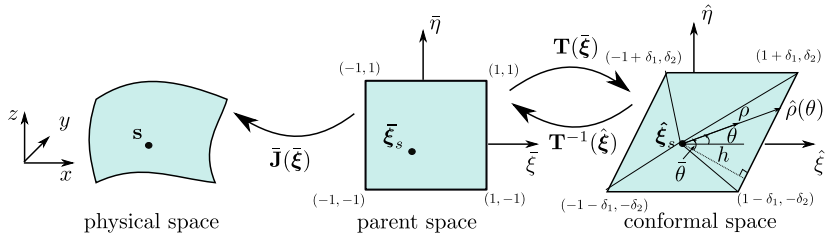

FIGURE 3.1: Transformation between coordinate system for SST

The first two singular terms on the right hand side are subtracted and added back semi-analytically, resulting in:

$$
\begin{aligned}
I &= I_1 + I_2, \\
I_1 &= \int_0^{2\pi} \int_0^{\hat{\rho}(\theta)} \Big[F(\rho,\theta) - \frac{F_{-2}(\theta)}{\rho^2} - \frac{F_{-1}(\theta)}{\rho} \Big] \mathrm{d}\rho \mathrm{d}\theta, \\
I_2 &= \int_0^{2\pi} I_{-1}(\theta) \ln \frac{\hat{\rho}(\theta)}{\beta(\theta)} \mathrm{d}\theta - \int_0^{2\pi} I_{-2}(\theta) \Big[\frac{\gamma(\theta)}{\beta^2(\theta)} + \frac{1}{\hat{\rho}(\theta)} \Big] \mathrm{d}\theta,
\end{aligned}
\tag{3.9}
$$

where I_1 is regular and I_2 are regular line integrals, Both can be applied with Gaussian quadrature rule. The evaluation of $\alpha(\varepsilon,\theta)$, $\beta(\theta)$ and $\gamma(\theta)$ as well as the limiting process are given in appendix B.2 and more details can be referred in [128].

3.3.2 Conformal mapping for SST

It has been revealed by Rong *et al* [154] that the expansion coefficients $F_i(\theta)$ in Equation (3.8) exhibits various orders of near-singularity in the angular θ direction, although the singularity in the radial ρ direction disappears. This near-singularity is sensitive to the shape of the element and becomes severe when the element is highly distorted. The $F_i(\theta)$ can be represented as:

$$
F_i(\theta) = \frac{\tilde{F}_i(\theta)}{A^p(\theta)} = \frac{\tilde{F}_i(\theta)}{[0.5(|\mathbf{m}_1^s|^2 + |\mathbf{m}_2^s|^2)(\omega \sin(2\theta + \varphi) + 1)]^{p/2}}, \tag{3.10}
$$

where $\tilde{F}_i(\theta)$ are the regular trigonometric functions and integer 'p' is the order associated with 'i'. The curvi-linear basis vectors $\mathbf{m}_i^s = \mathbf{m}_i|_{\bar{\boldsymbol{\xi}}=\bar{\boldsymbol{\xi}}_s}, (i =$

$1, 2)$ and are calculated as:

$$\begin{aligned} \mathbf{m}_1 &= \Big[\frac{\partial x}{\partial \bar{\xi}}, \frac{\partial y}{\partial \bar{\xi}}, \frac{\partial z}{\partial \bar{\xi}}\Big], \\ \mathbf{m}_2 &= \Big[\frac{\partial x}{\partial \bar{\eta}}, \frac{\partial y}{\partial \bar{\eta}}, \frac{\partial z}{\partial \bar{\eta}}\Big]. \end{aligned} \tag{3.11}$$

We introduces two parameters

$$\begin{aligned} \lambda &= |\mathbf{m}_1^s|/|\mathbf{m}_2^s|, \\ \cos\psi &= \mathbf{m}_1^s \cdot \mathbf{m}_2^s/|\mathbf{m}_1^s||\mathbf{m}_2^s|, \end{aligned} \tag{3.12}$$

such that

$$\begin{aligned} \varphi &= \arctan\frac{\lambda^2 - 1}{2\lambda\cos\psi}, \\ \varpi &= \sqrt{1 - \frac{4\sin^2\psi}{(\lambda + \lambda^{-1})^2}} < 1. \end{aligned} \tag{3.13}$$

It can be concluded that when the element aspect ratio is large or the angle between two basis vectors tends to 0 or π ($\sin\psi \to 0$), $A(\theta)$ will tend to 0, resulting in the near-singularity of $F_i(\theta)$. Both scenarios indicate a distorted shape of the singular element, which are common in isogeometric analysis.

Rong *et al* [154] constructed the conformal mapping from the parent space $(\bar{\xi}, \bar{\eta})$ to a new parametric space $(\hat{\xi}, \hat{\eta})$ where the two curvi-linear basis vectors in the new parametric space are orthogonal and have identical length, i.e.

$$\begin{aligned} \hat{\mathbf{m}}_1^s \cdot \hat{\mathbf{m}}_2^s &= 0, \\ |\hat{\mathbf{m}}_1^s| &= |\hat{\mathbf{m}}_2^s|. \end{aligned} \tag{3.14}$$

Then $A(\theta)$ becomes a constant, which makes the integration nonsensitive to the element shape, if the series is expanded in the new space. The quadrature for the singular integral turns to be stable regardless of mesh distortion.

The mapping proposed by Rong *et al* is tailored for triangular element, in this work we extend it to the quadrilateral elements (Figure (3.1)). In

[154], the Jacobian transformation matrix $\mathbf{T}$ from $\bar{\boldsymbol{\xi}} = (\bar{\xi}, \bar{\eta})$ to a new parametric space $\hat{\boldsymbol{\xi}} = (\hat{\xi}, \hat{\eta})$ is

$$\mathbf{T} = \begin{bmatrix} 1 & \delta_1 \\ 0 & \delta_2 \end{bmatrix}, \text{ so that } \hat{\boldsymbol{\xi}} = \mathbf{T}\bar{\boldsymbol{\xi}}, \tag{3.15}$$

where $\delta_1 = \cos\psi/\lambda$, $\delta_2 = \sin\psi/\lambda$. Then the new basis vectors

$$\begin{bmatrix} \hat{\mathbf{m}}_1^s & \hat{\mathbf{m}}_2^s \end{bmatrix} = \begin{bmatrix} \mathbf{m}_1^s & \mathbf{m}_2^s \end{bmatrix} \mathbf{T}^{-1} = \begin{bmatrix} \mathbf{m}_1^s & -(\delta_1/\delta_2)\mathbf{m}_1^s + (1/\delta_2)\mathbf{m}_2^s \end{bmatrix} \tag{3.16}$$

will satisfy the relation in Equations (3.14). The bilinear interpolation is used from $(\bar{\xi}, \bar{\eta})$ to the new parametric space $(\hat{\xi}, \hat{\eta})$ for a quadrilateral element:

$$\begin{aligned} \hat{\boldsymbol{\xi}} &= \sum_{I=1}^{4} N_I(\bar{\boldsymbol{\xi}})\hat{\boldsymbol{\xi}}^I, \\ N_1(\bar{\xi}, \bar{\eta}) &= 0.25(1+\bar{\xi})(1+\bar{\eta}), \\ N_2(\bar{\xi}, \bar{\eta}) &= 0.25(1-\bar{\xi})(1+\bar{\eta}), \\ N_3(\bar{\xi}, \bar{\eta}) &= 0.25(1-\bar{\xi})(1-\bar{\eta}), \\ N_4(\bar{\xi}, \bar{\eta}) &= 0.25(1+\bar{\xi})(1-\bar{\eta}). \end{aligned} \tag{3.17}$$

Combining Equations (3.15) and (3.17), the nodal coordinates $\hat{\boldsymbol{\xi}}^I$ can be obtained as $\hat{\boldsymbol{\xi}}^1(1+\delta_1, \delta_2)$, $\hat{\boldsymbol{\xi}}^2(-1+\delta_1, \delta_2)$, $\hat{\boldsymbol{\xi}}^3(-1-\delta_1, -\delta_2)$ and $\hat{\boldsymbol{\xi}}^4(1-\delta_1, -\delta_2)$. It should be noted that since $0 < \psi < \pi$, $\delta_2 > 0$, the quadrilateral element is guaranteed to have positive area (one possible plot is shown in Figure (3.1)). This requires the source point to be located at the degenerated point in the geometry where $|\mathbf{m}_i^s| \neq 0$.

It can be seen from Figure 3.1 that the shape of the element in conformal space is controlled by the coefficients δ_1 and δ_2. This means that if λ (reflecting the element aspect ratio) and $\cos\psi$ (reflecting the element distortion) deviate from 1, the conformal element will be skewed. This will result in sub-triangles with $\bar{\theta}$ approaching $\pm\pi/2$ if the field point is close to the edges adjacent to the source point of the sub-triangles (Figure 3.1). Thus $\hat{\rho}(\theta) = h/\cos\bar{\theta}$ is not calculated accurately. To alleviate this near singularity

in $\hat{\rho}(\theta)$, the following Sigmoidal transformation is applied in the angular direction such that the integration points will be adaptively clustered close to the edges where the near-singularity is severe, according to the value of $\bar{\theta}$ [154],

$$\begin{aligned} w(\bar{\theta}) &= \frac{1}{\pi}\Big(\bar{\theta}+\frac{\pi}{2}\Big), \quad -\frac{\pi}{2}<\bar{\theta}<\frac{\pi}{2}, 0<z<1, \\ z = z(s) &= w(\bar{\theta}_1)+\frac{1}{2}(s+1)(w(\bar{\theta}_2)-w(\bar{\theta}_1)), \quad -1<s<1, \\ & \qquad 0\le z(\bar{\theta}_1)<z<z(\bar{\theta}_2)\le 1, \\ f(z) &= \frac{z^m}{z^m+(1-z)^m}, \\ \bar{\theta} &= \pi f(z)-\frac{\pi}{2}, \\ J^{-1}(\theta) &= \frac{\partial\theta}{\partial s} = \frac{\pi[w(\bar{\theta}_2)-w(\bar{\theta}_1)]mf(z)^{m-1}}{2(f(z)^m+(1-f(z))^m)^2}, \end{aligned} \tag{3.18}$$

where s is the Gauß point in interval $(-1,1)$, the relation of θ and $\bar{\theta}$ can be found in Equation (3.7).

3.3.3 Numerical quadrature

In our numerical implementation, the Gaussian rule is applied in both radial and angular direction. 6 Gauß points are used in the radial direction. 18 Gauß points are used in the angular direction of each sub-triangle for conformal SST unless otherwise specified. For each non-singular element, an adaptive subdivision scheme is used according to the relative distance between the element and collocation point. All the rules are used empirically without any error control algorithm.

3.4 Crack growth

The approaches used to represent and track the crack propagation can be classified into two manifolds, implicit and explicit methods. A typical application of the former method would be the level set method [155] which was coupled in the XFEM/GFEM to represent and grow the discontinuity

[28][29]. The level set function is a signed distance function to the crack surface defined on the underlying mesh, which could be either consistent with the mesh discretization of the problem or an independent structured mesh. Since the cracks are open surfaces, one more level set function, perpendicular to the crack surface is required in order to describe the crack front. The quality to represent the crack surface depends on the resolution of the underlying mesh. Accurately describing the crack surface usually introduces additional computational expense [156]. Advection-type equations should be solved so as to update the crack front when the crack evolves [157] which increases the computational effort. Chopp and Sukumar [158] proposed the fast marching method to update the crack front, thus facilitating the process of updating the crack surface [27]. Fries and Baydoun [159] proposed an implicit-explicit method, in which the level set represented crack is explicitly dicretized by triangular facets. Analogous idea is the vector level set method [35]. These methods take advantage of the level set representation for the PU enrichment while avoiding to update the crack surface by solving the equations. Additionally, sharp turns and kinks can be retained by use of explicit crack surfaces rather than pure level sets.

The explicit method uses sets of triangular or quadrilateral facets to discretize the crack surface directly. For finite element based methods, the crack evolution process is usually accompanied with an automatic re-meshing operation. For XFEM/GFEM applications, the subdivision of the 3D solid elements needs to be performed for the integration purpose. Both relies on well-developed meshing/re-meshing packages [160][161]. The explicit representation of the crack surfaces by triangulation has been used in meshfree methods as well [33][36][37]. It should be noted that this representation method usually results in a C^0 crack surface and that the crack fronts are composed of line segments. This leads to at least two shortcomings: (1) The crack front is not smooth which leads to inaccuracies in the extraction of the fracture parameters (for example the SIFs). Geometry approximation error accumulates as the crack grows; (2) The local crack front coordinate system is not well defined and the deflection angle is discontinuous, resulting in

non-unique branch enrichment values for some points on the crack front. One approach to alleviate this is to abandon the branch enrichment [36][37]. As a remedy, the crack fronts need to be smoothed through some numerical techniques [160][161]. Similar scenarios occur in Lagrange based BEM for fracture modeling. Besides, Paluszny and Zimmerman [147] points out that a large number of facets are needed in order to more accurately represent the crack surface so that the storage increases rapidly with respect to the area of the crack surface when the cracks propagate. Hence they propose the use of a parametric surface, i.e. the NURBS patch, to describe the crack propagation. In their approach, crack growth is realized geometrically by deforming the NURBS surface through the mid-range La-Greca algorithm [146] to move the control points. Due to the parametrization of the NURBS patch, the crack tip can be sampled anywhere along the crack front, thus the storage for crack discretization increases mildly. Meanwhile the local crack front coordinate system is established on the smooth geometry. However, this method is based on re-meshing the finite elements. Recently Tambat *et al* proposed an explicitly represented lower-dimension geometry features by NURBS [104][105] through the partition of unity approximation. Instead of using level sets, the lower-dimension features such as cracks are accurately described through the calculation of the distance field in an efficient non-iterative way, providing a promising alternative to evolve discontinuities in the IGAFEM framework. However, more suitable numerical quadrature scheme are still desired in order to fully exploit the exact representation in geometry.

In the present work, we use NURBS patches to discretize the crack surfaces. The crack front is exactly described and the local crack tip system is defined naturally and uniquely based on the NURBS patch. Meanwhile, the physical quantities are also approximated by the NURBS basis in the spirit of isogeomtric analysis. With BEM, the smoothness in geometry and stress solution is fully exploited to calculate the fracture parameters and evolve the cracks. In the following section, we first introduce the ways to extract the stress intensity factors, based on the NURBS crack surfaces and recall

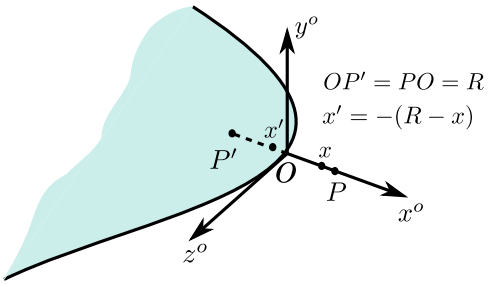

FIGURE 3.2: Crack tip coordinate system

the Paris law to calculate the crack advance. With these governing fracture parameters, a crack surface updating algorithm is outlined to perform the crack growth.

3.4.1 Computation of stress intensity factors

The driving force for the evolution of fatigue fracture is characterized by some fracture parameters such as the stress intensity factors (SIFs), which can be extracted from the numerical solution. If the fracture parameters are computed based on the point-wise tips on the crack front independently, the approach can be considered as 'local'. The key factor to compute accurately the SIFs in a local approach is to avoid discretization and path dependence. In this section both the virtual crac kclosure integral (VCCI) and the contour M integral have been investigated for the calculation of SIFs in fracture analysis via the 3D isogeometric BEM. A point-wise crack tip coordinate system is established along the crack front as in Figure 3.2. The physical quantities are all in the crack tip local coordinate system thus the superscript 'o' is omitted in this section.

Contour M integral

The definition of the J_k integral stems from two dimensions as:

$$J_k := \lim_{\Gamma_\epsilon \to 0} \int_{\Gamma_\epsilon} (W\delta_{jk} - \sigma_{ij}u_{i,k})n_j \mathrm{d}\Gamma = \lim_{\Gamma_\epsilon \to 0} \int_{\Gamma_\epsilon} P_{kj}n_j \mathrm{d}\Gamma, \quad k = 1, 2 \quad (3.19)$$

where P_{kj} is the Eshelby tensor, $W = 1/2\sigma_{ij}\epsilon_{ij}$ is the strain energy density. Γ_ϵ is a small contour with radius R centred at the point 'o' on the crack front in the '$x_o - y_o$' plane and n_j is the unit outward normal of Γ_ϵ.

This 2D definition can be extended to a three dimensional point-wise definition by taking a tubular surface around the crack front. When the contour Γ_ϵ is small enough, plane strain conditions are approximately satisfied. The contour definition can thus be used directly on the premise that a sufficiently small contour is assumed. For more details, see section 2.3.2

Virtual crack closure integral

In the VCCI, the strain energy release rate is equal to the work done by closing the crack along its extension. The modes of the strain energy release rate are given by

$$\begin{aligned} G_I &= \frac{1}{2R}\int_0^R \sigma_{yy}(x)[\![u_y(x')]\!]\mathrm{d}x, \\ G_{II} &= \frac{1}{2R}\int_0^R \sigma_{xy}(x)[\![u_x(x')]\!]\mathrm{d}x, \\ G_{III} &= \frac{1}{2R}\int_0^R \sigma_{yz}(x)[\![u_z(x')]\!]\mathrm{d}x, \end{aligned} \tag{3.20}$$

where $PO = R$ is the virtual crack advance and $x' = -(R - x)$. The crack opening displacement $[\![u_j(x')]\!] = u_j^+(x') - u_j^-(x')$. For the evaluation of $[\![u_j(x')]\!]$ on OP', the point inversion algorithm needs to be performed in order to find the parametric coordinates in the crack modeled by the NURBS surface [129]. The domains of these integrals OP' and PO are dicretized by a single linear element [162]. R is identical for all the sample points on the crack front. Then K_I, K_{II} and K_{III} can be computed according to Equation (C.5).

3.4.2 Paris law

The Paris-based laws are typical empirical relation linking the increment in crack advance $\mathrm{d}a$ occurring during $\mathrm{d}N$ cycles to the SIF amplitude, though empirically obtained coefficients C and m. The simplest expression of Paris

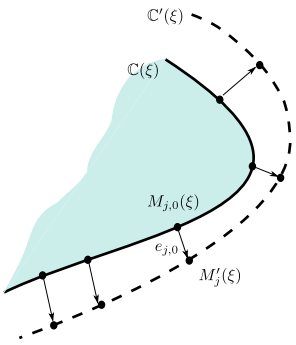

FIGURE 3.3: Crack front updating. $\mathbb{C}(\xi)$ is the old crack front curve, $\mathbb{C}'(\xi)$ is the new crack front curve after crack advance

law reads:

$$\frac{\mathrm{d}a}{\mathrm{d}N} = C(\Delta K)^m, \tag{3.21}$$

For mixed mode fracture, K is taken as the equivalent SIF K_{eq} which is given as [24]:

$$K_{\text{eq}} = \sqrt{K_I^2 + K_{II}^2 + (1+\nu)K_{III}^2} \tag{3.22}$$

It should be noted that the crack propagation velocity could be varied for the points along the front. In a single propagation step, the crack advance for each point is regularized by the user-specified maximum increment of crack advance $\Delta a^{\max}$,

$$\Delta a^i = C(\Delta K_{\text{eq}}^i)^m \frac{\Delta a^{\max}}{C(\Delta K_{\text{eq}}^{\max})} = \Delta a^{\max}\Big(\frac{\Delta K_{\text{eq}}^i}{\Delta K_{\text{eq}}^{\max}}\Big)^m, \tag{3.23}$$

where 'i' denotes the i-th sample point on the crack front.

The maximum hoop stress criterion is used to determine the direction of crack propagation. We assume, at each point on the crack front, that the crack propagates in the direction θ_c such that the hoop stress is maximum. This is given by the following expression [145]

$$\theta_c = 2\arctan\left[\frac{-2(K_{II}/K_I)}{1+\sqrt{1+8(K_{II}/K_I)^2}}\right]. \tag{3.24}$$

3.4.3 Crack surface updating algorithm

Crack propagation is realized geometrically by advancing the crack front so that the new crack front curve $\mathbb{C}'(\xi)$ passes through the new positions of the sample points on the old crack front curve $\mathbb{C}(\xi)$ which is parameterized by the knot vector $\Xi = \{\xi_1, \xi_2, ..., \xi_{n+p+1}\}$, n is the number of basis functions. We define the sample points on $\mathbb{C}(\xi)$ to be $M_j = \mathbb{C}(\xi_j), j = 0, 1, ..., N-1$, and the set of corresponding new positions to be $M'_j = \mathbb{C}'(\xi_j)$ and we set $N = n$ here. Note that each M'_j is calculated via the fracture parameters K and Δa introduced in the previous section. We adopt the algorithm described in [146] to generate a new curve which passes through all the new sample points by updating the control points of the old curve through a iterative process. For t-th iteration step, we define the error vector $\mathbf{e}_t$ as:

$$e_{j,t} = \overrightarrow{M_{j,t}M'_j}, \quad j = 0, 1, ..., N-1. \tag{3.25}$$

Note that when $t = 0$, $e_{j,t} = \overrightarrow{M_{j,0}M'_j} = \overrightarrow{M_jM'_j} = \Delta a_j$ which is the crack advance of the point on the crack front. If $\|\mathbf{e}_t\| < tol$, the iteration ceases and the new crack front curve is obtained.

To update the control points, we define a motion vector $\mathbf{m}_t$ for the control points such that at the t-th iteration step:

$$P_{i,t} = P_{i,t-1} + m_{i,t}, \quad i = 0, 1, ..., n-1, \tag{3.26}$$

with $P_{i,0} = P_i$ which are the control points of the old crack front $\mathbb{C}$. The motion vector $\mathbf{m}_t$ can be computed as:

$$m_{i,t} = \frac{1}{N}\sum_{j=0}^{N-1} f_{ij}e_{j,t-1}, \quad t > 1, \tag{3.27}$$

where $f_{ij} = f_i(\xi_j)$ are the influence functions corresponding to each constraint M'_j. We choose the influence functions to be the NURBS basis functions which are used to describe the curve, i.e. $f_i(\xi) = R_i(\xi)$. The parameter coordinate ξ_j of each M_j should satisfy $\xi_j \in [\xi_i, \xi_{i+p+1}]$. We use the Greville

Abscisse to generate the sample points to make sure the influence functions associated with each M'_j are linearly independent [146]. Finally, the error vector is calculated in a recursive way:

$$e_{j,t} = e_{j,t-1} - \frac{1}{N}\sum_{k=0}^{N-1}\sum_{i=0}^{n-1} R_{ij} f_{ik} e_{k,t-1}, \tag{3.28}$$

where $R_{ij} = R_i(\xi_j)$. The details for updating the crack front is given in Algorithm (1). Once the new crack front curve is obtained, the new crack surfaces can be generated by lofting along the crack extension direction from the old curve to the new curve. The generated crack surfaces can be merged into the old crack surfaces with either a C^0 joint or a C^1 joint. In this work a C^0 merging is adopted.

Algorithm 1 Crack front updating algorithm

Data: old crack front curve $\mathbb{C}(\xi)$; sample points M_j; new positions of sample points M'_j
Result: new crack front curve that passes through all M'_j
$t = 0$;
$tol = 1.e-4$;
$e_{j,0} = \overrightarrow{M_{j,0}M'_j}$; //the initial error vector
while $\|\mathbf{e}_t\| > tol$ **do**
  $t = t + 1$;
  $m_{i,t} = \frac{1}{N}\sum_{j=0}^{N-1} f_{ij} e_{j,t-1}$; //the motion vector at t-th step
  $P_{i,t} = P_{i,t-1} + m_{i,t}$; //the new point on the crack front at t-th step
  $e_{j,t} = e_{j,t-1} - \frac{1}{N}\sum_{k=0}^{N-1}\sum_{i=0}^{n-1} R_{ij} f_{ik} e_{k,t-1}$; //the error vector at t-th step
end

3.5 Numerical examples

In this section, numerical examples are treated to verify the methodology. We first verify the 3D IGABEM for fracture by investigating the convergence of the COD and SIFs with mesh refinement using both the VCCI and M integral, for curved crack fronts. We then verify the propagation algorithm against the literature. We study the integration algorithm in detail for the case of the penny-shaped crack. The Young's modulus $E = 1000$ and Poisson's ratio $\nu = 0.3$ for all cases. The relative error in the L_2 norm of

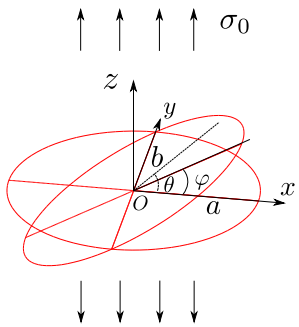

FIGURE 3.4: Geometry for penny-shaped crack ($a = b$) and elliptical crack ($a \neq b$)

COD is computed as

$$e_{L_2} = \sqrt{\frac{\int_S (\llbracket \mathbf{u} \rrbracket - \llbracket \mathbf{u} \rrbracket_{\text{ext}})(\llbracket \mathbf{u} \rrbracket - \llbracket \mathbf{u} \rrbracket_{\text{ext}})^{\mathrm{T}} \mathrm{d}S}{\int_S \llbracket \mathbf{u} \rrbracket_{\text{ext}} \llbracket \mathbf{u} \rrbracket_{\text{ext}}^{\mathrm{T}} \mathrm{d}S}}, \tag{3.29}$$

where the subscript 'ext' denotes the analytical solution of COD.

3.5.1 Penny-shaped crack

Suppose a penny-shaped crack is subjected to the remote tension σ_0, i.e. $\mathbf{t}^{\infty} = (0, 0, \sigma_0)$. The radius of circle is a. The inclination angle is φ and circular angle θ is defined in the crack plane (Oxy) as in Figure 3.4. The analytical solution for the SIFs read [163]:

$$\begin{aligned} K_I(\varphi) &= \frac{2}{\pi}\sigma_0\sqrt{a\pi}\cos^2\varphi, \\ K_{II}(\varphi,\theta) &= \frac{4}{\pi(2-\nu)}\sigma_0\sqrt{a\pi}\cos\varphi\sin\varphi\cos\theta, \\ K_{III}(\varphi,\theta) &= \frac{4(1-\nu)}{\pi(2-\nu)}\sigma_0\sqrt{a\pi}\cos\varphi\sin\varphi\sin\theta. \end{aligned} \tag{3.30}$$

In particular, when the crack plane is horizontal ($\varphi = 0$), the analytical normal displacement is given as:

$$u_z(r,\theta,0) = \frac{2(1-\nu)\sigma_0}{\pi\mu}\sqrt{a^2 - r^2}, \quad r \leqslant a. \tag{3.31}$$

Singular integration test

The problem is modeled by COD equation (2.13), so that a single NURBS patch is necessary to represent the crack. The numerical COD is compared

to the analytical solution. The collocation points are moved aside from the pole in order not to locate at the degenerated point. The NURBS basis functions associated with the pole, however, are enforced to be C^0 through sharing the same degrees of freedom. The BIEs from these moved collocation points are merged into one equation.

We note that the COD solution only varies in the radial direction and is constant in the angular direction, thus 4 elements are used in the angular direction. This will lead to high aspect ratio of each element with the refinement in the radial direction. Figure 3.5 compares the L_2 norm error in COD for $\varphi = 0$. 'ngp_s' denotes the number of Gauß points in the angular direction in each sub-triangle. By 'original SST', we mean a direct use of the method and by 'improved SST', the SST with conformal and Sigmoidal transformation. It can be observed that

- when $ngp\_s = 30$, the errors of the original SST and improved SST are comparable. However, the error from the original SST is non-uniformly distributed whilst the improved SST provides a more uniform error distribution;
- when $ngp\_s = 18$, the error from the original SST increases significantly (e_{L_2} =1.467716e-1), while the improved SST maintains the same accuracy as for $ngp\_s = 30$;
- the error is larger near the crack front. This is due to the crack tip singularity.

We conclude that the original SST requires more Gauß points for the same accuracy level as the improved SST. If we move the knot ($\eta = 0.875$) next to the crack front in the radial direction closer to the crack front ($\eta = 0.94$) and repeat the comparison of Figure 3.6, we find that even for $ngp\_s = 30$, the original SST still gives error as large as for $ngp\_s = 18$. while the improved method gives an error of e_{L_2} =1.755681e-2, which is lower than what was shown in Figure 3.5. We can refer that, due to the crack tip singularity, a refined mesh near the crack front should give a better accuracy in COD, but

the original SST is sensitive to the element distortion and gives diverged results. The improved SST presents a robust application for this kind of mesh configuration.

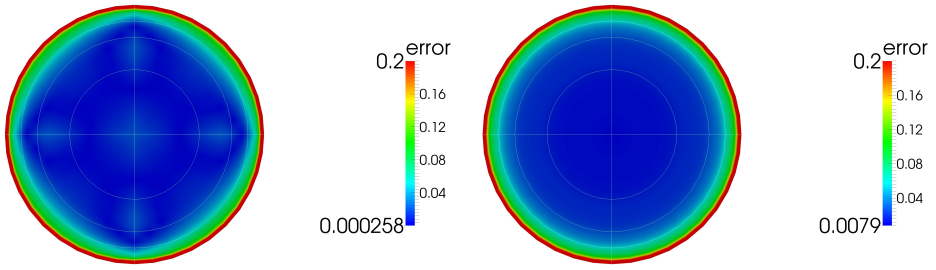

(a) original SST, ngp_s=30, e_{L_2} =3.344418e-2

(b) improved SST, ngp_s=30, e_{L_2} =3.844282e-2

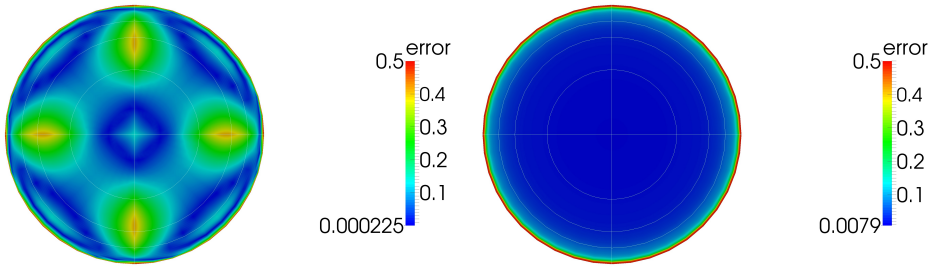

(c) original SST, ngp_s=18, e_{L_2} =1.467716e-1

(d) improved SST, ngp_s=18, e_{L_2}=3.844282e-2

FIGURE 3.5: The relative error of COD for the penny crack problem. 'ngp_s' denotes the number of Gauß points in angular direction in each sub-triangle. Knot vectors: angular direction $\boldsymbol{\xi}$=[0,0,0,0.25,0.25,0.5,0.5,0.75,0.75,1,1,1], radial direction $\boldsymbol{\eta}$=[0,0,0,0.5,0.75,0.875,1,1,1]

Convergence test

We perform uniform mesh refinement in parametric space. We calculate the element size as $h = \sqrt{S_e^{\max}}$, where $S_e^{\max}$ denotes the maximum area of the elements. The convergence curve is plotted in Figure 3.8 where we compared both the quadratic and cubic NURBS basis functions. It can be concluded that degree elevation improves accuracy. Yet, the order of convergence rate (ocr) of the relative error in the L_2 norm of COD keeps almost the same value ($ocr = 1$). The deteriorated ocr is due to the physical singularity along the crack front.

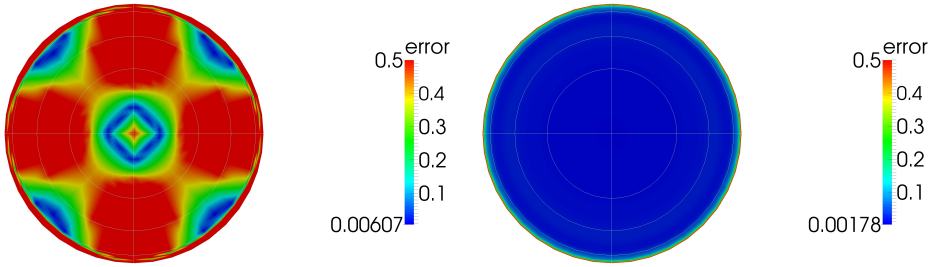

(a) original SST, ngp_s=30, e_{L_2}=8.138911e-1 (b) improved SST, ngp_s=30, e_{L_2}=1.755681e-2

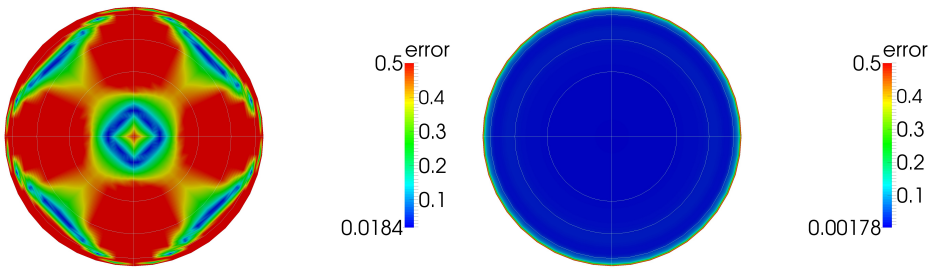

(c) original SST, ngp_s=18, e_{L_2}=7.110011e-1 (d) improved SST, ngp_s=18, e_{L_2}=1.755679e-002

FIGURE 3.6: The relative error of COD for the penny crack problem. 'ngp_s' denotes the number of Gauß points in angular direction in each sub-triangle. Knot vectors: angular direction $\boldsymbol{\xi}$=[0,0,0,0.25,0.25,0.5,0.5,0.75,0.75,1,1,1], radial direction $\boldsymbol{\eta}$=[0,0,0,0.5,0.75,0.94,1,1,1]

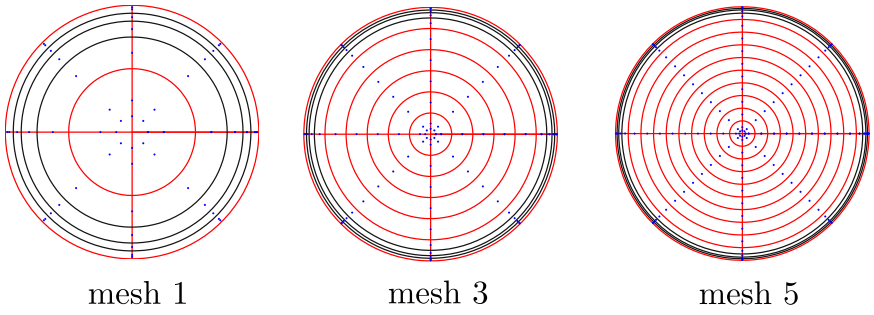

FIGURE 3.7: NURBS($p = q = 2$) represented crack surface meshes with 2, 6, and 10 uniform refinement in the radial direction, followed by graded refinement (with black edges) close to crack front. The blue dots are collocation points

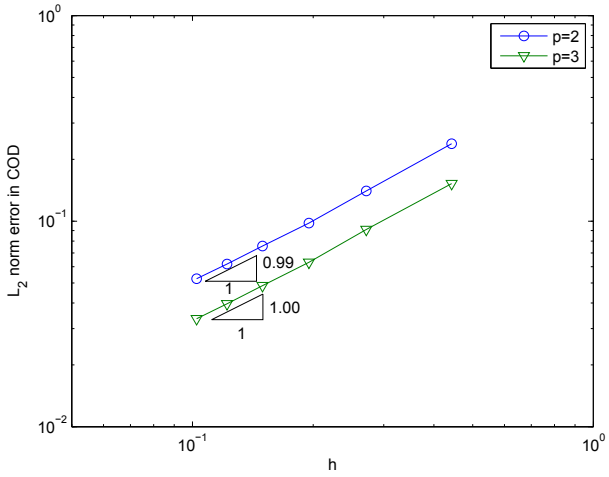

FIGURE 3.8: The relative error in the L_2 norm of COD for penny-shaped crack

As is well known, uniform refinement is neither effective nor efficient to improve the accuracy for the crack problem. Thus five mesh configurations are designed, through keeping the number of elements in the angular direction while the mesh is uniformly refined by 2, 4, 6, 8 and 10 elements in the radial direction. The elements along the crack front is then further gradely refined by consecutive knot insertion to reduce the error caused by the crack tip singularity (Figure 3.7 shows meshes 1, 3 and 5). Figure 3.9 shows for convergence study. It can be seen that the accuracy is improved almost by one order compared to uniform refinement and the final estimate convergence rate is two times higher than for uniform refinement. This indicates the effectivity of IGABEM for fracture simulation.

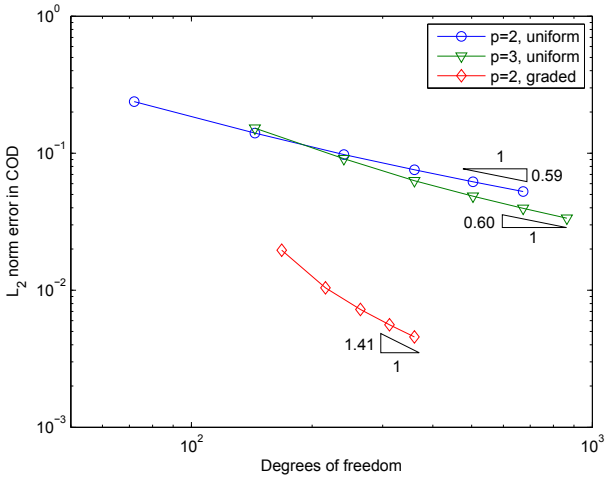

FIGURE 3.9: The relative error in the L_2 norm of COD for penny-shaped crack

Stress intensity factor test

In this subsection, the computation of SIFs is verified. Instead of using the COD equation to model the penny-shaped crack in an infinite domain, we embed two overlapping crack surfaces in a cube with size $L = 200a$ such that we can compare the numerical SIFs with the analytical solution for infinite domain. Dual equations are used for this case.

Figure 3.10 shows the path independence of the M integral and VCCI for mode I penny-shaped crack. Here 'R' denotes the virtual crack advance in VCCI and the radius of the contour in M integral. It can be seen that when R/a is from 0.02 to 0.08, both methods show path dependent behavior. For M integral, the error varies within 2%. When the radius of contour is small, K_I converges to analytical value; while increasing R, since the stress field for the crack tip is influence by other tips in the crack front, plane strain condition is not satisfied properly, the method becomes inaccurate. For VCCI, the error varies within 6% and generally a small virtual crack advance is needed. However, if R is too small, difficulty in numerical evaluation of stress and COD close to crack front will arise which lead to the inaccuracy of K_I. From the figure we can also refer that M integral presents a smaller reduction in error than VCCI.

Figure 3.11 compares the SIFs obtained from M integral with $R = 0.02a$

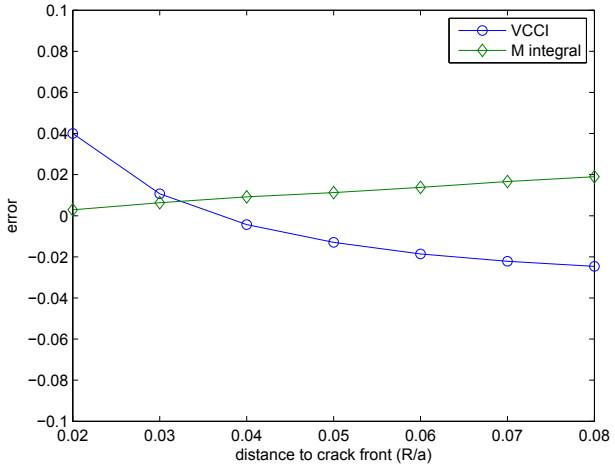

FIGURE 3.10: Path independence verification for VCCI and M integral. Here 'R' denotes the virtual crack advance in VCCI and the radius of the contour in M integral

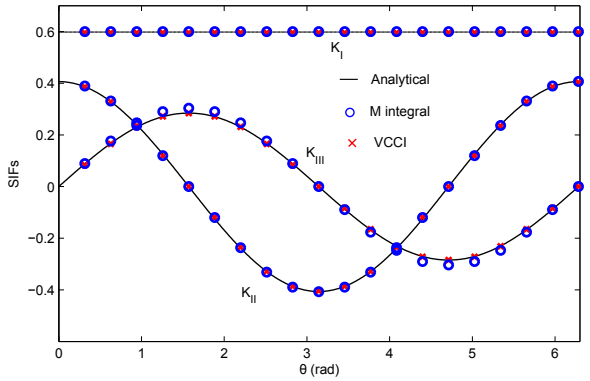

FIGURE 3.11: Stress intensity factors for penny crack with $\varphi = \pi/6$

and VCCI with $R = 0.04a$ for the mixed mode penny-shaped crack with inclination angle $\varphi = \pi/6$. It is seen that both methods agree well with the analytical solution. K_{III} from M integral shows deviation near $\theta = \pi/2$ and $3\pi/2$. Table 3.1 presents the error at $\theta = 0$, $\pi/4$ and $\pi/2$. It can be observed that the error of K_I and K_{II} is within 1% by both methods, while within 7% for K_{III} by M integral. we can conclude that the IGABEM can provide accurate SIFs, and the numerical SIFs along crack front is quite smooth, although with only 4 elements in angular direction and without any smoothness operation. This gives the premise for a stable evolution for the crack growth simulation.

3.5.2 Elliptical crack

Suppose an elliptical crack is subjected to the remote tensile loading σ_0 in the normal direction, i.e. $\mathbf{t}^\infty = (0, 0, \sigma_0)$. The semi-major axis is a, semi-minor axis b. The inclination angle is φ and the elliptical angle θ is defined in the crack plane as in Figure 3.4. The analytical SIFs read [163]:

$$\begin{aligned} K_I(\varphi,\theta) &= \frac{\sigma_0}{2}(1+\cos 2\varphi)\frac{\sqrt{b\pi}f(\theta)}{E(k)}, \\ K_{II}(\varphi,\theta) &= \frac{\sigma_0}{2}\sin 2\varphi\frac{\sqrt{b\pi}k^2(b/a)\cos\theta}{f(\theta)B(k)}, \\ K_{III}(\varphi,\theta) &= \frac{\sigma_0}{2}\sin 2\varphi\frac{\sqrt{b\pi}k^2(1-\nu)\sin\theta}{f(\theta)B(k)}, \\ k^2 &= 1-\frac{b^2}{a^2}, \\ f(\theta) &= (\sin^2\theta+\frac{b^2}{a^2}\cos^2\theta)^{1/4}, \\ B(k) &= (k^2-\nu)E(k)+\nu\frac{b^2}{a^2}K(k), \end{aligned} \tag{3.32}$$

where $K(k)$ and $E(k)$ are elliptic integrals of the first kind and second kind, respectively:

$$\begin{aligned} K(k) &= \int_0^{\pi/2}\frac{1}{\sqrt{1-k^2\sin^2\theta}}\mathrm{d}\theta, \\ E(k) &= \int_0^{\pi/2}\sqrt{1-k^2\sin^2\theta}\mathrm{d}\theta. \end{aligned} \tag{3.33}$$

In particular, when $\varphi = 0$, the displacement in the normal direction to the crack reads:

$$u_z(x,y,0) = \frac{2(1-\nu)\sigma_0}{\mu}\frac{b}{E(k)}\sqrt{1-\frac{x^2}{a^2}-\frac{y^2}{b^2}}. \tag{3.34}$$

The difference of the elliptical crack and penny crack is that the mode I SIF is not a constant, due to the variation of the curvature along the crack

	K_{II}		K_{III}	
	VCCI	M	VCCI	M
$\theta = 0$	7.133e-3	2.008e-3	2.898e-8	5.221e-9
$\theta = \pi/4$	7.167e-3	1.983e-3	1.591e-4	6.243e-2
$\theta = \pi/2$	1.622e-8	1.228e-8	2.010e-4	1.894e-2

TABLE 3.1: Error of SIFs for penny-shaped crack with $\varphi = \pi/6$.

front. The problem is modeled by COD equation (2.13) and mesh configuration and collocation strategy is analogous to the case of the penny-shaped crack. For elliptical cracks, the elements have high aspect ratios as well as non-orthogonal basis vectors. Figure 3.12 shows that original SST presents erroneous result with 18 Gauß points in angular direction. While the improved SST gives a reasonable COD and error distribution.

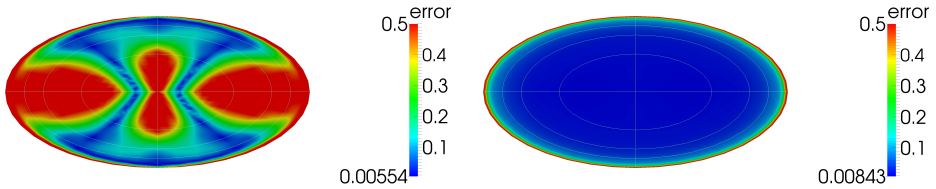

(a) original SST, ngp_s=18, e_{L_2}=4.603473e-1 (b) improved SST, ngp_s=18, e_{L_2}=3.798002e-2

FIGURE 3.12: Relative error in COD for elliptical crack. Knot vectors: angular direction $\boldsymbol{\xi}$=[0,0,0,0.25,0.25,0.5,0.5,0.75,0.75,1,1,1], radial direction $\boldsymbol{\eta}$=[0,0,0,0.5,0.75,0.875,1,1,1]

For the convergence study, we first give the result of uniform refinement in parametric space in Figure 3.14. Then the same graded mesh configurations for elliptical crack are generated as done for penny crack as in Figure 3.13. Figure 3.15 compares the result between uniform mesh and graded mesh. The convergence feature is almost the same as that of penny crack. And we can conclude that the IGABEM also suits well for modeling elliptical crack.

For the test of SIFs computation, we put two overlapping crack surfaces in a cube with size $L = 200a$ such that we could compare the numerical SIFs with the analytical solution for infinite domain. Dual equations are used.

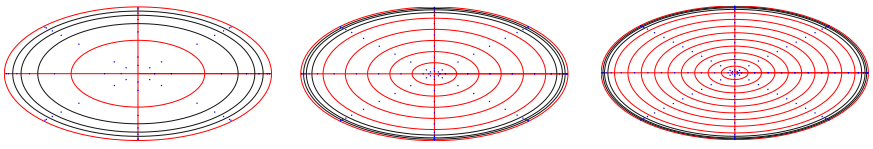

mesh 1 mesh 3 mesh 5

FIGURE 3.13: The NURBS ($p = q = 2$) represented crack surface meshes with 1, 5, and 9 uniformed refinement in radial direction, followed by graded refined elements (with black edges) close to crack front. The blue dots are collocation points

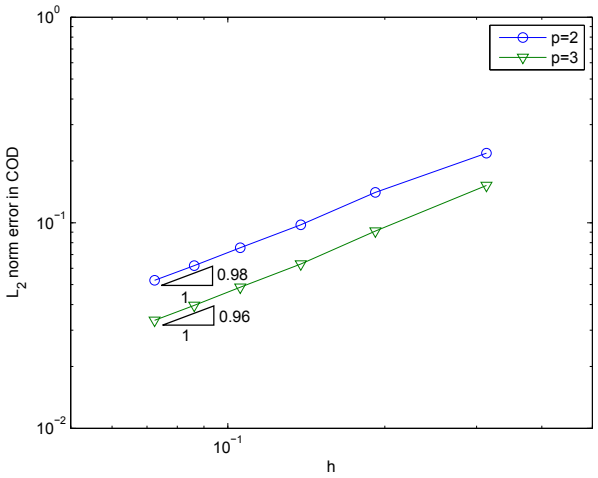

FIGURE 3.14: L_2 norm error of COD for elliptical crack

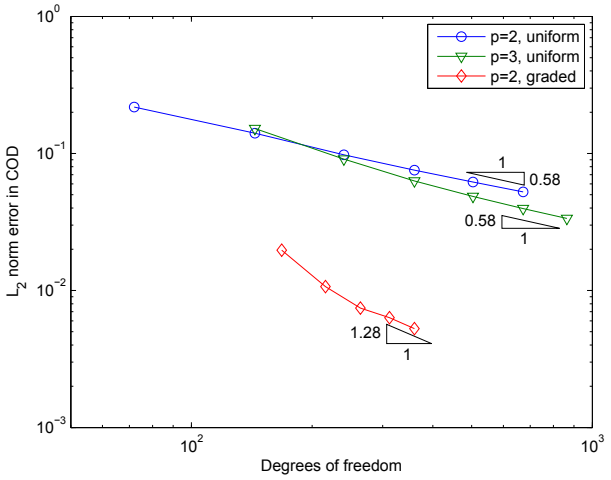

FIGURE 3.15: L_2 norm error of COD for elliptical crack

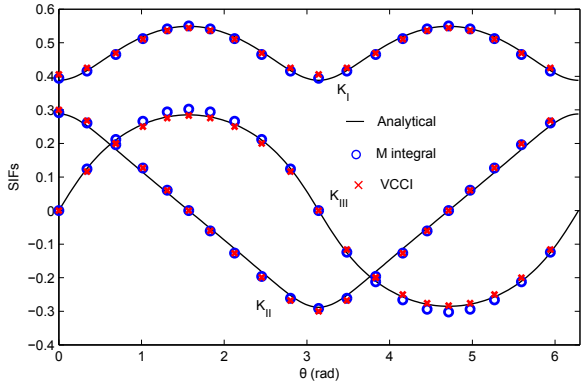

FIGURE 3.16: Stress intensity factors for elliptical crack with $\varphi = \pi/6$

Figure 3.16 compares the SIFs obtained from M integral with $R = 0.02b$ and VCCI with $R = 0.02b$ for the mixed mode elliptical crack with inclination angle $\varphi = \pi/6$. Table 3.2 presents the error at $\theta = 0$ and $\pi/2$ for the SIF in three modes. It can be seen that the error for all the SIFs is within 7%. And the SIFs along the crack front is smooth. We note that the SIFs accuracy for the elliptical crack is worse than for the penny crack, which is due to the variation of the crack curvature along the crack front. Since a fixed value of R is used, the singularity at the sample points near the semi-major and semi-minor axes would be different, which leads to inaccuracies in the SIFs evaluation [164]. More suitable way to estimate the SIFs for elliptical crack would be one of the future work.

	K_I		K_{II}		K_{III}	
	VCCI	M	VCCI	M	VCCI	M
$\theta = 0$	4.564e-2	1.534e-2	4.138e-2	1.279e-2	1.226e-7	2.174e-7
$\theta = \pi/2$	8.284e-3	2.214e-2	6.936e-8	5.152e-8	6.882e-3	5.959e-2

TABLE 3.2: Relative error of SIFs for elliptical crack with $\varphi = \pi/6$

3.5.3 Fatigue crack growth

In this section, the crack surface updating algorithm is tested using the Paris law as a crack growth law. We first check the crack growth of the horizontal penny crack under uniform tension from section 3.5.1. The fatigue parameters $m = 2.1$ and the specified $\Delta a_{\max} = 0.2a$. Since the defined

problem gives a uniform velocity along the crack front, exact crack fronts can be obtained for each step of growth and can be used to benchmark numerical ones. We propagate 10 steps and compare the exact crack front with the IGABEM result(Figure 3.17(a)). A numerical result obtained by the XFEM+level set method is also compared to the exact one in [165] (Figure 3.17(b)). It can be observed that the numerical crack fronts by IGABEM agree well with exact ones. While the crack front by XFEM+level set deviates gradually from the exact crack fronts, due to the fact that the level set method is restricted in describing the crack front exactly and this inaccuracy accumulates at each step. We then compute the crack propagation for $m = 5$, and the result is presented in Figure 3.17 (c). We find that the numerical crack front still agrees well with the exact front, although the high index amplifies the error in crack growth rate. In order to quantitatively scale the error, we define the relative error of the numerical crack front to the exact front as:

$$\begin{aligned} E_f(\mathbf{x}) &= \frac{|\Gamma_{\text{num}}(\mathbf{x}) - \Gamma_{\text{ext}}(\mathbf{x})|}{\Delta a}, \\ \text{error} &= \frac{\int_\Gamma E_f(\mathbf{x}) \mathrm{d}\Gamma_{\text{ext}}(\mathbf{x})}{\int_\Gamma \mathrm{d}\Gamma_{\text{ext}}(\mathbf{x})}, \end{aligned} \tag{3.35}$$

where Γ_{num} denotes the geometry of numerical crack front and Γ_{ext} is the exact one.

Figure 3.18 gives the relative error of the numerical crack front by IGABEM. It can be seen that the error accumulates in a slow speed and the difference of $m = 5$ and $m = 2.1$ is small, although the error for $m = 5$ is larger than $m = 2.1$ as expected. This test shows the proposed crack propagation scheme has the ability to grow cracks in a stable and accurate manner, thanks to the smoothness in the stress field and SIFs solution and to the exact representation of the geometry of the crack during the crack growth.

Finally, we simulate crack growth for an elliptical crack with inclination angle $\varphi = \pi/6$ modeled by the dual equations in a finite domain taken from section 3.5.2. Figure 3.19 illustrates the 2nd, 5th and 10th of the propagation step.

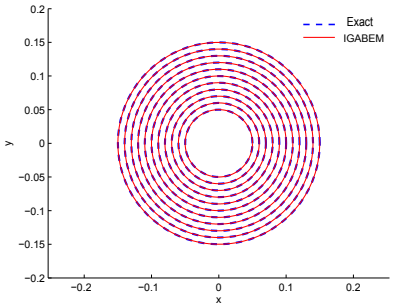

(a) IGABEM, $m = 2.1$

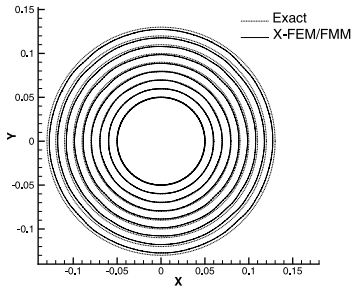

(b) XFEM/FMM, $m = 2.1$, Sukumar *et al* 2003

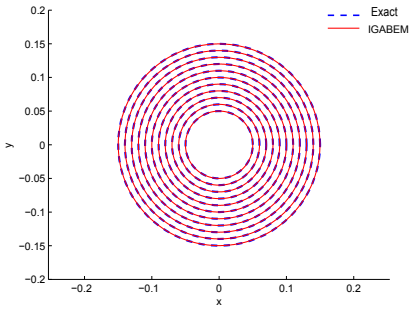

(c) IGABEM, $m = 5$

FIGURE 3.17: Fatigue crack growth of the first 10 steps of a penny crack

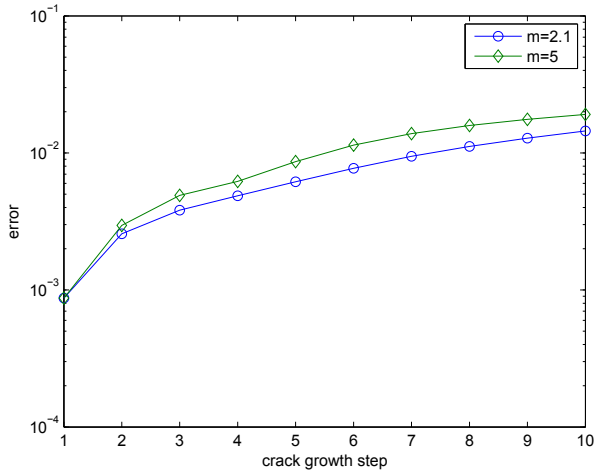

FIGURE 3.18: Relative error of the crack front for in each crack growth step by IGABEM

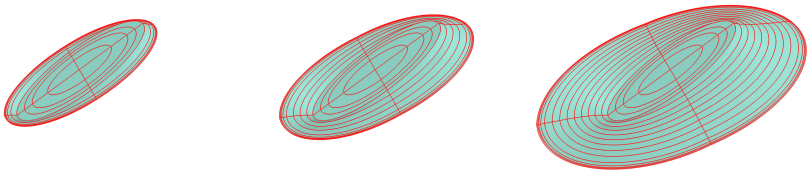

(a) Step 2 (b) Step 5 (c) Step 10

FIGURE 3.19: Fatigue crack growth simulation of an elliptical crack

3.6 Conclusions

The formulation and implementation of isogeometric boundary element methods (IGABEM) for simulating 3D fatigue fracture problem were outlined in this chapter. The same NURBS basis functions have been used for the discretization of the geometry and crack and for the approximation of displacement/traction. The singularity subtraction technique (SST) proposed in [128] has been used for the treatment of (hyper-)singular integrals in BEM. The improved SST [154] has been extended to quadrilateral elements such that it can be applied to tensor-product NURBS basis functions. Both the COD form and dual equations of IGABEM have been used to model the crack. Two methods to extract SIFs, the contour-based M integral and VCCI, were compared. An algorithm to propagate the NURBS-represented crack surface was presented and validated. The highlights of this work include:

(1) The proposed singular integration scheme can preserve the quadrature accuracy for highly distorted elements which exist commonly in IGA. Thus it enables a robust IGABEM implementation;

(2) Through graded mesh refinement in the direction where the crack tip singularity varies, the convergence rate can be improved by a factor of 2 and the accuracy can be improved by one order, compared to uniform refinement. This shows the promise of IGABEM for fracture problem;

(3) The local crack tip system is setup naturally and uniquely thanks to the NURBS representation of the crack surface. Combining with the continuity in stress solution in BEM, the obtained SIFs along the crack front are smooth

and accurate;

(4) The proposed algorithm for crack propagation is seen to be stable, even for high exponent values in the Paris law, due to the smoothness in the crack front geometry and numerical SIFs.

The use of CAD geometry directly for fracture simulation provides benefits as listed above. Nevertheless it also raises difficulties to model surface cracks, where the crack will intersects the boundary of the body indeed, introducing and evolving the discontinuity into a NURBS patch at an arbitrary position is cumbersome due to the higher order continuity of the basis functions. The next chapter will provide a solution to model the surface cracks problem, based on the development of a trimmed NURBS approach.

Chapter 4

IGABEM for trimmed NURBS and surface crack modeling

This chapter presents some numerical aspects of isogeometric boundary element methods (IGABEM). The behavior of hyper-singular and nearly-singular integration is first explored on the distorted NURBS surface and several numerical treatments are proposed to enhance the quadrature in the framework of isogeometric analysis. Then a numerical implementation of IGABEM for trimmed NURBS is detailed. Based on this idea, the surface crack problem is modeled with the phantom element method. And the crack is allowed to intersect with the boundary of the body while preserving the original parametrization of the NURBS-based CAD geometry.

4.1 Trimmed NURBS surfaces

The geometry is generally created via trimming operations performed on NURBS surfaces. The data of the NURBS surface and the relative trimming information is stored in an IGES file. The trimming curve is given both in physical space and parametric space. Figure 4.1 illustrates a trimmed surface

$$S(\xi,\eta)=\sum_{i=1}^{n}\sum_{j=1}^{m}R_{i,j}(\xi,\eta)P_{i,j}, \tag{4.1}$$

with the physical trimming curve

$$C(s)=\sum_{k=1}^{l}R_k(s)Q_k, \tag{4.2}$$

and the parametric trimming curve

$$C^p(u) = \sum_{k=1}^{l^p} R_k^p(u) Q_k^p, \tag{4.3}$$

where $R_{i,j}$,R_k, R_k^p and $P_{i,j}$, Q_k, Q_k^p are the NURBS basis functions and control points of the surface, physical trimming curve and parametric trimming curve respectively. Supposing the parametric domain of $S(\xi, \eta)$ is a rectangle defined by $D = \{(\xi, \eta) | \xi_1 \leq \xi \leq \xi_2 \text{ and } \eta_1 \leq \eta \leq \eta_2\}$, the parametric trimming curve $C^p(u)$ will take its values inside the domain.

Note that the $C(s)$ and $C^p(u)$ are independent curves, i.e, the number of basis functions and their degrees can be different. In the IGES manual [166], the trimming curve can be given by the composition of mapping $S(\xi, \eta)$ and $C^p(u)$, i.e., the composition curve

$$\begin{aligned} C_c(u) &= S \circ C^p(u) = S(C^p(u)) = S(\xi(u), \eta(u)) \\ &= (x(\xi(u), \eta(u)), y(\xi(u), \eta(u)), z(\xi(u), \eta(u))). \end{aligned} \tag{4.4}$$

The resulting physical trimming curve $C_c(u)$ and $C(s)$ which is provided in IGES file, will share the same image and orientation in physical space.

4.1.1 Representation of trimmed surface

In order to obtain analysis-suitable trimmed surfaces, the trimmed elements need to be determined, which requires a search through the surface parametrization to compute the parametric coordinates of the intersection points of the trimming curve with the trimmed surface. Here the trimmed elements means the 2D tensor-product knot spans (quadrilateral elements) with some edges intersected with the parametric trimming curve. The bisection searching algorithm by Schmidt *et al* [167] is adopted in this work. After identification of the intersection points, the trimmed elements can be picked out and categorized into three categories: triangle ('3'), quadrangle ('4') and pentagon ('5') as in Figure 4.1(b). Other types of cutting can be transformed into the named types by knot insertion (mesh refinement). Note that the

trimming orientation (Figure 4.1(b)) will determine which side of the surface is remained. In the present work, the left hand side of the direction of the trimming curve[1] will be preserved.

Then the untrimmed elements will be either cropped ('-1') or kept ('1') via the following procedure:

(1) Linearize the parametric trimming curve and find the shortest distance vector $\mathbf{d}$ from the central point of the element of interest to the line-segment represented trimming curve (Figure 4.1(b));

(2) Take the cross product of the distance vector $\mathbf{d}$ and trimming orientation vector $\mathbf{t}$:

$$\mathbf{n} = \frac{\mathbf{d} \times \mathbf{t}}{|\mathbf{d} \times \mathbf{t}|}; \tag{4.5}$$

if $\mathbf{n} = (0, 0, 1)$, the element of interest will be kept, otherwise deleted.

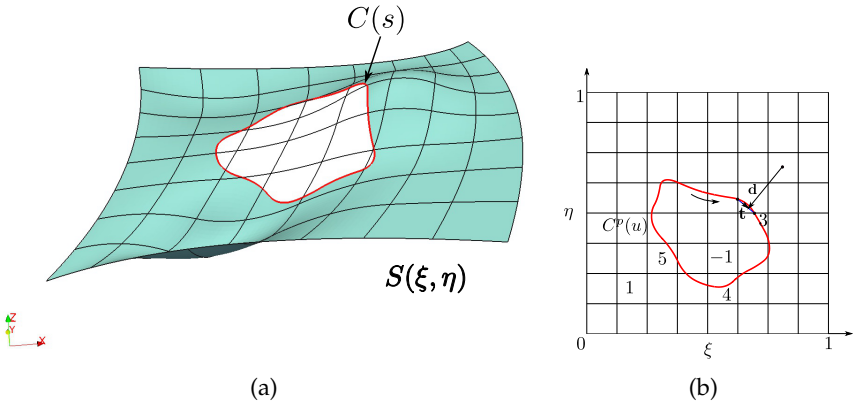

FIGURE 4.1: An example of trimmed surface, (a) in physical space; (b) in parametric space. The arrow in (b) denotes the direction of the trimming curve. The trimmed elements can be classified into three types: '3' denotes a triange, '4' denotes a quadrangle and '5' denotes a pentagon. '1' represents untrimmed elements and '-1' the cropped elements

4.1.2 Integration of trimmed elements

Numerical integration for trimmed elements is one of the key ingredients in IGA for trimmed CAD geometry. In the work by Kim *et al* [168][169], the method which was applied in NURBS-Ehanced FEM [170] was adopted.

[1]The direction (orientation) of the trimming curve is determined by the knots. The non-decreasing knot sequence is defined as the positive direction

This method requires the triangulation of the parametric domain of the trimmed element. Schmidt *et al* [167] reconstructed the trimmed element by using a new patch via interpolation or least square approximation. Beer *et al* [121] created a mapping from the area bordered by two trimming curves and straight lines which connect the ends of the trimming curves to the trimmed surfaces, by use of the composition of trimming curve given in Equation 4.4. The implementation is simple but excludes the case of holes cutout where closed trimming curves exist.

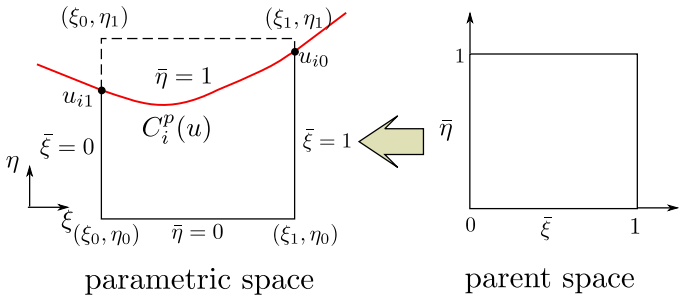

FIGURE 4.2: The mapping from parent space to parametric space. $\bar{\eta} = 0$ refers to curve I and $\bar{\eta} = 1$ is curve II

A trimmed surface analysis is proposed which can address the closed trimming curve in this work. Inspired by the work of Beer *et al* [121], this mapping approach is applied locally for the trimmed elements. First, the segmentation is done at every intersection point by knot insertion until C^0 continuity is obtained. As presented in Figure 4.2, the i-th segment of the parametric trimming curve $C_i^p(u)$ is then obtained between the intersection points u_{i0} and u_{i1}. Then the parameter range for sub-curve $C_i^p(u) = C_i^p(\tilde{u})$ is simply linearly-scaled to the range $0 \leq \tilde{u} \leq 1$.

Now we are at the stage to establish the mapping from parent space to parametric space. For the case in Figure 4.2, the $C_i^p(\tilde{u})$ would be $\bar{\eta} = 1$ (curve II), and the opposite edge $\bar{\eta} = 0$ (curve I) is a straight line. Taking

$\tilde{u} = \bar{\xi}$, using Equation (4.12), we have

$$\begin{aligned} \xi^I &= \sum_{j=1}^{n_I} R_j^I(\bar{\xi})\xi_j^I, \\ \eta^I &= \sum_{j=1}^{n_I} R_j^I(\bar{\xi})\eta_j^I, \\ \xi^{II} &= \sum_{j=1}^{n_{II}} R_j^{II}(\bar{\xi})\xi_j^{II}, \\ \eta^{II} &= \sum_{j=1}^{n_{II}} R_j^{II}(\bar{\xi})\eta_j^{II}, \end{aligned} \tag{4.6}$$

where ξ_j and η_j are the components of the parametric control points Q_j^u. Which can be obtained directly from the IGES file. Then linear interpolation is used between the two curves:

$$\begin{aligned} \xi &= (1-\bar{\eta})\xi^I + \bar{\eta}\xi^{II}, \\ \eta &= (1-\bar{\eta})\eta^I + \bar{\eta}\eta^{II}. \end{aligned} \tag{4.7}$$

And the Jacobian transformation matrix from parent space to parametric space would be

$$\mathbf{J}|_{\bar{\boldsymbol{\xi}}\to\boldsymbol{\xi}} = \begin{bmatrix} \frac{\partial\xi}{\partial\bar{\xi}} & \frac{\partial\xi}{\partial\bar{\eta}} \\ \frac{\partial\eta}{\partial\bar{\xi}} & \frac{\partial\eta}{\partial\bar{\eta}} \end{bmatrix} = \begin{bmatrix} (1-\bar{\eta})\frac{\partial\xi^I}{\partial\bar{\xi}} + \bar{\eta}\frac{\partial\xi^{II}}{\partial\bar{\xi}} & -\xi^I + \xi^{II} \\ (1-\bar{\eta})\frac{\partial\eta^I}{\partial\bar{\xi}} + \bar{\eta}\frac{\partial\eta^{II}}{\partial\bar{\xi}} & -\eta^I + \eta^{II} \end{bmatrix}, \tag{4.8}$$

where ξ^I, ξ^{II}, η^I and η^{II} and their derivatives are obtained from Equation (4.6).

Note that for the pentagon-type trimmed elements, the parametric domain will be subdivided into two sub-quadrilaterals. Then the mapping scheme is setup for each sub-quadrilateral.

Compared to the work by Beer *et al* [121], the proposed scheme for the trimmed NURBS can handle the closed trimming without further subdivision of the original patch. Integration for the trimmed NURBS is simplified and no triangulation on the parametric domain is needed as was discussed by Kim *et al* [168]. This would facilitate the implementation of singular integration for the trimmed elements.

We note that in some scenarios, where the shape or parametrization of the trimmed CAD geometry in analysis can be changed (for example the crack propagation problem, where the crack advance increment is usually computed in physical space by fracture law), only the information of physical trimming curve is updated during the analysis while the parametric trimming curve data, i.e. the parametric control points Q_j^u will be lost. A possible solution for this is to reconstruct the parametric trimming curve (recovering the control points of the parametric trimming curve) according to the physical trimming curve. In this work, the parametric trimming curve is reconstructed from the same basis functions as those of the physical trimming curve. However, it is not mandatory as the basis functions and the degree of each can be different. Then the interpolation technique is adopted for recovering the parametric control points as following:
(1) Using Greville Abscissae to generate the sample points on the i-th physical trimming curve, i.e.

$$u_k^s = (u_{k+1} + \cdots + u_{k+p})/p, k = 1, ..., n, \tag{4.9}$$

where p is the order of the trimming curve and n is the number of basis functions representing the trimming curve;
(2) Find the physical coordinates of the sample points on the trimming curve

$$\mathbf{x}_k^s = \mathbf{x}(u_k^s) = \sum_{j=1}^{n} R_j(u_k^s) Q_j, \tag{4.10}$$

where Q_j are the physical control points of this segment;
(3) Using the point inversion algorithm [129] to retrieve the parametric coordinates $P_k^s = \boldsymbol{\xi}_k^s(\xi_k^s, \eta_k^s)$ of each $\mathbf{x}_k^s$;
(4) the parametric control points $Q_j^u(\xi_j, \eta_j)$ can be found by solving

$$\begin{bmatrix} R_1(u_1^s) & \cdots & R_n(u_1^s) \\ \vdots & \ddots & \vdots \\ R_1(u_n^s) & \cdots & R_n(u_n^s) \end{bmatrix} \begin{bmatrix} Q_1^u \\ \vdots \\ Q_n^u \end{bmatrix} = \begin{bmatrix} P_1^s \\ \vdots \\ P_n^s \end{bmatrix}. \tag{4.11}$$

The relation between (ξ, η) and u is achieved by the reconstructed parametric trimming curve as follows $\forall P(\xi, \eta) \in C_i^p(u)$,

$$\begin{aligned} \xi &= \sum_{j=1}^{n} R_j(u)\xi_j, \\ \eta &= \sum_{j=1}^{n} R_j(u)\eta_j, \end{aligned} \tag{4.12}$$

where ξ_j and η_j are the components of the parametric control points Q_j^u. Then the double mapping method can be applied as aforementioned. The approximation property is illustrated in Figures 4.3 and 4.4. In Figure 4.3, since the mapping from parametric space to physical space of the original surface is linear, for curve order $p = 2$, only 3 sample points (1 element of the curve) can exactly capture the trimmed geometry. In Figure 4.4, since the mapping from parametric space to physical space of the original patch is nonlinear, the trimmed surface is inaccurately approximated using 3 sample points (Figure 4.4(b)), however, using more sample points by refining the trimming curve improves the approximation as shown in Figure 4.4(c). The convergence of the approximation error $(S_{\text{trim}} - S_{\text{ext}})/S_{\text{ext}}$ (S_{trim} is the area of the trimmed surface by the proposed approximation, S_{ext} is the exact area of the trimmed surface) with respect to the number of sample points is given in Figure 4.5. It can be observed that fast convergence speed is achieved (the approximation accuracy can reach $O(10^{-8})$ with only 16 sample points) which indicates the efficiency of the proposed method to approximate the trimmed geometry.

Another benefit by using the reconstructed trimming curve probably lies in improving the numerical quadrature efficiency. When we perform the quadrature for trimmed elements, the parametric domain needs to be subdivided into sub-regions which would conform to the knot intervals of the parametric trimming curve such that Gaussian quadrature rule can be applied for each sub-region. However sometimes the parametric trimming curve provided by IGES file could include many knot intervals, resulting in more sub-regions for integration and the number of Gauß points increases.

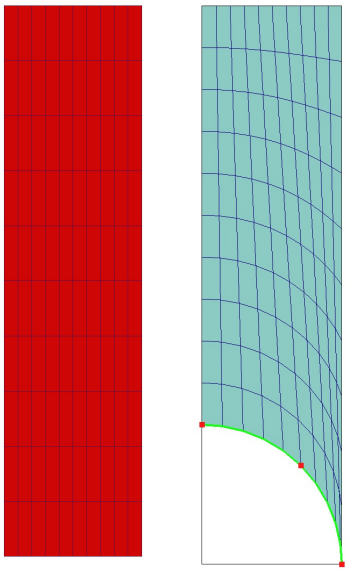

(a) (b)

FIGURE 4.3: Approximation of the trimming surface; (a) The original surface; (b) The trimmed surface, where the green line is the physical trimming curve, and the red dots are sample points. The mapping from parametric to physical space is linear, the trimmed surface is exactly represented

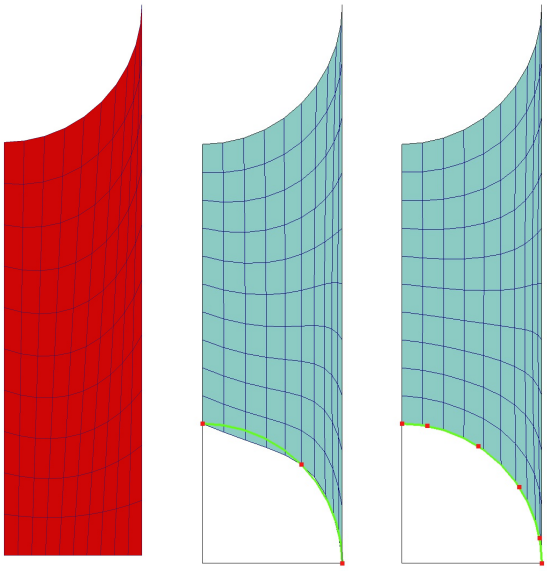

(a) (b) (c)

FIGURE 4.4: Approximation of the trimming surface; (a) The original surface; (b) The trimmed surface with 3 sample points on the trimming curve; (c) The trimmed surface with 6 sample points on the trimming curve

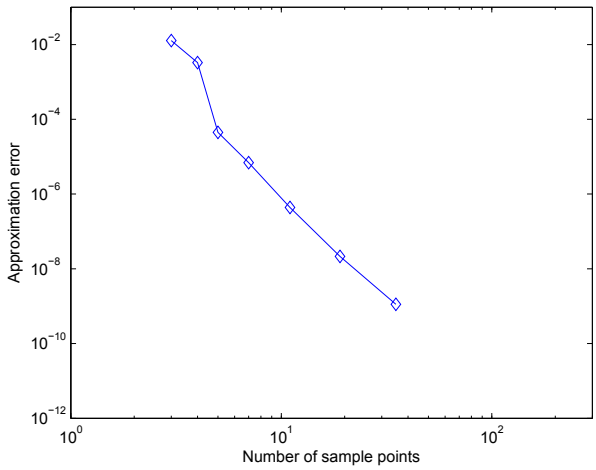

FIGURE 4.5: The convergence plot of approximation error $(S_{\text{trim}} - S_{\text{ext}})/S_{\text{ext}}$ with respect to the number of sample points

By reconstructing the parametric trimming curve, the number of knot intervals is reduced, then the effort for numerical quadrature is decreased at the sacrifice of loosing geometry exactness.

4.1.3 Collocation

For a closed domain composed of trimless and compatible NURBS patches, the Greville abscissae (GA) is proved to be elegant and suitable to locate the collocation points [142]. In our IGABEM implementation, for those collocation points which lie along sharp edges or at corners, or when discontinuous basis functions are needed, we offset the collocation points from the original positions as follows (Figure 4.7(a))

$$\begin{aligned} \xi_{s,i} &= \xi_{s,i} + \alpha(\xi_{s,i+1} - \xi_{s,i}), \quad \text{or} \\ \xi_{s,i} &= \xi_{s,i} - \alpha(\xi_{s,i} - \xi_{s,i-1}), \quad 0 < \alpha < 1. \end{aligned} \tag{4.13}$$

The GA collocation can be used for trimmed NURBS as well. One only needs to be aware that some collocation points associated with the basis functions on the cropped part of a patch should be inactivated due to the trimming operation, providing a one to one correspondence is specified between the basis functions and collocation points (see [122] for details).

Considering that in that case, some collocation points still locate outside the original patch, the parametric position of the collocation point is uncertain (it may locate on other patches with a totally different parametrization). We thus attempted a mixed collocation scheme tailored for trimmed NURBS patches based on the above modified Greville abscissae:
(1) Remove the collocation points located in the cropped elements and trimmed elements as denoted by blue dots in Figure 4.6(a);
(2) For each trimmed element, $(p+1)(q+1)$ (the number of basis functions for this element) collocation points are uniformly placed inside the elements (the yellow dots in Figure 4.6(b)).
We note that in this way the number of collocation points is more than the number of basis functions (or the number of degree of freedoms, which is identical to the number of entry of the boundary integral equations). This leads to an over-determined system equations. Hence the boundary integral equations from $(p+1)(q+1)$ collocation points in each trimmed element will be merged into the entry of equations numbered by the global index of these collocation points in each trimmed element. For the pentagon-type trimmed elements, the $(p+1)(q+1)$ collocation points are simply placed in one of the sub-quadrilaterals (more details are outlined in Section 4.4.3). However, bespoke schemes can be constructed to place the collocation points by comparing the area of the sub-quadrilaterals or by uniformly distributing them into both sub-quadrilaterals. More efficient collocation scheme are certainly an important direction for future work. Figure 4.7 compares the the GA collocation and mixed collocation methods for a square trimmed by a circle. Note that the points locating in the trimmed elements are moved to the centre of the parent space to ensure robust singular and nearly-singular integration.

4.1.4 Boundary conditions

In this work, Dirichlet or Neumann boundary conditions for each single trimless or trimmed NURBS patch are enforced by an L_2 projection. Suppose $\bar{\mathbf{u}}$ is the prescribed displacement field on a boundary patch S. The

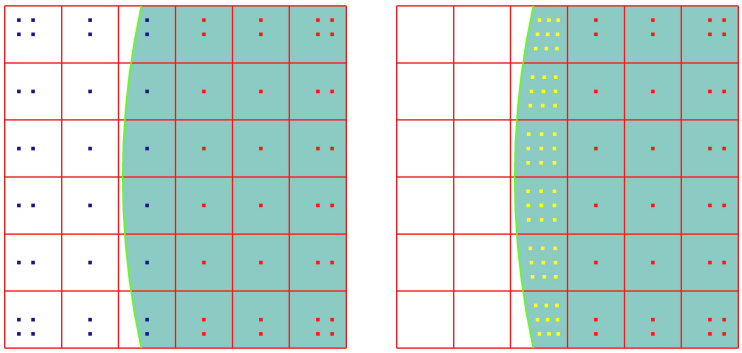

(a) (b)

FIGURE 4.6: Mixed collocation scheme for trimmed NURBS surface of order $p = q = 2$; (a) the collocation points generated by modified Greville abscissae, the blue ones are located in the cropped and trimmed elements and will be removed; (b) the final collocation points for trimmed NURBS patch by adding $(p+1)(q+1)$ collocation points in each trimmed element

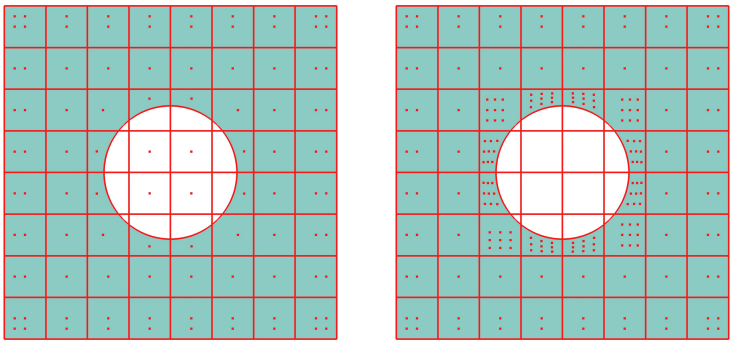

(a) (b)

FIGURE 4.7: Two collocation methods for trimmed NURBS of $p = q = 2$. (a) The Greville Abscissae (GA) collocation approach (the points located in the trimmed elements are moved to the central of the parent space); (b) The mixed collocation approach

finite element approximation $\mathbf{u}^h \in U^h$ can be found by minimizing the L_2 norm of the error between the prescribed and approximated displacement fields, i.e.

$$\begin{aligned} J(\mathbf{u}_h) &:= \|\bar{\mathbf{u}} - \mathbf{u}^h\|^2_{L_2(S)} \\ &= \int_S (\bar{\mathbf{u}} - \mathbf{u}^h)(\bar{\mathbf{u}} - \mathbf{u}^h)^{\mathrm{T}} \mathrm{d}S. \end{aligned} \tag{4.14}$$

We use $(f, g)_S$ to represent the inner product $\int_s f \cdot g \mathrm{d}S$. The minimization can be realized by letting the residual $\bar{\mathbf{u}} - \mathbf{u}^h$ be orthogonal to any arbitrary $\mathbf{v}^h \in U^h$,

$$\begin{aligned} (\bar{\mathbf{u}} - \mathbf{u}^h, \mathbf{v}^h)_S = 0, \\ (\mathbf{u}^h, \mathbf{v}^h)_S = (\bar{\mathbf{u}}, \mathbf{v}^h)_S. \end{aligned} \tag{4.15}$$

Now we use the NURBS basis functions to get the approximation

$$\mathbf{u}^h = \sum_{j=1}^{N} \mathbf{R}_j \mathbf{d}_j, \quad N \text{ is the number of basis functions.} \tag{4.16}$$

Substituting Equation (4.16) into (4.15), the discretized linear system can be obtained as

$$\mathbf{K}\mathbf{d} = \mathbf{F}, \tag{4.17}$$

where the components of $\mathbf{K}$ is $\mathbf{K}_{ij} = (\mathbf{R}_i, \mathbf{R}_j)_S$, and $\mathbf{F}_i = (\mathbf{R}_i, \bar{\mathbf{u}})_S$. Then the control coefficients $\mathbf{d}$ can be found by solving the linear system of equations.

4.2 Surface crack modeling

4.2.1 Description of the surface crack problem

In the boundary element method, cracks can be modeled by pairs of coinciding surfaces as external boundaries of the body. Then dual boundary integral equations are applied to form the linear system [42]. Figure 4.10 illustrates a surface crack (or breaking crack) model. From (a) to (b), the two coinciding surfaces (crack) are inserted into a corner of a cube, thus breaking the boundary surfaces of the cube. If we take the front surface separately as in (c), the intersection curve of the crack surfaces and the

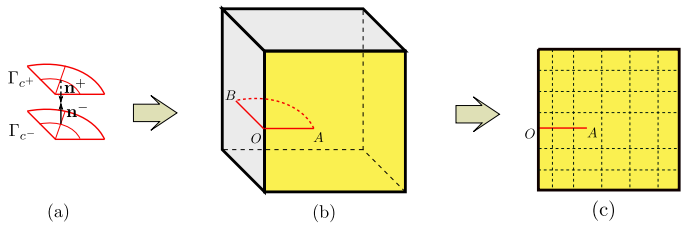

FIGURE 4.8: Surface crack model by the boundary element method. (a) The crack is modeled by two coinciding surfaces as external boundaries of the body; (b) the crack is inserted at a corner of the cube, breaking the boundary surfaces of the cube; (c) If only the front surface is concerned, the intersection curve OA of the crack and front surface will create a discontinuity on the surface

front surface OA leads to a displacement discontinuity on the front surface. Hence the surface crack problem has two manifolds in numerical implementation: one is the coinciding crack surfaces inside the body domain, the other is the surface discontinuity along the geometry boundary. The latter can be considered as a problem of cracks in 2D plane or 3D shell conditions in finite element method (FEM). In Lagrange-based elements (triangle or quadrilateral), one way to initiate and propagate the surface cracks is remeshing [43]. The extend FEM (XFEM) proposed by Belytschko and his team [5] allows the discontinuities modeled without changing the mesh discretization by introducing the enrichment functions such as the Heaviside function into the original basis functions. When the problem comes into the Isogeometric analysis, analogous treatments can be done. The work contributing on the enriched IGA to model discontinuities can be referred in, for example [97][98][99]. The original parametrization of the geometry is preserved by introducing the enrichment functions to describe the crack. Verhoosel *et al* [101] proposed a reparametrization scheme via T-Splines to explicitly represent the crack. It should be noted that in their method, the original parametrization is lost due to the reparametrization. In order to form an analysis-suitable parametrization, the elements are distorted when the crack needs to take a turn. This will deteriorate the system condition number when the crack has a sharp turn.

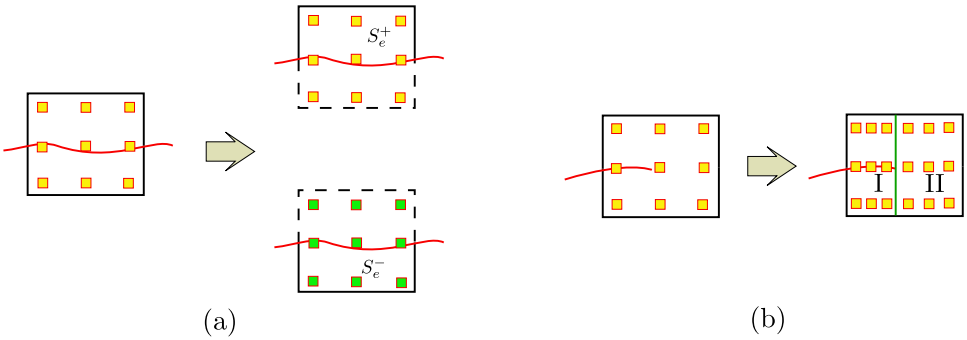

FIGURE 4.9: The phantom element method to model a surface discontinuity. The red curve denotes the crack, which is regarded as a trimming curve to split the surface. The yellow rectangle represents the degrees of freedom (DOFs) associated with the element of interest. (a) For a completely cut element, the DOFs will be doubled directly. One group is associated with the upper part of the element; an additional group with the lower part. The way of quadrature for trimmed NURBS can be applied for each part. (b) For the element containing the crack tip (an endpoint of the crack front), a knot (green line) is inserted to reduce the continuity such that the crack tip halted inside an element can be represented. In this way, the old element will be split into two new elements, and the obtained element I can then be treated with the phantom element method

4.2.2 Phantom element method

In this work, a simple approach named phantom element method (PEM, or in literature also called phantom node method [171]) is outlined to model the surface crack by IGABEM. In PEM, a crack will cut the element of interest into two parts. The degrees of freedom (DOFs) associated with this element will be duplicated, then each part has its independent DOFs to describe the primary physical fields (Figure 4.9). The PEM has been investigated in finite element-based methods to represent strong and weak discontinuities. The PEM is also a way to model discontinuities without changing the mesh, by integrating the split parts independently while no additional enrichment function is introduced. More details and applications can be seen in, for example [172][173][171][174].

Figure 4.9(a) illustrates the PEM in IGABEM to model surface cracks. The intersection curve (red curve in the figure) of the crack surfaces and the boundary surfaces can be considered as a trimming curve. By doubling the

DOFs of the cut element, a phantom element (specified as S_e^-) overlapping with the original element (S_e^+) is produced. Then the the displacement field in the cracked element is approximated as

$$\begin{aligned} \mathbf{u}^+(\mathbf{x}) &= \sum_j^{N^e} \mathbf{R}_j(\mathbf{x})\mathbf{d}_j, \quad \mathbf{x} \in S_e^+, \\ \mathbf{u}^-(\mathbf{x}) &= \sum_k^{N^e} \mathbf{R}_k(\mathbf{x})\mathbf{d}_k, \quad \mathbf{x} \in S_e^-, \end{aligned} \tag{4.18}$$

where N_e is the number of basis functions for the cracked element. For the element containing the crack tip (an endpoint of the crack front), a local knot insertion (green line in the figure) is done to cut the element into two new elements (Figure 4.9(b)). the element I is completely cut by the crack and then PEM is applied. However we note that NURBS do not allow local knot insertion due to the tensor-product nature of its basis functions. In order to do so, we first perform knot insertion on each knot of the NURBS patch until its multiplicity is equal to $p + 1$ (p is the degree of each direction). Thus the continuity between the element reduces to C^{-1} such that discontinuous NURBS basis functions (or discontinuous rational Bézier basis functions) are obtained.

Although the continuity between the untrimmed elements is lost in order to stop the crack inside an element, the original parametrization is preserved and extensions to cracks with sharp kinks or multi-cracks are straightforward. The future work will focus on performing local knot insertion to reduce the continuity only for the crack tip element by using T-Splines in which the continuity in the non-cracked area can be preserved.

4.3 Singular and nearly singular integration

The singularity subtraction technique is used for both untrimmed and trimmed elements. We briefly recall the the formula and more details can be found

in section 3.3.1. For the hyper-singular integral of the form

$$I = \neq\!\!\!\!\int_S S(\mathbf{s}, \mathbf{x}(\bar{\boldsymbol{\xi}}))R(\bar{\boldsymbol{\xi}})\bar{J}(\bar{\boldsymbol{\xi}})\mathrm{d}S, \tag{4.19}$$

where $S(\mathbf{s}, \mathbf{x}(\bar{\boldsymbol{\xi}}))$ is the hyper-singular kernel, $R(\bar{\boldsymbol{\xi}})$ is the NURBS basis function and $\bar{J}(\bar{\boldsymbol{\xi}})$ is the Jacobian of the transformation from parent space to physical space. By subtracting the Lorentz term and adding it back semi-analytically, the integral becomes

$$\begin{aligned}
I =& \int_0^{2\pi}\int_0^{\hat{\rho}(\theta)} \Big[F(\rho,\theta) - \frac{F_{-2}(\theta)}{\rho^2} - \frac{F_{-1}(\theta)}{\rho}\Big]\mathrm{d}\rho\mathrm{d}\theta + \int_0^{2\pi} I_{-1}(\theta)\ln\frac{\hat{\rho}(\theta)}{\beta(\theta)}\mathrm{d}\theta \\
&- \int_0^{2\pi} I_{-2}(\theta)\Big[\frac{\gamma(\theta)}{\beta^2(\theta)} + \frac{1}{\hat{\rho}(\theta)}\Big]\mathrm{d}\theta \\
=& \int_0^{2\pi}\int_0^{\hat{\rho}(\theta)} F(\rho,\theta)\mathrm{d}\rho\mathrm{d}\theta - \int_0^{2\pi}\int_0^{\hat{\rho}(\theta)} \frac{F_{-2}(\theta)}{\rho^2}\mathrm{d}\rho\mathrm{d}\theta - \int_0^{2\pi}\int_0^{\hat{\rho}(\theta)} \frac{F_{-1}(\theta)}{\rho}\mathrm{d}\rho\mathrm{d}\theta \\
&+ \int_0^{2\pi}\Big\{I_{-1}(\theta)\ln\frac{\hat{\rho}(\theta)}{\beta(\theta)} - I_{-2}(\theta)\Big[\frac{\gamma(\theta)}{\beta^2(\theta)} + \frac{1}{\hat{\rho}(\theta)}\Big]\Big\}\mathrm{d}\theta \\
=& I_0 - I_2 - I_1 + I_{\text{line}}
\end{aligned} \tag{4.20}$$

The curvilinear basis vectors at the source points $\mathbf{m}_i^s = \mathbf{m}_i|_{\bar{\boldsymbol{\xi}}=\bar{\boldsymbol{\xi}}_s}, (i = 1, 2)$ and are calculated as:

$$\begin{aligned}
\mathbf{m}_1 &= \Big[\frac{\partial x}{\partial\bar{\xi}}, \frac{\partial y}{\partial\bar{\xi}}, \frac{\partial z}{\partial\bar{\xi}}\Big], \\
\mathbf{m}_2 &= \Big[\frac{\partial x}{\partial\bar{\eta}}, \frac{\partial y}{\partial\bar{\eta}}, \frac{\partial z}{\partial\bar{\eta}}\Big].
\end{aligned} \tag{4.21}$$

We introduce two parameters

$$\begin{aligned}
\lambda &= |\mathbf{m}_1^s|/|\mathbf{m}_2^s|, \\
\cos\psi &= \mathbf{m}_1^s \cdot \mathbf{m}_2^s/|\mathbf{m}_1^s||\mathbf{m}_2^s|,
\end{aligned} \tag{4.22}$$

such that the conformal transformation can be established. It can be concluded that λ reflects the local aspect ratio of the element at the source point and $\cos\psi$ indicates the distortion of the element. The influence on singular integration of these two factors will be investigated in detail in example section.

For nearly singular integration, two methods are devised. The first one is the recursive subdivision in the parametric domain and the other is a

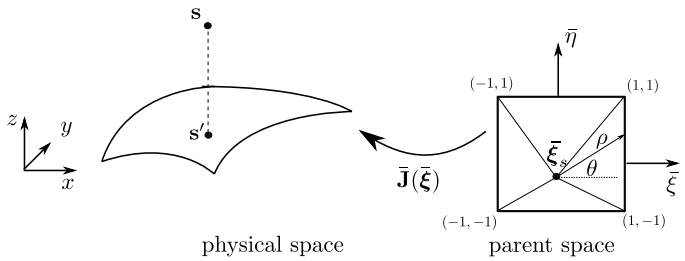

FIGURE 4.10: $L-1/5$ transformation for nearly singular integration

variable transformation technique. Note that many variable transformation techniques exist for nearly singular integration in Lagrange-based elements in literature (readers can refer to [175] for more details). However, as far as we know, these techniques were never verified for NURBS elements. We adopt an $L-1/5$ transformation, which was proposed by Hayami and Matsumoto [176]. The general procedure in Hayami's work is as follows:

(1) Find the closest point $\mathbf{s}'(\bar{\xi},\bar{\eta})$ to the source point $\mathbf{s}$ in the element of interest and the distance between them is $d=\|\mathbf{s}-\mathbf{s}'\|$;

(2) Create a projection plane composed by sub-triangles $\tilde{\triangle}_i = \mathbf{x_i s' x_{i+1}}$. These triangles can be obtained by projecting the each vertex $\mathbf{x}_i$ into the tangent plane containing $\mathbf{s}'$ [176] or simply connecting the vertex and the closest point $\tilde{\mathbf{s}'}$ which can be found by $\mathbf{s}'(\bar{\xi},\bar{\eta})$ [177];

(3) Map the parent space $(\bar{\xi},\bar{\eta})$ to the sub-triangles $\tilde{\triangle}_i$, which is in Cartesian coordinates. The Jacobian of the transformation would be $\tilde{J}$;

(4) Introduce the polar coordinate transformation in $\tilde{\triangle}_i$. The nearly singular integral of the type:

$$I=\int_S \frac{f}{r^\alpha}\mathrm{d}S, \quad \alpha\in\mathbb{N}^+, \tag{4.23}$$

can then be written as

$$I=\sum_i^{N_{\tilde{\triangle}_i}}\int_0^{\Delta\theta_i}\mathrm{d}\theta\int_0^{\rho_i(\theta)}\frac{f}{r^\alpha}\tilde{J}\rho\mathrm{d}\rho; \tag{4.24}$$

(5) Let $R(\rho) = (\rho + d)^{-\frac{1}{5}}$, the integral can be further transformed as

$$I = \sum_{i}^{N_{\tilde{\triangle}_i}} \int_0^{\Delta\theta_i} \mathrm{d}\theta \int_0^{\rho_i(\theta)} \frac{f\tilde{J}\rho}{r^{\alpha}} \frac{\mathrm{d}\rho}{\mathrm{d}R} \mathrm{d}R. \tag{4.25}$$

By introducing the exponential Jacobian term, the radial integrand is regularized to be 'smoother', thus effort on numerical quadrature is decreased.

In this work, we simply perform the polar coordinate transformation in parent space and avoid the construction of $\tilde{\triangle}_i$. This would cause two problems as stated in [177]:
(1) In $R(\rho) = (\rho + d)^{-\frac{1}{5}}$, d is in Cartesian space. Then the meaning of R is vague. This is bypassed by regularizing d with the characteristic element size h, i.e. $d_0 = d/h$;
(2) The parent space is insensitive to the element distortion. This is improved by using the conformal and Sigmoidal transformation which are used for singular integration in this work as outlined in section 3.3.1.

4.4 Numerical examples

4.4.1 Singular integration

The hyper-singular integral

$$I = \oint\!\!\!\!\!\!= \int_S \frac{1}{r^3} \mathrm{d}S \tag{4.26}$$

is verified for various geometries in this section. The related reference solutions are obtained by Mathematica©. For singular integration, three cases are involved: conformal transformation ('con'), conformal transformation and Sigmoidal transformation ('con+sig'), and the original SST ('ori'). For nearly-singular integration, two cases, the adaptive subdivision and the $L - 1/5$ transformation are compared. A Gauß-Legendre rule is used for quadrature. For the integration performed in sub-triangles (the singular integration and the nearly-singular integration by $L-1/5$ transformation),'ngp_s'

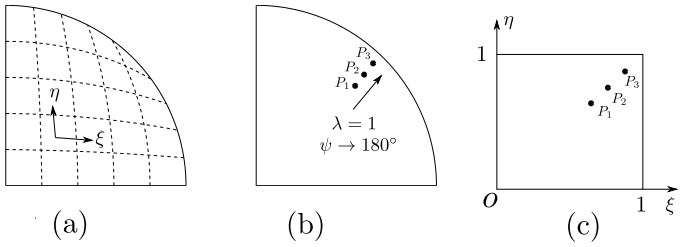

FIGURE 4.11: A quarter of a disc by Coons parametrization. (a) the parameter line; (b) the single element for singular integration with source points P_1 : $\boldsymbol{\xi}_s(0.7, 0.7)$, P_2 : $\boldsymbol{\xi}_s(0.9, 0.9)$ and P_3 : $\boldsymbol{\xi}_s(0.99, 0.99)$; (c) the parametric space

denotes the number of Gauß points in the angular direction in each sub-triangle and 'ngp_t' represents the number of Gauß points in the radial direction.

The influence of distortion angle ψ

We first verify the hyper-singular integration over a quarter of a disc given by Coons parametrization as in Figure 4.11. For the source point $\boldsymbol{\xi}_s$ moving from $(0.5, 0.5)$ to $(1, 1)$, ψ varies from $90°$ to $180°$ while λ remains 1. Thus the integral undergoes an increasing near-singularity. We take $\boldsymbol{\xi}_s$ as $(0.7, 0.7)$, $(0.9, 0.9)$ and $(0.99, 0.99)$, and ψ is equal to $123.2°$, $157.3°$ and $177.6°$ respectively. Since one element is used, only the singular integration is involved here. It can be seen from Figure 4.12 that in all the three cases, the integral converges to a stable precision with increasing ngp_s. For $\boldsymbol{\xi}_s(0.7, 0.7)$, 'con' and 'con+sig' show a very close convergence rate and reaches $O(10^{-11})$ at $ngp\_s = 14$, while the original SST uses 20 Gauß points. For $\boldsymbol{\xi}_s(0.9, 0.9)$, the decrease in convergence rate among the three cases becomes significant. And the 'con+sig' performs the best with $ngp\_s = 12$ to reach $O(10^{-8})$, which costs 28 Gauß points in the angular direction for original SST. The use of conformal transformation only provides an intermediate convergence rate. However, the convergence error increases when the source point $\boldsymbol{\xi}_s$ approaches $(1, 1)$ for a fixed $ngp\_t = 10$, especially for $\boldsymbol{\xi}_s(0.99, 0.99)$ although the improved methods show much faster convergence rates than the original method, the error is only of $O(10^{-2})$. Figure

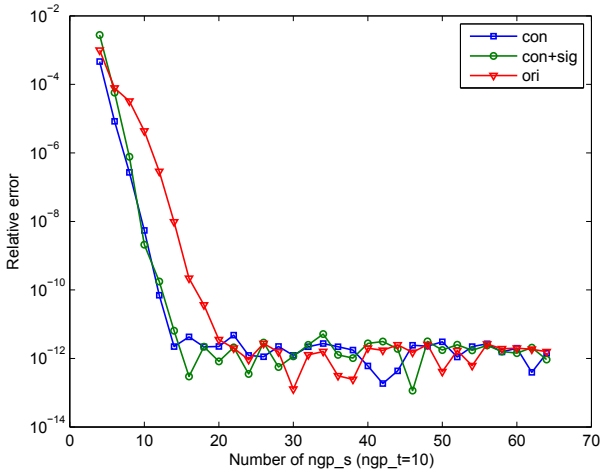

(a) $\boldsymbol{\xi}_s(0.7, 0.7)$

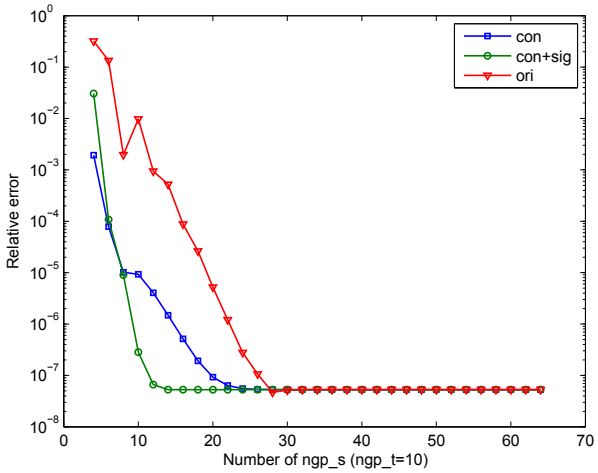

(b) $\boldsymbol{\xi}_s(0.9, 0.9)$

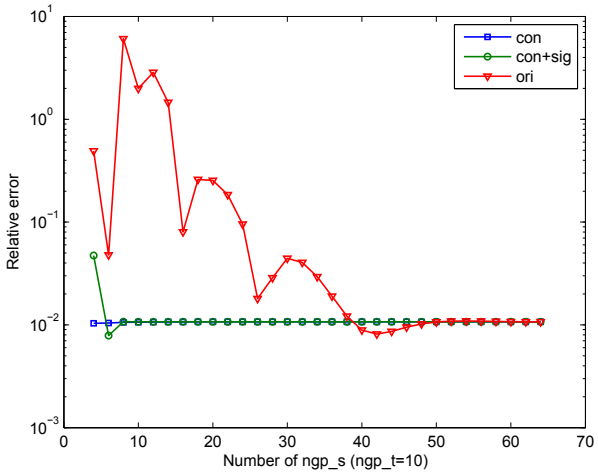

(c) $\boldsymbol{\xi}_s(0.99, 0.99)$

FIGURE 4.12: Convergence check with respect to ngp_s for hyper-singular integral over a quarter of disc by Coons parametrization

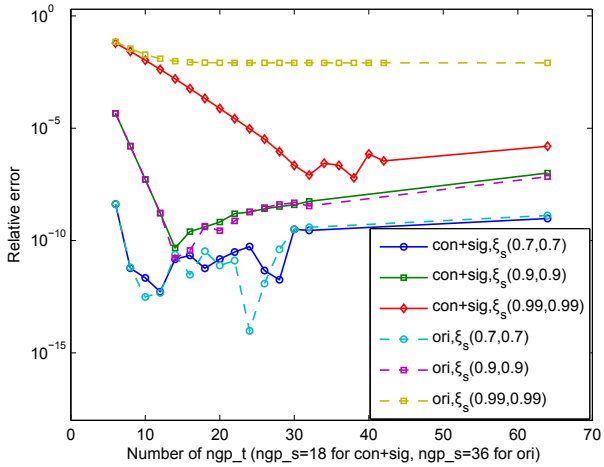

FIGURE 4.13: Convergence study with respect to ngp_t for hyper-singular integral over a quarter of disc by Coons parametrization

4.13 illustrates the study with an increasing number of Gauß points in radial direction ngp_t, while fixing the number of Gauß point in the angular direction ngp_s. We fixed $ngp\_s = 18$ for the improved method and $ngp\_s = 36$ for the original method since we note that the original method needs more Gauß points in the angular direction to converge. It can be observed that the improved method shows the same convergence trend as the original method with respect to the number of Gauß Points in the radial direction. And both methods achieve $O(10^{-10})$ for $\boldsymbol{\xi}_s$ at $(0.7, 0.7)$ and $(0.9, 0.9)$ when ngp_t is 14. However, further increasing the number of Gauß points in the radial direction leads to an accumulation of the integration error. For $\boldsymbol{\xi}_s$ at $(0.99, 0.99)$, the original method converges to $O(10^{-2})$ with increasing the ngp_t while the improved method reaches $O(10^{-7})$. This is due to the fact that even 36 Gauß points in the angular direction is insufficient to circumvent the near-singularity in the integrand for the original method.

The influence of local aspect ratio λ

We still perform the hyper-singular integral over a quarter disc, but with the parametrization degenerated at the pole as in Figure 4.14 such that the distortion angle ψ is always $90°$ regardless of $\boldsymbol{\xi}_s$. For $\boldsymbol{\xi}_s$ moving from $(0.5, 0.5)$ to $(0.5, 0)$, the local aspect ratio λ changes from 1 to $+\infty$ (assume $\lambda \geq 1$).

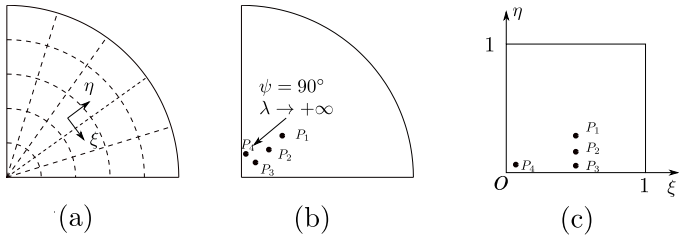

FIGURE 4.14: A quarter of a disc by parametrization degenerated at the pole. (a) the parameter line; (b) the single element for singular integration with source points $P_1 : \boldsymbol{\xi}_s(0.5, 0.1)$, $P_2 : \boldsymbol{\xi}_s(0.5, 0.01)$, $P_3 : \boldsymbol{\xi}_s(0.5, 0.0.001)$ and $P_4 : \boldsymbol{\xi}_s(0.001, 0.001)$; (c) the parametric space

We take $\boldsymbol{\xi}_s$ at $(0.5, 0.1)$, $(0.5, 0.01)$, $(0.5, 0.001)$ and $(0.001, 0.001)$, and λ is 6.0, 60.3, 603.6 and 706.7, respectively. The convergence results with respect to the number of Gauß points in the angular direction ngp_s while keeping $ngp\_t = 10$ and the errors of the integral are compared in Figure 4.15. We can see that for all cases, the 'con+sig' scheme outperforms with the fastest convergence rate and the smallest error (for the former three positions of $\boldsymbol{\xi}_s$, the precision at $O(10^{-12})$ with about 20 Gauß points in the angular direction). The conformal transformation only shows a better convergence than the original method, but both methods fail to get converged at a stable precision with increasing λ. For $\boldsymbol{\xi}_s(0.001, 0.001)$, the integral by the original method results in arbitrary values thus its error curve is not plotted in Figure 4.15(d). The 'con+sig' scheme converges at $O(10^{-6})$ with 14 Gauß points in the angular direction and the conformal transformation only presents a slow convergence and higher error than 'con+sig' finally although the error is much lower than 'con+sig' when $ngp\_s < 12$.

We also studied the error convergence trend with respect to the number of Gauß points in the radial direction ngp_t with a fixed $ngp\_s = 18$ for the improved method and $ngp\_t = 36$ for the original method. We can conclude from Figure 4.16 that the integral shows a stable behavior for these cases, while with too many Gauß points in the radial direction, the error starts to accumulate slowly. The accuracy is poor by the original method for $\boldsymbol{\xi}_s$ at $(0.5, 0.01)$ and $(0.5, 0.001)$, due to the fact that $ngp\_s = 36$ is far from sufficient to overcome the near-singularity.

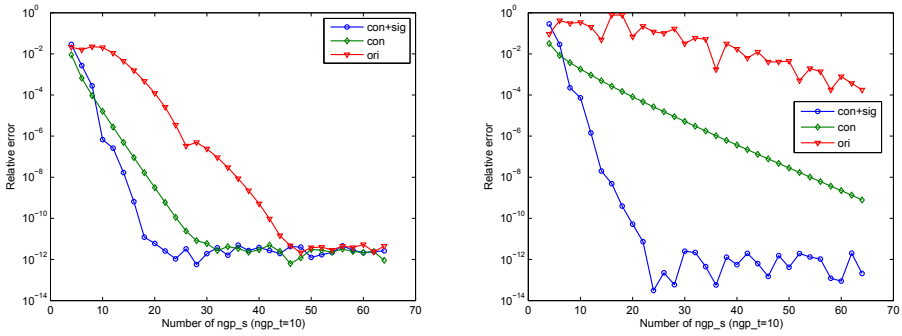

(a) $\boldsymbol{\xi}_s(0.5, 0.1)$ (b) $\boldsymbol{\xi}_s(0.5, 0.01)$

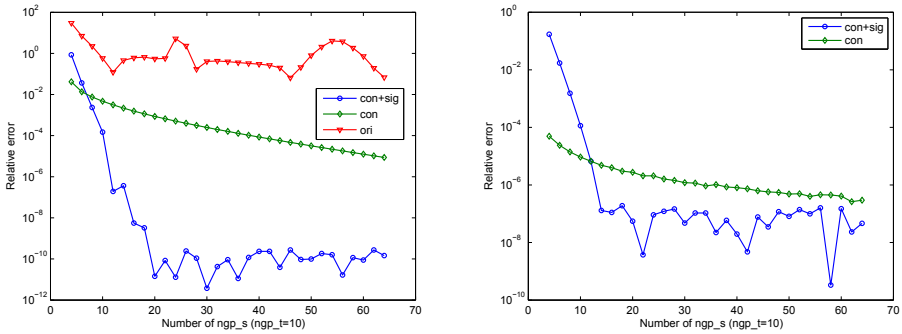

(c) $\boldsymbol{\xi}_s(0.5, 0.001)$ (d) $\boldsymbol{\xi}_s(0.001, 0.001)$

FIGURE 4.15: Convergence study with respect to ngp_s for hyper-singular integral over a quarter of disc by parametrization degenerated at the pole

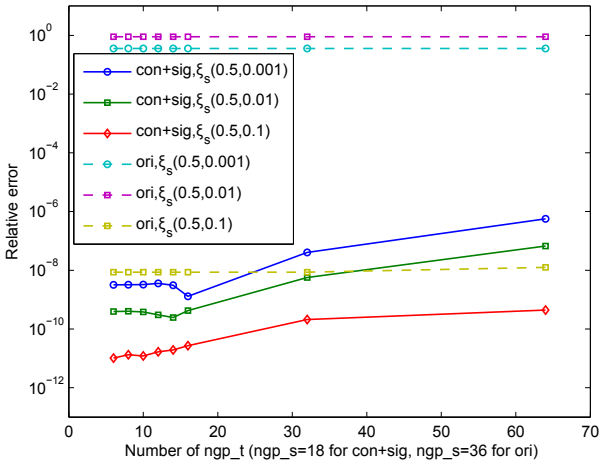

FIGURE 4.16: Convergence study with respect to ngp_t for the hyper-singular integral over a quarter of a disc by parametrization degenerated at the pole

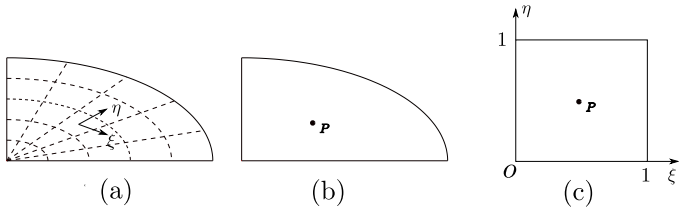

FIGURE 4.17: A quarter of an ellipse by parametrization degenerated at the pole. (a) the parameter line; (b) the single element for singular integration with source points $P : \boldsymbol{\xi}_s(0.5, 0.5)$; (c) the parametric space

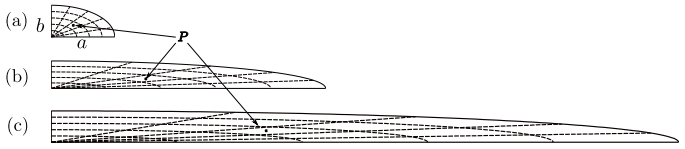

FIGURE 4.18: A quarter of an ellipse by parametrization degenerated at the pole with source point $P : \boldsymbol{\xi}_s(0.5, 0.5)$. (a) $a/b = 2$, $\lambda = 1.2$ and $\psi = 53.1°$ for P; (b) $a/b = 10$, $\lambda = 1.2$ and $\psi = 11.4°$ for P; (c) $a/b = 20$, $\lambda = 1.2$ and $\psi = 5.7°$ for P

Performance for complex distortion

First of all, we define what we mean by 'complex distortion': (1) the distortion angle ψ gets close to π and the local aspect ratio λ deviates from 1; (2) The parameter line shows an obvious change in direction within an element. For example, a quarter of an ellipse with parametrization degenerated at the pole has a close-to-unit λ at its parametric center point regardless the variation of the ratio of semi-major and semi-minor axes (a/b) as illustrated in Figure 4.18. We use a single element to discretize the quarter of an ellipse and place $\boldsymbol{\xi}_s$ at $(0.5, 0.5)$ (Figure 4.17), then perform the hyper-singular integral over the domain with $a/b = 2, 10$ and 20. The results are plotted in Figure 4.19. It can be observed that both the improved method and the original method present close convergence trends with respect to ngp_s. And they can achieve low error at $O(10^{-12})$ for small a/b, but the integral becomes divergent when a/b is larger. Table 4.1 and 4.2 list the value of the components of the integral. It can been observed that for $a/b = 2$, all terms achieve an error below $O(10^{-7})$ within 22 Gauß points. While for $a/b = 20$, the terms I_{-1}, I_{-2} and I_{line} easily reach the $O(10^{-7})$ with 22 Gauß points, nevertheless I_0 has a poor precision. It can be seen that for complex

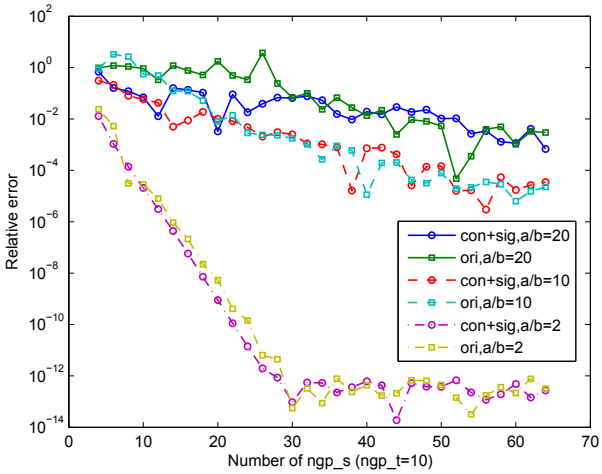

FIGURE 4.19: Convergence check with respect to ngp_s for hyper-singular integral over a quarter of ellipse with varied a/b

distortion of the geometry, it is the bad quadrature in I_0 that leads to the poor accuracy in the final integration.

A remedy for this deterioration would be to perform certain mesh refinement as in Figure 4.21(c) with $\omega = 0.01$ (see Figure 4.21(c) for the definition), i.e. knot insertions in NURBS. Then multiple elements are used to discretize the domain and near-singular integration is introduced. We use the adaptive subdivision scheme for nearly-singular integration. The convergence is checked for the case of $a/b = 20$ with respect to the ngp_s in the singular element which is shown in Figure 4.20. It is seen that with certain mesh refinement, the improved method achieves a fast convergence as previous case studies and reaches $O(10^{-8})$ with about 20 Gauß point in the angular direction, while the original method remains poor accuracy and slow convergence rate. This example indicates a quadrature scheme for geometries with complex distortion, which we name 'transformation+subdivision' scheme. We note that the final result of singular integration by this method is determined by both singular and nearly-singular integration, and it will studied further in the next section.

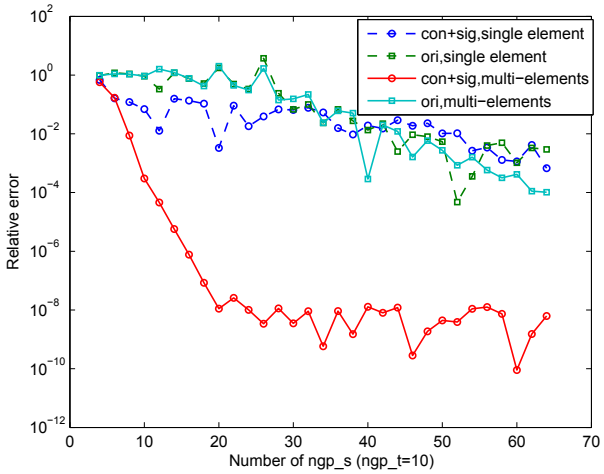

FIGURE 4.20: Convergence check with respect to ngp_s for hyper-singular integral over a quarter of ellipse with $a/b = 20$

ngp_s	I_0	I_1	I_2
4	8.2892124e+03	8.2941725e+03	2.4757973e-14
6	8.2898314e+03	8.2942830e+03	6.9305672e-14
8	8.2898699e+03	8.2942821e+03	6.3671290e-14
10	8.2898749e+03	8.2942821e+03	8.2156503e-15
12	8.2898757e+03	8.2942821e+03	5.4206639e-14
14	8.2898758e+03	8.2942821e+03	-2.7339241e-15
16	8.2898758e+03	8.2942821e+03	1.7486012e-14
18	8.2898758e+03	8.2942821e+03	1.7402745e-14
20	8.2898758e+03	8.2942821e+03	-2.3064883e-14
22	8.2898758e+03	8.2942821e+03	1.9602375e-16

ngp_s	I_{line}	I
4	-3.7700784e+01	-4.2660963e+01
6	-3.7701286e+01	-4.2152800e+01
8	-3.7701282e+01	-4.2113450e+01
10	-3.7701282e+01	-4.2108479e+01
12	-3.7701282e+01	-4.2107735e+01
14	-3.7701282e+01	-4.2107622e+01
16	-3.7701282e+01	-4.2107606e+01
18	-3.7701282e+01	-4.2107604e+01
20	-3.7701282e+01	-4.2107604e+01
22	-3.7701282e+01	-4.2107604e+01

TABLE 4.1: Convergence study of integrals with respect to ngp_s when fixing $ngp\_t = 10$ for a quarter of ellipse with $a/b = 2$

ngp_s	I_0	I_1	I_2
4	6.0095571e+03	6.0985633e+03	-5.3383686e-13
6	6.0632550e+03	6.0790875e+03	1.3248356e-12
8	6.0638743e+03	6.0777228e+03	-4.8755812e-13
10	6.0712094e+03	6.0776900e+03	3.5870503e-13
12	6.0693107e+03	6.0776896e+03	4.8955425e-13
14	6.0738115e+03	6.0776896e+03	6.9030751e-13
16	6.0631426e+03	6.0776896e+03	-1.9533745e-13
18	6.0645280e+03	6.0776896e+03	-2.0992392e-13
20	6.0687301e+03	6.0776896e+03	6.7663279e-13
22	6.0718837e+03	6.0776896e+03	7.9022942e-14

ngp_s	I_{line}	I
4	-2.7720742e+01	-1.1672697e+02
6	-2.7632216e+01	-4.3464761e+01
8	-2.7626013e+01	-4.1474569e+01
10	-2.7625863e+01	-3.4106492e+01
12	-2.7625861e+01	-3.6004716e+01
14	-2.7625861e+01	-3.1503924e+01
16	-2.7625861e+01	-4.2172826e+01
18	-2.7625861e+01	-4.0787458e+01
20	-2.7625861e+01	-3.6585377e+01
22	-2.7625861e+01	-3.3431702e+01

TABLE 4.2: Convergence study of integrals with respect to ngp_s when fixing $ngp\_t = 10$ for a quarter of ellipse with $a/b = 20$

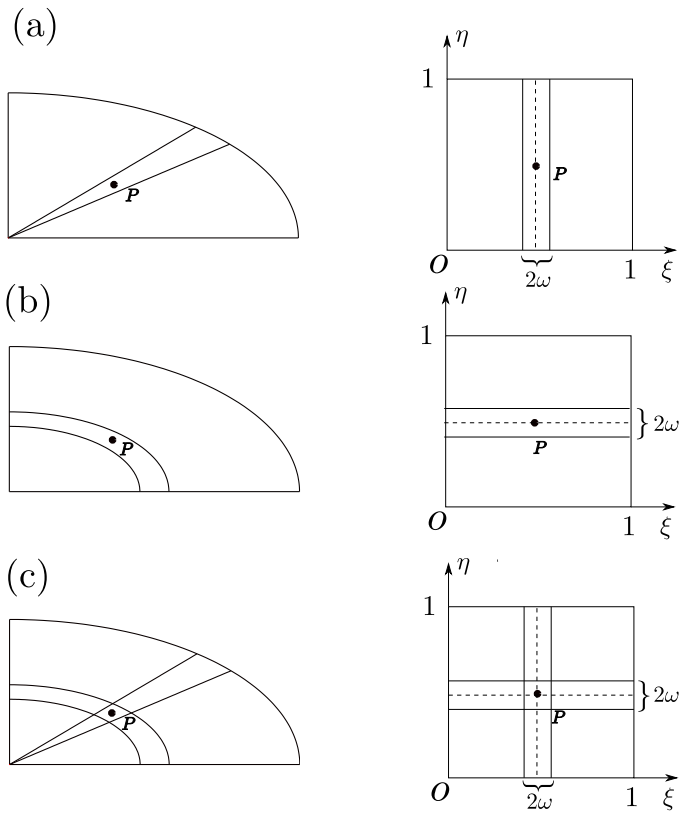

FIGURE 4.21: The hyper-singular integral over a quarter of an ellipse with different mesh design. (a) mesh A with knot vectors $\boldsymbol{\xi}$: $[0,0,0,0.5-\omega,0.5+\omega\,1,1,1]$, $\boldsymbol{\eta}$: $[0,0,0,1,1,1]$; (b) mesh B with knot vectors $\boldsymbol{\xi}$: $[0,0,0,1,1,1]$, $\boldsymbol{\eta}$: $[0,0,0,0.5-\omega,0.5+\omega\,1,1,1]$; (c) mesh C with knot vectors $\boldsymbol{\xi}$: $[0,0,0,0.5-\omega,0.5+\omega,1,1,1]$, $\boldsymbol{\eta}$: $[0,0,0,0.5-\omega,0.5+\omega,1,1,1]$;

4.4.2 Nearly-singular integration

In this section the nearly-singular integration by the proposed $L-1/5$ transformation is studied in detail. We take a quarter of an ellipse with $a/b = 2$ as an example. Three mesh refinement configurations are set up as in Figure 4.21 such that the near-singularity arises in the neighborhood of the singular element by introducing a *relative distance factor* ω (see explanation in Figure 4.21). Note that the effect of different spatial positions of the source point and nearly-singular element can be checked as the same time. For the singular element, $ngp\_s = 18$ and $ngp\_t = 10$ will be fixed. And for the nearly-singular element, we increase the ngp_s and ngp_t from 4 to 80 respectively. The integration error for all the cases is plotted in Figure 4.22. For all the mesh configurations, the $L - 1/5$ transformation can achieve $O(10^{-6})$ with about 20 Gauß points in both the radial and the angular directions for each sub-triangle. And the convergence trend is similar in both directions. The accuracy can be maintained with $\omega = 0.001$. By further reducing the value of ω, the error will increase. How to improve the precision for nearly-singular integration will be further explored in future work.

Table 4.3 presents the reduction in the total number of Gauß points if compared with the recursive subdivision scheme. It can be seen that the total number of Gauß points is reduced by two orders of magnitude when $\omega \leq 0.01$ for all the mesh configurations.

	mesh A			mesh B		
ω	0.1	0.01	0.001	0.1	0.01	0.001
$L-1/5$ transform	512	800	768	480	640	768
subdivision	4644	22572	47844	3672	20736	44244

	mesh C		
ω	0.1	0.01	0.001
$L-1/5$ transform	2304	3840	4608
subdivision	5148	21960	46188

TABLE 4.3: Number of Gauß points needed to reach $O(10^{-6})$

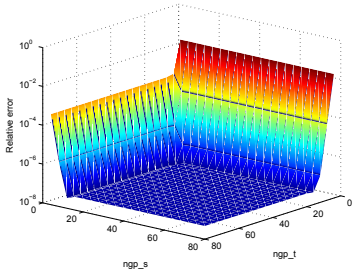

(a) mesh A with $\omega = 0.1$

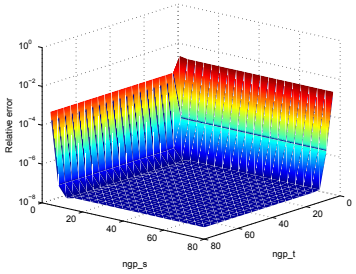

(b) mesh B with $\omega = 0.1$

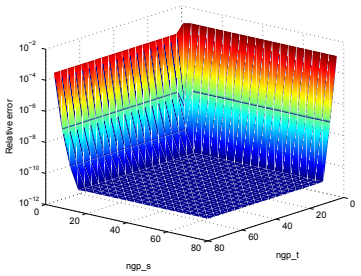

(c) mesh C with $\omega = 0.1$

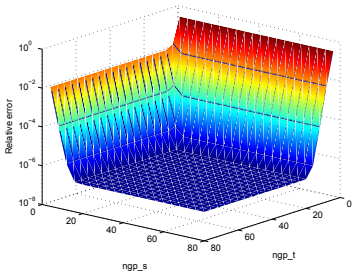

(d) mesh A with $\omega = 0.01$

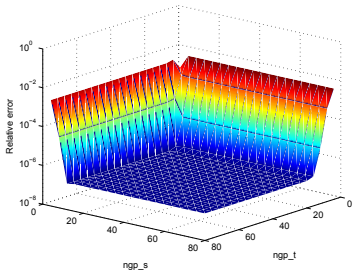

(e) mesh B with $\omega = 0.01$

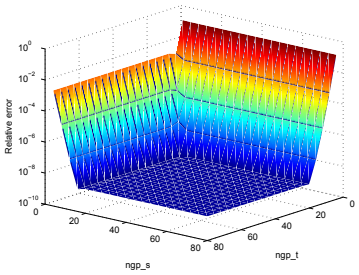

(f) mesh C with $\omega = 0.01$

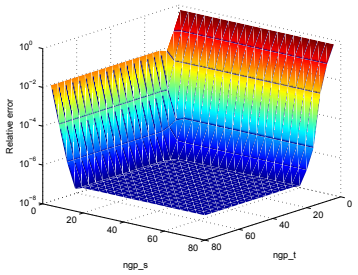

(g) mesh A with $\omega = 0.001$

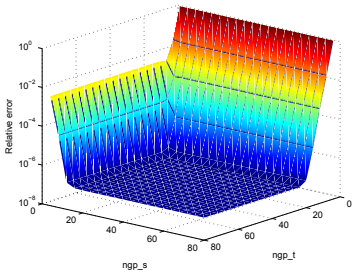

(h) mesh B with $\omega = 0.001$

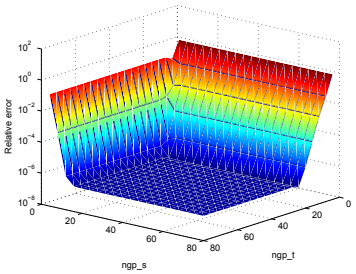

(i) mesh C with $\omega = 0.001$

FIGURE 4.22: Convergence study ('z' direction is the relative error and 'x', 'y' are number of Gauß Points in the angular and the radial direction of each sub-triangle respectively) for nearly-singular integration by $L - 1/5$ transformation

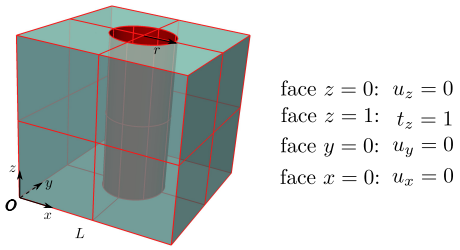

FIGURE 4.23: The central of a cube trimmed by a cylindrical surface (red). The unspecified degrees of freedom are zero tractions

4.4.3 Examples of Trimmed NURBS

Two case studies are performed to evaluate the proposed methods for trimmed NURBS. The relative error in displacement or traction L_2 norm over the boundary of the domain is used to measure the accuracy of the results. They are given as:

$$\begin{aligned} \|e_u\|_{L_2} &= \sqrt{\frac{\int_S (\mathbf{u} - \mathbf{u}_{\text{ext}})(\mathbf{u} - \mathbf{u}_{\text{ext}})^{\mathrm{T}} \mathrm{d}S}{\int_S \mathbf{u}_{\text{ext}} \mathbf{u}_{\text{ext}}^{\mathrm{T}} \mathrm{d}S}}, \\ \|e_t\|_{L_2} &= \sqrt{\frac{\int_S (\mathbf{t} - \mathbf{t}_{\text{ext}})(\mathbf{t} - \mathbf{t}_{\text{ext}})^{\mathrm{T}} \mathrm{d}S}{\int_S \mathbf{t}_{\text{ext}} \mathbf{t}_{\text{ext}}^{\mathrm{T}} \mathrm{d}S}}, \end{aligned} \tag{4.27}$$

where the subscript 'ext' denotes the analytical solution. The default order of the basis functions is 2. In the degree elevation process, the highest order will be 3.

Patch test

A cube with edge $L = 1$ cut by a cylindrical surface with radius r at its centre is studied in this section as in Figure 4.23. The faces $x = 0$, $y = 0$ and $z = 0$ are subjected to normal displacement constraints and the top face $z = 1$ is subjected to a uniform traction in the z direction. The remaining degrees of freedom are traction-free. The material constants $E = 1000$ and $\nu = 0.3$ such that the analytical displacement field over the domain would be:

$$\begin{aligned} u_x(x, y, z) &= -\frac{\nu x}{E}, \\ u_y(x, y, z) &= -\frac{\nu y}{E}, \\ u_z(x, y, z) &= \frac{z}{E}. \end{aligned} \tag{4.28}$$

Since the stress field is constant in this example and the geometry is exactly represented, the source of numerical error comes only from the integration scheme.

The aforementioned collocation schemes are first investigated on a quarter of the trimmed cube with $r = 0.15$ for the cylindrical surface to check the singular integration for the pentagon-type elements in the trimmed NURBS geometry. Figure 4.24 illustrates collocation scheme A (the collocation points are in the sub-quadrilateral with all straight edges) and scheme B (the collocation points in the sub-quadrilateral with the curved edge) for a coarse mesh (4 elements) and a fine mesh (9 elements). When the collocation points are placed in one sub-quadrilateral, the integration over the other sub-quadrilateral will be performed as a regular one (the nearly singular quadrature is used). It can been seen that for the collocation points in scheme A, good parametrization is obtained for singular integration. While in scheme B, the collocation points are located in the sub-quadrilateral with a highly distorted parametrization, which will increase the difficulty for singular integration. Two singular integration methods are compared. One is performing the singular integration with the conformal and Sigmoidal transformations directly (denoted by 'trans'); The other will subdivide the parametric space as was done in Figure 4.21 and then the relative transformations will be adopted for singular integration and the remaining subdomains will be treated with nearly singular integration (i.e the 'transformations+subdivision' or 'trans+subdi' for short). The coefficient $\omega = 0.01$ is taken for the subdivision. Table 4.4 presents the results of relative error in the displacement L_2 norm for the test. It can be observed that scheme A achieves orders of magnitude higher precision than scheme B in singular integration scheme 'trans', due to the complex distortion of the parametrization. Analogous to the example in Section 4.4.1, the 'trans+subdi' method improves the results when the collocation points are in the distorted subquadrilateral. It is seen that for mesh (b), the 'trans+subdi' method achieves the same order ($O(10^{-7})$) for both collocation schemes A and B, while for mesh (c), the 'trans+subdi' only reaches $O(10^{-4})$ although two orders of

magnitude higher than 'trans'. Reducing ω is supposed to further improve the precision. However due to the restriction in nearly singular integration, the final result would not further improve. This requires a further local refinement closed to the trimming curve in the untrimmed mesh to reduce the distortion of trimmed elements.

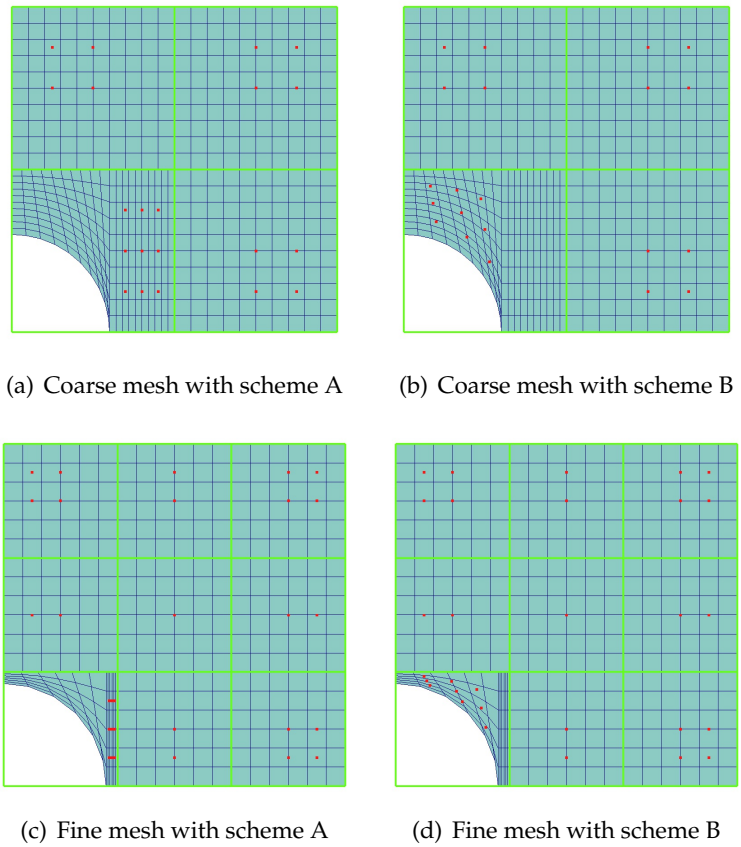

(a) Coarse mesh with scheme A (b) Coarse mesh with scheme B

(c) Fine mesh with scheme A (d) Fine mesh with scheme B

FIGURE 4.24: Collocation scheme for pentagon-type trimmed element in top face of the cube. The green line is the untrimmed element boundary; the blue line denotes the parameter line and red dots are collocation points

Then the whole model is used and 4 mesh configurations are obtained by uniform knot insertion for the untrimmed cube (Figure 4.25). The collocation scheme A for the pentagon-type trimmed elements in the mixed collocation method and 'trans+subdi' singular quadrature method for the trimmed elements are used for all 4 meshes. Table 4.5 presents the relative error in the displacement L_2 norm for both mixed and GA collocation. It can be observed that the smallest error reached $O(10^{-8})$ for both collocation methods. The GA collocation maintains the error below $O(10^{-5})$. The

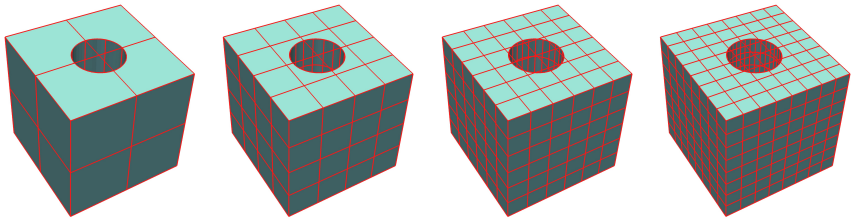

(a) (b) (c) (d)

FIGURE 4.25: Meshes of the trimmed cube

mixed collocation method obtains better accuracy however for mesh 3 in Figure 4.25, the error is of $O(10^{-4})$. This is because the collocation points in the small triangle-type trimmed elements will lead to nearly-singular integration. We note that both cases give smaller error than the result in [122] where the error stays of $O(10^{-3})$ although it was given as a discretized L_2 norm for some selected points.

Convergence test

In this section, the convergence behavior of the IGABEM for the trimmed NURBS is studied by applying the Kelvin fundamental solution to the trimmed geometry. The cube cut by the cylindrical surface in the patch test is used. And a unit point force in the z direction is applied at $\mathbf{s}_P(0, 0, 1.5)$, then the corresponding displacement and traction fields in the closed domain

	mesh (b)		mesh (c)	
	scheme A	scheme B	scheme A	scheme B
trans	2.615e-06	1.922e-03	2.485e-08	9.785e-02
trans+subdi	6.135e-07	4.989e-07	1.638e-07	4.273e-04

TABLE 4.4: Comparison of relative error in the displacement L_2 norm by two singular integration methods ('trans' denotes only the transformations are used and 'trans+subdi' means transformations and subdivision of the singular element are both used) and two collocation scheme ('scheme A' puts the collocation points in the quadrilateral with all straight edges and 'scheme B' places the collocation points in the quadrilateral with the curved edge)

mesh	mixed collocation	GB collocation
1	7.340474e-07	3.183425e-05
2	3.909840e-08	2.436823e-08
3	3.951035e-04	2.741819e-05
4	2.224108e-08	5.064460e-06

TABLE 4.5: Relative error in the displacement L_2 norm for two collocation schemes

$\bar{\Omega}$ caused by the point force are

$$\begin{aligned} u_i(\mathbf{x}) =& \frac{1}{16\pi\mu(1-\nu)r}[(3-4\nu)\delta_{i3} + r_{,i}r_{,3}], \\ t_i(\mathbf{x}) =& -\frac{1}{8\pi(1-\nu)r^2}\Big\{\frac{\partial r}{\partial n}[(1-2\nu)\delta_{i3} + 3r_{,i}r_{,3}] - \\ & (1-2\nu)(r_{,i}n_3 - r_{,3}n_i)\Big\}, \quad \forall \mathbf{x} \in \bar{\Omega}, \end{aligned} \tag{4.29}$$

where $r = |\mathbf{s}_P - \mathbf{x}|$ and $\mathbf{n}$ is the unit out normal. The material constant $\mu = \frac{E}{2(1+\nu)}$. We take $\mu = 1$ and $\nu = 0.3$ for the case study.

Figure 4.26 compares the two collocation methods for the pure Dirichlet boundary condition (BC). Since the displacement fields for all the faces are prescribed by the L_2 projection at the beginning of analysis, the error can be considered as the approximation error and it is the same for the two collocation methods. It can be observed that both methods can obtain a converging behavior in traction fields. The result of the GA collocation is more accurate than that of the mixed collocation. Based on this, we select the GA collocation for further studies.

Figure 4.27 shows the convergence curves for a degree elevation of the basis functions from $p = 2$ to 3 for the pure Dirichlet BC. The optimal order of convergence rates (ocr) of the prescribed displacement fields for both $p = 2$ ($ocr = 3.04$) and $p = 3$ ($ocr = 4.26$) are obtained. For the traction fields, the order elevation will reduce the error. However we note that for both cases, the convergence results are sub-optimal. And the ocr for $p = 3$ (1.95) is worse than for $p = 2$ (2.46). One possible reason could be that the integration error is not small enough compared to the approximation error to give an optimal convergence. For this example, the integration error is known to be $O(10^{-5})$ from the patch test. And the approximation error

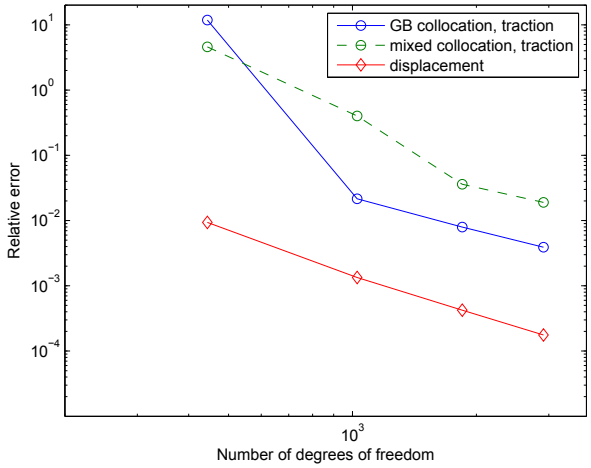

FIGURE 4.26: Comparison of the two collocation methods for a pure Dirichlet problem in the convergence study

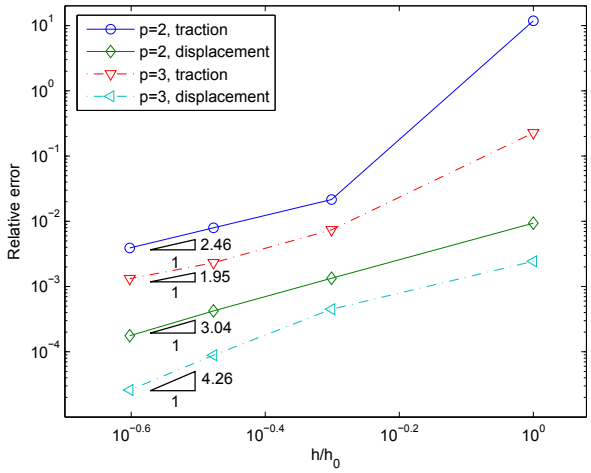

FIGURE 4.27: Relative error in displacement and traction fields for pure dirichlet boundary condition

of the problem can be known from the prescribed displacement fields. It can be seen that after degree elevation, the approximation error approaches closely to $O(10^{-5})$, which is almost in the same level as the integration error. This may explain the deterioration in ocr for $p = 3$ compared to $p = 2$.

The case of mixed BCs is then tackled where the top $z = 1$ and bottom $z = 0$ faces are Dirichlet BC and the remaining faces are subjected to Neumann BCs. Figure 4.28 compares the convergence results for the displacement and traction fields for pure Dirichlet BCs and mixed BCs. It can be observed that convergence can be obtained for mixed BCs as well.

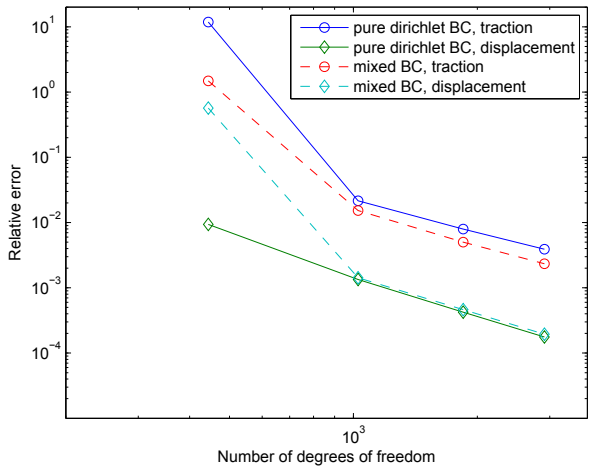

FIGURE 4.28: Relative error in displacement and traction fields for pure dirichlet boundary condition and mixed boundary condition

4.4.4 Edge crack

In this section a surface edge crack modeled by the phantom element method is tackled. Figure 4.29(a) illustrates the numerical model of the edge crack, where the top and bottom faces are subjucted the uniform traction in the normal direction. The unspecified faces are traction-free. The material constants are $E = 1000$ and $\nu = 0.3$. Figure 4.29(b) gives the deformation plot of the edge crack. Figure 4.30 compares the normalized K_I from the center point of the crack front along the direction Oz' with the results from Lagrange-based BEM by Mi and Aliabadi [42] and FEM solution by Raju and Newman [178], as well as the reference solution from plane strain condition. It can be observed that K_I agrees well with the Lagrange-based BEM solution and the plane strain solution closed to the center point. When the sample point approaches the free lateral face, K_I is reduced due to a weaker crack tip singularity than $\sqrt{\rho}$ on the free face.

This example exhibits the possibility to model the surface crack problem using IGABEM while the original parametrization can be preserved. Further verification in the surface crack propagation for non-trivial industrial parts will be done in the future work.

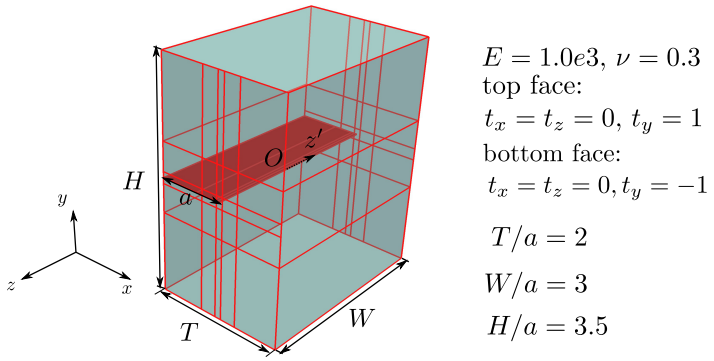

(a) Model of edge crack

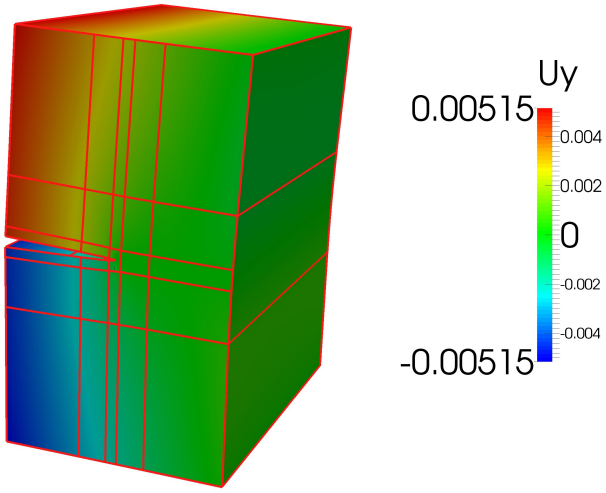

(b) Deformation of the edge crack

FIGURE 4.29: Edge crack

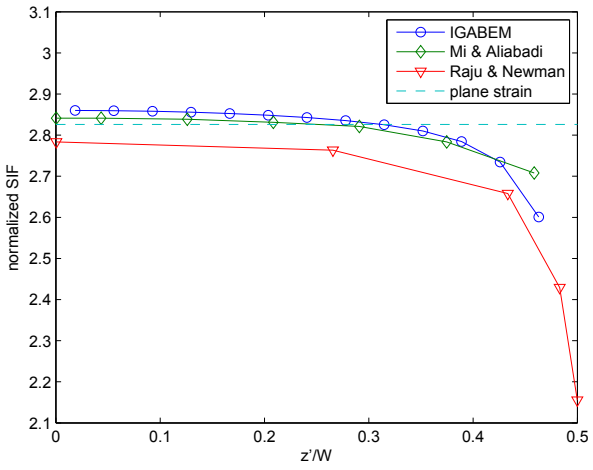

FIGURE 4.30: Relative error in $K_I/\sqrt{\pi a}$

4.5 Conclusions

In this chapter several numerical aspects, such as singular integration, trimmed NURBS and surface crack modeling, of the IGABEM were investigated in detail. The singular and nearly singular integration were studied for NURBS elements with high aspect ratios or elemental distortion, which were then to be important factors influencing the accuracy of trimmed NURBS implementation. The conclusions are

(1) Singular integration is sensitive to the element shape (or parametrization quality) and distorted elements usually with bad quality parametrizations leads to a deterioration of the accuracy of the singular integral. The proposed 'transformation+subdivision' scheme is shown to be a remedy for this issue in IGABEM;

(2) The new proposed IGABEM for trimmed NURBS is able to handle closed trimming curve and multi-curves in a single patch;

(3) The proposed surface crack modeling allows the crack to split the boundary of the body while preserving the original parametrization provided by the CAD model.

Chapter 5

Conclusions and future work

This thesis outlines an isogeometric boundary element method (IGABEM) to simulate crack growth directly from CAD, without meshing or remeshing at any stage of the simulation. NURBS functions are used to approximate both the geometry and field variables. This approximation is found to offer significant savings in human intervention through the circumvention of mesh generation and to provide superior accuracy properties over conventional discretization procedures in linear elastostatics.

- In chapter 2, the dual boundary integral equations are introduced such that cracks can be modeled within a single domain. The crack tip graded mesh refinement and partition of unity (PU) enrichment are compared to capture the crack tip singularity. It is found that both methods can significantly improve the solution accuracy near the crack tip. PU enrichment achieves an accuracy which is intermediate between that of consecutive knot insertions at $(1/2)^3$ and $(1/2)^4$ of the distance to the crack tip in parametric space while the convergence rate is improved by 55% compared to graded mesh refinement. Popular approaches to extract SIFs are compared in the framework of IGABEM which indicates that the M integral is more efficient for SIF extraction in IGABEM. The IGABEM also provides a higher accuracy than Lagrange basis based BEM for the same model size or number of DOFs. The convergence rate in SIFs is improved by 5 to 8 times compared to BEM with a discontinuous Lagrange basis without any treatment of the crack tip; The cracks are modeled directly by

NURBS, and an algorithm for modifying the NURBS crack is developed to describe the crack during propagation. The proposed crack growth procedure can lead to C^1 smooth crack trajectories and agrees well with those results from XFEM. Finally we present an example of crack growth in a spanner to illustrate the procedure for damage tolerance assessment directly from CAD, which does not require any mesh (re)generation.

- Chapter 3 focuses on IGABEM for simulating 3D fatigue fracture problems. We extend the improved singularity subtraction technique [154] to quadrilateral elements such that it can be applied to tensor-product NURBS basis functions. The proposed singular integration scheme preserves the quadrature accuracy for elements with large aspect ratios. Both the crack opening displacement form and the dual equations of IGABEM are compared. By graded mesh refinement in the direction where the crack tip singularity varies, the convergence rate can be improved by a factor of two and accuracy by one order, compared to uniform refinement. This indicates the efficiency of IGABEM in the application of fracture problems.

  Two ways to extract SIFs, the contour-based M integral and virtual crack closure integral, are compared. The local crack tip system is setup naturally and uniquely thanks to the NURBS representation of the crack surface. Combining with the continuity of the stress solution in BEM, the obtained SIFs along the crack front are smooth and accurate. An algorithm to propagate the NURBS-represented crack surface is presented and the stability is verified, even for high Paris law indices, due to the smoothness in crack front geometry and numerical SIFs.

- In chapter 4, several numerical aspects, such as singular integration,

trimmed NURBS and surface crack modeling, of the IGABEM are investigated in detail. Singular and nearly singular integration are studied for NURBS elements with high aspect ratios or elemental distortion. Singular integration exhibits certain sensitivity to the element shape (or parametrization quality) and to element distortion, usually because of blow quality parametrization. This leads to a deterioration of the accuracy of the singular integral. The proposed 'transformation+subdivision' scheme is shown to be a remedy for this issue of IGABEM. The implementation of IGABEM for trimmed NURBS is able to handle closed trimming curves within a single patch. Convergence result is observed for the manufactured solution, which confirms that the levels of integration error and approximation error have a strong influence on the convergence rate. The proposed phantom element method for surface crack modeling allows the crack to split the boundary of the body while preserving the original parametrization.

Future work may be pursued on:

- More effective algorithms are needed to achieve higher accuracy in (nearly) singular integration for highly distorted elements. Efforts should be expended on improving the integration routine or improving the parametrization quality. Since spline based basis functions are used for the analysis, almost no discretization error is introduced in the model, thus the integration error is the major source of numerical model error. While the singular integration or nearly singular integration is rarely studied for highly distorted elements in literature. This is due to the fact that element shapes tend to be regular in traditional Lagrange-based mesh discretization with mesh refinement. Nevertheless, the elements in IGA can still be distorted after mesh refinement. We should be aware that even in FEM based work, the parametrization quality has significant influence on numerical results. Thus analysis-suitable parametrization should be developed, for example [109].

- Acceleration algorithm are necessary if we put IGABEM into practical use. Although the use of spline-based functions helps reduce the model size, the model is still large when it comes to non-trivial geometries. For example for crack propagation, the mesh density usually should be much higher than for non-cracked part in order to obtain reliable fracture parameters. Algorithms such as the fast multipole method or adaptive cross approximation based on hierarchical matrices and parallelization approaches could be fruitful directions.

- T-spline based local refinement strategies could benefit IGABEM. (a) In chapter 4, we reduce the continuity between elements to C^{-1} such that the crack tip can be located inside an element when using the phantom element method. However this can be further improved by locally reducing the continuity at the crack tip element whilst the basis functions of thew non-cracked part can still preserve smoothness; (b) In the representation of trimmed NURBS, local refinement can help convert the 'unknown' trimmed elements into the 'known' types.

- More robust collocation schemes are pursued for trimmed NURBS and surface crack modeling. Alternatives could be Galerkin BEM or IGA Nyström method [179].

Appendix A

Fundamental solutions for elasticity

The fundamental solutions for displacement boundary integral equation (BIE) are given by

$$\begin{aligned} U_{ij}(\mathbf{s},\mathbf{x}) =& \frac{1}{8\pi\mu(1-\nu)}\left[(3-4\nu)\delta_{ij}\ln\left(\frac{1}{r}\right)+r_{,i}r_{,j}\right], \\ T_{ij}(\mathbf{s},\mathbf{x}) =& -\frac{1}{4\pi(1-\nu)r}\Big\{\frac{\partial r}{\partial n}[(1-2\nu)\delta_{ij}+2r_{,i}r_{,j}]- \\ & (1-2\nu)(r_{,i}n_j-r_{,j}n_i)\Big\}, \end{aligned} \tag{A.1}$$

for $2D$ under plane strain conditions, where $\mu = E/[2(1+\nu)]$, E is Young's Modulus and ν Poisson's ratio. For traction BIE,

$$K_{ij} = \frac{1}{4\pi(1-\nu)r}[(1-2\nu)(\delta_{ij}r_{,k}+\delta_{jk}r_{,i}-\delta_{ik}r_{,j})+2r_{,i}r_{,j}r_{,k}]n_k(\mathbf{s}) \tag{A.2}$$

$$\begin{aligned} S_{ij} = & \frac{\mu}{2\pi(1-\nu)r^2}\Big\{2\frac{\partial r}{\partial n}[(1-2\nu)\delta_{ik}r_{,j}+\nu(\delta_{ij}r_{,k}+\delta_{jk}r_{,i})-4r_{,i}r_{,j}r_{,k}] \\ & +2\nu(n_ir_{,j}r_{,k}+n_kr_{,i}r_{,j})-(1-4\nu)\delta_{ik}n_j \\ & +(1-2\nu)(2n_jr_{,i}r_{,k}+\delta_{ij}n_k+\delta_{jk}n_i)\Big\}n_k(\mathbf{s}) \end{aligned} \tag{A.3}$$

For 3D displacement BIE:

$$U_{ij}(\mathbf{s},\mathbf{x}) = \frac{1}{16\pi\mu(1-\nu)r}\left[(3-4\nu)\delta_{ij}+r_{,i}r_{,j}\right], \tag{A.4}$$

$$T_{ij}(\mathbf{s},\mathbf{x}) = -\frac{1}{8\pi(1-\nu)r^2}\left\{\frac{\partial r}{\partial n}[(1-2\nu)\delta_{ij}+3r_{,i}r_{,j}]-(1-2\nu)(r_{,i}n_j-r_{,j}n_i)\right\}, \tag{A.5}$$

and for 3D traction BIE:

$$K_{ij} = \frac{1}{8\pi(1-\nu)r^2}[(1-2\nu)(\delta_{ij}r_{,k}+\delta_{jk}r_{,i}-\delta_{ik}r_{,j})+3r_{,i}r_{,j}r_{,k}]n_k(\mathbf{s}) \tag{A.6}$$

$$\begin{aligned} S_{ij} = \frac{\mu}{4\pi(1-\nu)r^3}\Big\{&3\frac{\partial r}{\partial n}[(1-2\nu)\delta_{ik}r_{,j}+\nu(\delta_{ij}r_{,k}+\delta_{jk}r_{,i})-5r_{,i}r_{,j}r_{,k}] \\ &+3\nu(n_ir_{,j}r_{,k}+n_kr_{,i}r_{,j})-(1-4\nu)\delta_{ik}n_j \\ &+(1-2\nu)(3n_jr_{,i}r_{,k}+\delta_{ij}n_k+\delta_{jk}n_i)\Big\}n_k(\mathbf{s}) \end{aligned} \tag{A.7}$$

Appendix B

Coefficients of the integrand expansions for SST

B.1 Expressions for 2D

Now we present the SST formula for the hyper-singular integral as follows. Expanding the components of distance between field and source points as Taylor series in parent space gives:

$$\begin{aligned} x_i - s_i &= \frac{\mathrm{d}x_i}{\mathrm{d}\hat{\xi}}\Big|_{\hat{\xi}=\hat{\xi}_s}(\hat{\xi}-\hat{\xi}_s) + \frac{\mathrm{d}^2x_i}{\mathrm{d}\hat{\xi}^2}\Big|_{\hat{\xi}=\hat{\xi}_s}\frac{(\hat{\xi}-\hat{\xi}_s)^2}{2} + \cdots \\ &:= A_i(\hat{\xi}-\hat{\xi}_s) + B_i(\hat{\xi}-\hat{\xi}_s)^2 + \cdots \\ &= A_i\delta + B_i\delta^2 + O(\delta^3) \end{aligned} \tag{B.1}$$

and

$$\begin{aligned} A &:= \left(\sum_{k=1}^{2} A_k^2\right)^{\frac{1}{2}} \\ C &:= \sum_{k=1}^{2} A_k B_k \end{aligned} \tag{B.2}$$

The first and second derivatives are:

$$\begin{aligned} \frac{\mathrm{d}x_i}{\mathrm{d}\xi} &= \frac{\mathrm{d}N_a}{\mathrm{d}\xi}x_i^a \\ \frac{\mathrm{d}^2x_i}{\mathrm{d}\xi^2} &= \frac{\mathrm{d}^2N_a}{\mathrm{d}\xi^2}x_i^a \\ \frac{\mathrm{d}x_i}{\mathrm{d}\hat{\xi}} &= \frac{\mathrm{d}x_i}{\mathrm{d}\xi}\frac{\mathrm{d}\xi}{\mathrm{d}\hat{\xi}} \\ \frac{\mathrm{d}^2x_i}{\mathrm{d}\hat{\xi}^2} &= \frac{\mathrm{d}^2x_i}{\mathrm{d}\xi^2}\left(\frac{\mathrm{d}\xi}{\mathrm{d}\hat{\xi}}\right)^2 \end{aligned} \tag{B.3}$$

The derivative $r_{,i}$ can be expressed as

$$\begin{aligned} r_{,i} = \frac{x_i - s_i}{r} &= \frac{A_i}{A} + \left(B_i A - A_i \frac{A_k B_k}{A^3} \right) \delta + O(\delta^2) \\ &:= d_{i0} + d_{i1}\delta + O(\delta^2) \end{aligned} \tag{B.4}$$

The term $1/r^2$ can be expressed as

$$\begin{aligned} \frac{1}{r^2} &= \frac{1}{A^2\delta^2} - \frac{2C}{A^4\delta} + O(1) \\ &:= \frac{S_{-2}}{\delta^2} + \frac{S_{-1}}{\delta} + O(1) \end{aligned} \tag{B.5}$$

The component of Jacobian from parametric space to physical space can be expressed as:

$$\begin{aligned} J_1(\xi) &= J_{10}(\xi_s) + J_{11}(\xi_s)(\xi - \xi_s) + O((\xi - \xi_s)^2) \\ &= J_{10}(\xi_s) + \frac{\mathrm{d}\xi}{\mathrm{d}\hat{\xi}}\Big|_{\xi=\xi_s} J_{11}(\xi_s)\delta + O(\delta^2) \\ J_2(\xi) &= J_{20}(\xi_s) + J_{21}(\xi_s)(\xi - \xi_s) + O((\xi - \xi_s)^2) \\ &= J_{10}(\xi_s) + \frac{\mathrm{d}\xi}{\mathrm{d}\hat{\xi}}\Big|_{\xi=\xi_s} J_{21}(\xi_s)\delta + O(\delta^2) \end{aligned} \tag{B.6}$$

i.e.,

$$J_k(\xi) := J_{k0}(\xi_s) + \frac{\mathrm{d}\xi}{\mathrm{d}\hat{\xi}}\Big|_{\xi=\xi_s} J_{k1}(\xi_s)\delta + O(\delta^2)$$

and we note that

$$\begin{aligned} J(\xi) &= \sqrt{J_1^2(\xi) + J_2^2(\xi)} = \sqrt{\left(\frac{\mathrm{d}y}{\mathrm{d}\xi}\right)^2 + \left(-\frac{\mathrm{d}x}{\mathrm{d}\xi}\right)^2} \\ \mathbf{n}(\xi) &= \left[\frac{\mathrm{d}y}{\mathrm{d}\xi}, -\frac{\mathrm{d}x}{\mathrm{d}\xi}\right] \end{aligned} \tag{B.7}$$

i.e.,

$$n_k(\xi) = J_k(\xi)/J(\xi)$$

And the NURBS basis function is also expanded as:

$$\begin{aligned} R_a(\hat{\xi}) &= R_a(\hat{\xi}_s) + \frac{\mathrm{d}R_a}{\mathrm{d}\xi}\Big|_{\xi=\xi_s}(\xi-\xi_s) + \cdots \\ &= R_a(\hat{\xi}_s) + \frac{\mathrm{d}R_a}{\mathrm{d}\xi}\Big|_{\xi=\xi_s}\frac{\mathrm{d}\xi}{\mathrm{d}\hat{\xi}}\Big|_{\hat{\xi}=\hat{\xi}_s}\delta + \cdots \\ &:= R_{a0}(\hat{\xi}_s) + R_{a1}(\hat{\xi}_s)\frac{\mathrm{d}\xi}{\mathrm{d}\hat{\xi}}\Big|_{\hat{\xi}=\hat{\xi}_s}\delta + O(\delta^2) \end{aligned} \tag{B.8}$$

The detail form of hyper-singular kernel S_{ij} is (plane strain)

$$\begin{aligned} S_{ij}(\mathbf{s},\mathbf{x}) = \frac{\mu}{2\pi(1-\nu)r^2}\Big\{ & 2\frac{\partial r}{\partial n}\left[(1-\nu)\delta_{ik}r_{,j} + \nu(\delta_{ij}r_{,k} + \delta_{jk}r_{,i} - 4r_{,i}r_{,j}r_{,k})\right] \\ & + 2\nu(n_i r_{,j}r_{,k} + n_k r_{,i}r_{,j}) - (1-4\nu)\delta_{ik}n_j \\ & + (1-2\nu)(2n_j r_{,i}r_{,k} + \delta_{ij}n_k + \delta_{jk}n_i)\Big\} n_k(\hat{\xi}_s) \\ := & \frac{1}{r^2}h(\hat{\xi}) \end{aligned} \tag{B.9}$$

Noting that $n_k(\xi) = J_k(\xi)/J(\xi)$, Use the above expansions to rewrite $h(\xi)$ as:

$$h(\hat{\xi}) = \frac{h_0(\hat{\xi}_s)}{J(\xi)} + \frac{h_1(\hat{\xi}_s)}{J(\xi)}\delta + O(\delta^2) \tag{B.10}$$

$$\begin{aligned} h_0(\hat{\xi}_s) = \Big(& 2\nu(J_{i0}d_{j0}d_{k0} + J_{k0}d_{i0}d_{j0}) + (1-2\nu)(2J_{j0}d_{i0}d_{k0} + \delta_{ij}J_{k0} + \delta_{jk}J_{i0}) \\ & + (1-4\nu)\delta_{ik}J_{j0}\Big)\frac{\mu}{2\pi(1-\nu)}n_k(\hat{\xi}_s) \end{aligned} \tag{B.11}$$

$$\begin{aligned} h_1(\hat{\xi}_s) = \Big[& 2(d_{l1}J_{l0} + d_{l0}J_{l1})\Big((1-2\nu)\delta_{ik}d_{j0} + \nu(\delta_{ij}d_{k0} + \delta_{jk}d_{i0}) - 4d_{i0}d_{j0}d_{k0}\Big) \\ & + 2\nu\Big(J_{i0}(d_{j1}d_{k0} + d_{j0}d_{k1}) + J_{i1}d_{j0}d_{k0} + J_{k0}(d_{i1}d_{j0} + d_{i0}d_{j1}) + J_{k1}d_{i0}d_{j0}\Big) \\ & + (1-2\nu)\Big(2(J_{j1}d_{i0}d_{k0} + J_{j0}(d_{i1}d_{k0} + d_{i0}d_{k1})) + \delta_{ij}J_{k1} + \delta_{jk}J_{i1}\Big) \\ & - (1-4\nu)\delta_{ik}J_{j1}\Big]\frac{\mu}{2\pi(1-\nu)}n_k(\hat{\xi}_s) \end{aligned} \tag{B.12}$$

Thus,

$$\begin{aligned} h(\hat{\xi})R_a(\hat{\xi})J(\hat{\xi}) =&\Big(h_0(\hat{\xi}_s)+h_1(\hat{\xi}_s)\delta+O(\delta^2)\Big)\Big(R_{a0}(\hat{\xi}_s)+\frac{\mathrm{d}\xi}{\mathrm{d}\hat{\xi}}\Big|_{\hat{\xi}=\hat{\xi}_s}R_{a1}(\hat{\xi}_s)\delta \\ &+O(\delta^2)\Big) \\ =&h_0R_{a0}+(h_1R_{a0}+h_0R_{a1}\frac{\mathrm{d}\xi}{\mathrm{d}\hat{\xi}}\Big|_{\hat{\xi}=\hat{\xi}_s})\delta+O(\delta^2) \end{aligned} \tag{B.13}$$

$$\begin{aligned} F(\hat{\xi}_s,\hat{\xi}) =& \frac{1}{r^2(\hat{\xi}_s,\hat{\xi})}h(\hat{\xi})R_a(\hat{\xi})J(\hat{\xi}) \\ =&\Big(\frac{S_{-2}}{\delta^2}+\frac{S_{-1}}{\delta}+O(1)\Big)\Big(h_0R_{a0}+(h_1R_{a0}+h_0R_{a1}\frac{\mathrm{d}\xi}{\mathrm{d}\hat{\xi}}\Big|_{\hat{\xi}=\hat{\xi}_s})\delta \\ &+O(\delta^2)\Big) \\ =&\frac{S_{-2}h_0R_{a0}}{\delta^2}+\frac{S_{-1}h_0R_{a0}+S_{-2}(h_1R_{a0}+h_0R_{a1}\frac{\mathrm{d}\xi}{\mathrm{d}\hat{\xi}}\Big|_{\hat{\xi}=\hat{\xi}_s})}{\delta}+O(1) \\ :=&\frac{F_{-2}}{\delta^2}+\frac{F_{-1}}{\delta}+O(1) \end{aligned} \tag{B.14}$$

B.2 Expressions for 3D

Supposing the parametric coordinate $\boldsymbol{\xi}(\xi,\eta)$ is in the knot interval $[\xi_1,\xi_2]\times[\eta_1,\eta_2]$, the mapping between parametric coordinate and parent coordinate is:

$$\begin{aligned} \xi &= \frac{1}{2}(\xi_2-\xi_1)\bar{\xi}+\frac{1}{2}(\xi_2+\xi_1), \\ \eta &= \frac{1}{2}(\eta_2-\eta_1)\bar{\eta}+\frac{1}{2}(\eta_2+\eta_1). \end{aligned} \tag{B.15}$$

And the Jacobian transformation for this would be:

$$\begin{aligned} \bar{J}_\xi &= \frac{\partial\xi}{\partial\bar{\xi}} = \frac{1}{2}(\xi_2-\xi_1), \\ \bar{J}_\eta &= \frac{\partial\eta}{\partial\bar{\eta}} = \frac{1}{2}(\eta_2-\eta_1), \\ \bar{J}(\boldsymbol{\xi}) &= \bar{J}_\xi\bar{J}_\eta. \end{aligned} \tag{B.16}$$

The Taylor expansion of $x_i - s_i$ with respect to the source point in the parent space would be:

$$x_i - s_i = \Big[\frac{\partial x_i}{\partial \bar{\xi}}\Big|_{\bar{\boldsymbol{\xi}}=\bar{\boldsymbol{\xi}}_s}(\bar{\xi}-\bar{\xi}_s) + \frac{\partial x_i}{\partial \bar{\eta}}\Big|_{\bar{\boldsymbol{\xi}}=\bar{\boldsymbol{\xi}}_s}(\bar{\eta}-\bar{\eta}_s)\Big] + \Big[\frac{\partial^2 x_i}{\partial \bar{\xi}^2}\Big|_{\bar{\boldsymbol{\xi}}=\bar{\boldsymbol{\xi}}_s}\frac{(\bar{\xi}-\bar{\xi}_s)^2}{2} + \frac{\partial^2 x_i}{\partial \bar{\xi}\partial \bar{\eta}}\Big|_{\bar{\boldsymbol{\xi}}=\bar{\boldsymbol{\xi}}_s}(\bar{\xi}-\bar{\xi}_s)(\bar{\eta}-\bar{\eta}_s) + \frac{\partial^2 x_i}{\partial \bar{\eta}^2}\Big|_{\bar{\boldsymbol{\xi}}=\bar{\boldsymbol{\xi}}_s}\frac{(\bar{\eta}-\bar{\eta}_s)^2}{2}\Big] + \cdots. \tag{B.17}$$

Note that:

$$\begin{aligned}
\frac{\partial x_i}{\partial \bar{\xi}} &= \frac{\partial x_i}{\partial \xi}\frac{\partial \xi}{\partial \bar{\xi}} = \frac{\partial x_i}{\partial \xi}\bar{J}_\xi,\\
\frac{\partial x_i}{\partial \bar{\eta}} &= \frac{\partial x_i}{\partial \eta}\frac{\partial \eta}{\partial \bar{\eta}} = \frac{\partial x_i}{\partial \eta}\bar{J}_\eta,\\
\frac{\partial^2 x_i}{\partial \bar{\xi}^2} &= \frac{\partial^2 x_i}{\partial \xi^2}\Big(\frac{\partial \xi}{\partial \bar{\xi}}\Big)^2 = \frac{\partial^2 x_i}{\partial \xi^2}\bar{J}_\xi^2,\\
\frac{\partial^2 x_i}{\partial \bar{\eta}^2} &= \frac{\partial^2 x_i}{\partial \eta^2}\Big(\frac{\partial \eta}{\partial \bar{\eta}}\Big)^2 = \frac{\partial^2 x_i}{\partial \eta^2}\bar{J}_\eta^2,\\
\frac{\partial^2 x_i}{\partial \bar{\xi}\partial \bar{\eta}} &= \frac{\partial^2 x_i}{\partial \xi \partial \eta}\frac{\partial \xi}{\partial \bar{\xi}}\frac{\partial \eta}{\partial \bar{\eta}} = \frac{\partial^2 x_i}{\partial \xi \partial \eta}\bar{J}_\xi \bar{J}_\eta
\end{aligned} \tag{B.18}$$

Now the polar coordinates $\boldsymbol{\rho}(\rho,\theta)$ centred at the source point are introduced in the parent space as in Figure 3.1, The parent domain is subdivided into four triangles for quadrature naturally. Each triangle is regarded as a degenerated square $[-1,1]\times[-1,1]$ with two points joint together. Supposing a point $\boldsymbol{\rho}(\rho,\theta)\in[0,\hat{\rho}(\theta)]\times[\theta_1,\theta_2]$ in the triangle, a linear mapping between the polar coordinates and the square coordinates system $\tilde{\boldsymbol{\xi}}(\tilde{\xi},\tilde{\eta})$ is performed as:

$$\begin{aligned}
\rho &= \frac{1}{2}(\tilde{\eta}+1)\hat{\rho}(\theta),\\
\theta &= \frac{1}{2}(\theta_2-\theta_1)\tilde{\xi} + \frac{1}{2}(\theta_2+\theta_1).
\end{aligned} \tag{B.19}$$

And the Jacobian transformation for this would be:

$$\begin{aligned}
\tilde{J}_\rho &= \frac{\partial \rho}{\partial \tilde{\eta}} = \frac{1}{2}\hat{\rho}(\theta),\\
\tilde{J}_\theta &= \frac{\partial \theta}{\partial \tilde{\xi}} = \frac{1}{2}(\theta_2-\theta_1),\\
\tilde{J}(\boldsymbol{\rho}) &= \tilde{J}_\rho \tilde{J}_\theta.
\end{aligned} \tag{B.20}$$

Equation (B.17) becomes:

$$\begin{aligned} x_i - s_i =& \rho\Big[\frac{\partial x_i}{\partial \bar{\xi}}\Big|_{\bar{\boldsymbol{\xi}}=\bar{\boldsymbol{\xi}}_s}\cos\theta + \frac{\partial x_i}{\partial \bar{\eta}}\Big|_{\bar{\boldsymbol{\xi}}=\bar{\boldsymbol{\xi}}_s}\sin\theta\Big] \\ &+ \rho^2\Big[\frac{\partial^2 x_i}{\partial \bar{\xi}^2}\Big|_{\bar{\boldsymbol{\xi}}=\bar{\boldsymbol{\xi}}_s}\frac{\cos^2\theta}{2} + \frac{\partial^2 x_i}{\partial \bar{\xi}\partial \bar{\eta}}\Big|_{\bar{\boldsymbol{\xi}}=\bar{\boldsymbol{\xi}}_s}\cos\theta\sin\theta + \frac{\partial^2 x_i}{\partial \bar{\eta}^2}\Big|_{\bar{\boldsymbol{\xi}}=\bar{\boldsymbol{\xi}}_s}\frac{\sin^2\theta}{2}\Big] \\ &+ O(\rho^3) \\ :=& \rho A_i(\theta) + \rho^2 B_i(\theta) + O(\rho^3). \end{aligned} \tag{B.21}$$

And we define:

$$\begin{aligned} A &:= \left(\sum_{k=1}^{3}[A_k(\theta)]^2\right)^{\frac{1}{2}}, \\ C &:= \sum_{k=1}^{3} A_k(\theta)B_k(\theta). \end{aligned} \tag{B.22}$$

The derivatives of $r = |\mathbf{x} - \mathbf{s}|$ are:

$$\begin{aligned} r_{,i} = \frac{x_i - s_i}{r} &= \frac{A_i}{A} + \left(\frac{B_i}{A} - A_i\frac{C}{A^3}\right)\rho + O(\rho^2) \\ &:= d_{i0} + d_{i1}\rho + O(\rho^2). \end{aligned} \tag{B.23}$$

The term $1/r^3$ is:

$$\begin{aligned} \frac{1}{r^3} &= \frac{1}{A^3\rho^3} - \frac{3C}{A^5\rho^2} + O(\frac{1}{\rho}) \\ &:= \frac{S_{-2}}{\rho^3} + \frac{S_{-1}}{\rho^2} + O(\frac{1}{\rho}). \end{aligned} \tag{B.24}$$

The NURBS basis function is also expanded as:

$$\begin{aligned} R_a(\boldsymbol{\xi}) &= R_a(\boldsymbol{\xi}_s) + \rho\Big[\frac{\partial R_a}{\partial \xi}\Big|_{\bar{\boldsymbol{\xi}}=\bar{\boldsymbol{\xi}}_s}\bar{J}_\xi\cos\theta + \frac{\partial R_a}{\partial \eta}\Big|_{\bar{\boldsymbol{\xi}}=\bar{\boldsymbol{\xi}}_s}\bar{J}_\eta\sin\theta\Big] + O(\rho^2) \\ &:= R_{a0} + R_{a1}(\theta)\rho + O(\rho^2). \end{aligned} \tag{B.25}$$

For the surface point $\boldsymbol{\xi}(\xi, \eta)$ in the knot interval $[\xi_1, \xi_2] \times [\eta_1, \eta_2]$, we define two tangential vectors along the ξ and η directions respectively as:

$$\begin{aligned} \mathbf{m}_1 &= \Big[\frac{\partial x}{\partial \xi}, \frac{\partial y}{\partial \xi}, \frac{\partial z}{\partial \xi}\Big], \\ \mathbf{m}_2 &= \Big[\frac{\partial x}{\partial \eta}, \frac{\partial y}{\partial \eta}, \frac{\partial z}{\partial \eta}\Big]. \end{aligned} \tag{B.26}$$

And we can get the normal vectors through:

$$\bar{\mathbf{n}} = \mathbf{m}_1 \times \mathbf{m}_2 = \Big[\frac{\partial y}{\partial \xi}\frac{\partial z}{\partial \eta} - \frac{\partial z}{\partial \xi}\frac{\partial y}{\partial \eta}, \frac{\partial z}{\partial \xi}\frac{\partial x}{\partial \eta} - \frac{\partial x}{\partial \xi}\frac{\partial z}{\partial \eta}, \frac{\partial x}{\partial \xi}\frac{\partial y}{\partial \eta} - \frac{\partial y}{\partial \xi}\frac{\partial x}{\partial \eta}\Big]. \quad \text{(B.27)}$$

The Jacobian for transformation from parametric space to physical space is the length of the normal vector $\bar{\mathbf{n}}$:

$$\begin{aligned} J(\boldsymbol{\xi}) &= \Big[\Big(\frac{\partial y}{\partial \xi}\frac{\partial z}{\partial \eta} - \frac{\partial z}{\partial \xi}\frac{\partial y}{\partial \eta}\Big)^2 + \Big(\frac{\partial z}{\partial \xi}\frac{\partial x}{\partial \eta} - \frac{\partial x}{\partial \xi}\frac{\partial z}{\partial \eta}\Big)^2 + \Big(\frac{\partial x}{\partial \xi}\frac{\partial y}{\partial \eta} - \frac{\partial y}{\partial \xi}\frac{\partial x}{\partial \eta}\Big)^2\Big]^{1/2} \\ &:= \Big[\sum_{k=1}^{3} J_k^2(\boldsymbol{\xi})\Big]^{1/2} \end{aligned} \quad \text{(B.28)}$$

The unit normal vector $\mathbf{n}$ could be expressed as:

$$\mathbf{n}(\boldsymbol{\xi}) = \frac{\bar{\mathbf{n}}}{J(\boldsymbol{\xi})}. \quad \text{(B.29)}$$

The component $J_i(\boldsymbol{\xi})$ can be expanded at the source point. For instance:

$$\begin{aligned} J_1(\boldsymbol{\xi}) &= J_1(\boldsymbol{\xi}_s) + \rho\Big[\frac{\partial J_1}{\partial \xi}\Big|_{\bar{\boldsymbol{\xi}}=\bar{\boldsymbol{\xi}}_s} \bar{J}_\xi \cos\theta + \frac{\partial J_1}{\partial \eta}\Big|_{\bar{\boldsymbol{\xi}}=\bar{\boldsymbol{\xi}}_s} \bar{J}_\eta \sin\theta\Big] + O(\rho^2) \\ &:= J_{10} + J_{11}(\theta)\rho + O(\rho^2), \\ \frac{\partial J_1}{\partial \xi} &= \frac{\partial}{\partial \xi}\Big(\frac{\partial y}{\partial \xi}\frac{\partial z}{\partial \eta} - \frac{\partial z}{\partial \xi}\frac{\partial y}{\partial \eta}\Big). \end{aligned} \quad \text{(B.30)}$$

So we can obtain $J_i(\boldsymbol{\xi})$ as:

$$J_i(\boldsymbol{\xi}) = J_{i0} + J_{i1}(\theta)\rho + O(\rho^2). \quad \text{(B.31)}$$

Combining with Equation (B.29), we arrive at:

$$n_i(\boldsymbol{\xi}) = \frac{1}{J(\boldsymbol{\xi})}[J_{i0} + J_{i1}(\theta)\rho + O(\rho^2)]. \quad \text{(B.32)}$$

Row, all the terms are prepared for the expansion of the integrand. Let's take a simple example:

$$I = \oint\!\!\!\!\!\!-_S \frac{r_{,i} n_i(\boldsymbol{\xi}) R_a(\boldsymbol{\xi})}{r^3} \mathrm{d}S. \quad \text{(B.33)}$$

After discretization,

$$I = \int_0^{2\pi} \int_0^{\hat{\rho}(\theta)} \frac{r_{,i} n_i R_a}{r^3} J(\boldsymbol{\xi}) \bar{J}(\boldsymbol{\xi}) \rho \mathrm{d}\rho \mathrm{d}\theta, \tag{B.34}$$

where $\bar{J}(\boldsymbol{\xi})$ is from parent to parametric space defined in Equation (B.16), $J(\boldsymbol{\xi})$ from parametric to physical space defined in Equation (B.28). $\hat{\rho}(\theta)$ is the upper bound of ρ and can be seen in Figure 3.1.

And substitute Equations (B.23)(B.24)(B.32)(B.25) into the discretization:

$$\begin{aligned} I = & \int_0^{2\pi} \int_0^{\hat{\rho}(\theta)} \Big[d_{i0} + d_{i1}\rho + O(\rho^2) \Big] \frac{1}{J(\boldsymbol{\xi})} \Big[J_{i0} + J_{i1}\rho + O(\rho^2) \Big] \Big[R_{a0} + R_{a1}\rho \\ & + O(\rho^2) \Big] \Big[\frac{S_{-2}}{\rho^3} + \frac{S_{-1}}{\rho^2} + O(\frac{1}{\rho}) \Big] J(\boldsymbol{\xi}) \bar{J}(\boldsymbol{\xi}) \rho \mathrm{d}\rho \mathrm{d}\theta \\ = & \int_0^{2\pi} \int_0^{\hat{\rho}(\theta)} \Big[d_{i0} J_{i0} R_{a0} + (d_{i1} J_{i0} R_{a0} + d_{i0} J_{i1} R_{a0} + d_{i0} J_{i0} R_{a1}) \rho \\ & + O(\rho^2) \Big] \Big[\frac{S_{-2}}{\rho^2} + \frac{S_{-1}}{\rho} + O(1) \Big] \frac{1}{\rho J(\boldsymbol{\xi})} J(\boldsymbol{\xi}) \bar{J}(\boldsymbol{\xi}) \rho \mathrm{d}\rho \mathrm{d}\theta \\ = & \int_0^{2\pi} \int_0^{\hat{\rho}(\theta)} \Big(\frac{I_{-2}}{\rho^2} + \frac{I_{-1}}{\rho} + O(1) \Big) \bar{J}(\boldsymbol{\xi}) \mathrm{d}\rho \mathrm{d}\theta, \end{aligned} \tag{B.35}$$

where I_{-2}, I_{-1} are only functions of θ:

$$\begin{aligned} I_{-2} &= S_{-2} d_{i0} J_{i0} R_{a0}, \\ I_{-1} &= S_{-1} d_{i0} J_{i0} R_{a0} + S_{-2} (d_{i1} J_{i0} R_{a0} + d_{i0} J_{i1} R_{a0} + d_{i0} J_{i0} R_{a1}). \end{aligned} \tag{B.36}$$

Subtracting the explicit singular part in the original integrand in Equation (B.34), the regular integral will be obtained:

$$I_{\text{reg}} = \int_0^{2\pi} \int_0^{\hat{\rho}(\theta)} \Big[\frac{r_{,i} n_i R_a}{r^3} J(\boldsymbol{\xi}) \rho - \frac{I_{-2}}{\rho^2} - \frac{I_{-1}}{\rho} \Big] \bar{J}(\boldsymbol{\xi}) \mathrm{d}\rho \mathrm{d}\theta, \tag{B.37}$$

This double integral can be evaluated using normal Gaussian rule. And the explicit part then will be added back and treated in a semi-analytical way. For the source point located in the singular element, a small circle is created to exclude the source point radius ε in physical space. When mapping the circle into the intrinsic polar coordinate, the circle will be distorted

generally. The polar coordinate ρ is represented with respect to ε as:

$$\rho := \alpha(\varepsilon, \theta) = \varepsilon\beta(\theta) + \varepsilon^2\gamma(\theta) + O(\varepsilon^3). \tag{B.38}$$

To evaluate the coefficients β and γ, the radius of the circle is given as the Taylor expansion in intrinsic polar coordinates as:

$$\varepsilon = \rho A(\theta) + \rho^2 \frac{C(\theta)}{A(\theta)} + O(\rho^3). \tag{B.39}$$

The reversion of this series is:

$$\rho = \alpha(\varepsilon, \theta) = \varepsilon\frac{1}{A} - \varepsilon^2\frac{C}{A^4} + O(\varepsilon^3). \tag{B.40}$$

Thus we get:

$$\begin{aligned} \beta &= \frac{1}{A}, \\ \gamma &= -\frac{C}{A^4}, \end{aligned} \tag{B.41}$$

which are only functions of θ. Then let's first look at the explicit strong singular part given in the limit form as:

$$\begin{aligned} &\lim_{\varepsilon\to 0}\int_0^{2\pi}\int_{\alpha(\varepsilon,\theta)}^{\hat{\rho}(\theta)} \frac{I_{-1}(\theta)}{\rho}\bar{J}(\boldsymbol{\xi})\mathrm{d}\rho\mathrm{d}\theta \\ &= \lim_{\varepsilon\to 0}\int_0^{2\pi}\int_{\alpha(\varepsilon,\theta)}^{\hat{\rho}(\theta)} \frac{I_{-1}(\theta)}{\rho}\bar{J}(\boldsymbol{\xi})\tilde{J}(\boldsymbol{\rho})\mathrm{d}\tilde{\eta}\mathrm{d}\tilde{\xi} \\ &= \lim_{\varepsilon\to 0}\int_0^{2\pi} I_{-1}(\theta)\bar{J}(\boldsymbol{\xi})\tilde{J}_\theta\Big[\int_{\alpha(\varepsilon,\theta)}^{\hat{\rho}(\theta)} \frac{1}{\rho}\tilde{J}_\rho\mathrm{d}\tilde{\eta}\Big]\mathrm{d}\bar{\xi} \\ &= \lim_{\varepsilon\to 0}\int_0^{2\pi} I_{-1}(\theta)\bar{J}(\boldsymbol{\xi})\tilde{J}_\theta\Big[\int_{\alpha(\varepsilon,\theta)}^{\hat{\rho}(\theta)} \frac{1}{\rho}\mathrm{d}\rho\Big]\mathrm{d}\tilde{\xi} \\ &= \lim_{\varepsilon\to 0}\int_0^{2\pi} I_{-1}(\theta)\bar{J}(\boldsymbol{\xi})\tilde{J}_\theta[\ln\hat{\rho}(\theta) - \ln\alpha(\varepsilon,\theta)]\mathrm{d}\tilde{\xi} \\ &= \int_0^{2\pi} I_{-1}(\theta)\bar{J}(\boldsymbol{\xi})\ln\hat{\rho}(\theta)\tilde{J}_\theta\mathrm{d}\tilde{\xi} - \lim_{\varepsilon\to 0}\int_0^{2\pi} I_{-1}(\theta)\bar{J}(\boldsymbol{\xi})\ln\alpha(\varepsilon,\theta)\tilde{J}_\theta\mathrm{d}\tilde{\xi} \\ &= \int_0^{2\pi} I_{-1}(\theta)\bar{J}(\boldsymbol{\xi})\ln\hat{\rho}(\theta)\tilde{J}_\theta\mathrm{d}\tilde{\xi} - \lim_{\varepsilon\to 0}\int_0^{2\pi} I_{-1}(\theta)\bar{J}(\boldsymbol{\xi})\ln\varepsilon\beta(\theta)\tilde{J}_\theta\mathrm{d}\tilde{\xi} \\ &= \int_0^{2\pi} I_{-1}(\theta)\bar{J}(\boldsymbol{\xi})\ln\frac{\hat{\rho}(\theta)}{\beta(\theta)}\tilde{J}_\theta\mathrm{d}\tilde{\xi} - \bar{J}(\boldsymbol{\xi})\ln\varepsilon\lim_{\varepsilon\to 0}\int_0^{2\pi} I_{-1}(\theta)\mathrm{d}\theta \\ &= \int_0^{2\pi} I_{-1}(\theta)\bar{J}(\boldsymbol{\xi})\ln\frac{\hat{\rho}(\theta)}{\beta(\theta)}\tilde{J}_\theta\mathrm{d}\tilde{\xi}, \end{aligned} \tag{B.42}$$

where $\tilde{J}(\boldsymbol{\rho})$ is from polar to square coordinates defined in Equation (B.20). Note that the last term is canceled since:

$$\int_0^{2\pi} I_{-1}(\theta)\mathrm{d}\theta = 0. \tag{B.43}$$

After integrating the singular term with respect to ρ analytically and with the use of Equations (B.38)(B.43), the explicit strong singular integrand is transferred as a regular one-dimensional integral and normal Gaussian rule then can be applied. Similar treatment applies to the explicit hyper-singular term. The full evaluation for Equation (B.34) is obtained:

$$I = I_{\text{reg}} + \int_0^{2\pi} I_{-1}(\theta)\bar{J}(\boldsymbol{\xi})\ln\frac{\hat{\rho}(\theta)}{\beta(\theta)}\tilde{J}_\theta \mathrm{d}\tilde{\xi} - \int_0^{2\pi} I_{-2}(\theta)\bar{J}(\boldsymbol{\xi})\Big[\frac{\gamma(\theta)}{\beta^2(\theta)} + \frac{1}{\hat{\rho}(\theta)}\Big]\tilde{J}_\theta \mathrm{d}\tilde{\xi} \tag{B.44}$$

Appendix C

Details for the SIF extraction

C.1 The relations of J_x and K

Once the J_1 and J_2 are evaluated properly, K_I and K_{II} can be found easily. Since

$$J_1 = \frac{K_I^2 + K_{II}^2}{E'} \tag{C.1a}$$

$$J_2 = -\frac{2K_I K_{II}}{E'} \tag{C.1b}$$

where $E' = E/(1-\nu^2)$ for plane strain condition. And K_I and K_{II} can be solved as [144]:

$$K_I = \pm\Big\{\frac{E'J_1}{2}\Big[1 \pm \Big(1 - \Big(\frac{J_2}{J_1}\Big)^2\Big)^{1/2}\Big]\Big\}^{1/2} \tag{C.2a}$$

$$K_{II} = \pm\Big\{\frac{E'J_1}{2}\Big[1 \mp \Big(1 - \Big(\frac{J_2}{J_1}\Big)^2\Big)^{1/2}\Big]\Big\}^{1/2} \tag{C.2b}$$

The signs of K_I and K_{II} correspond to the signs of crack opening displacement $[\![u_1]\!]$ and $[\![u_2]\!]$, respectively. If $[\![u_1]\!] > 0$, $K_I > 0$. The term in brace can be determined as :

$$\text{if} |[\![u_1]\!]| \geq |[\![u_2]\!]|, \text{take} + \tag{C.3a}$$

$$\text{if} |[\![u_1]\!]| < |[\![u_2]\!]|, \text{take} - \tag{C.3b}$$

C.2 SIF extraction from M integral

Combined with Equation C.1a, the following relationship can be obtained for the M integral,

$$M^{(1,2)} = \frac{2}{E'}(K_I^{(1)}K_I^{(2)} + K_{II}^{(1)}K_{II}^{(2)}) \tag{C.4}$$

For 3D case, the relation of J and K is:

$$J = G_I + G_{II} + G_{III} = \frac{1-\nu^2}{E}K_I^2 + \frac{1-\nu^2}{E}K_{II}^2 + \frac{1}{2\mu}K_{III}^2, \tag{C.5}$$

where G_i ($i = I, II, III$) are the energy release rates for the three modes of fracture. Then

$$M^{(1,2)} = \frac{2(1-\nu^2)}{E}(K_I^{(1)}K_I^{(2)} + K_{II}^{(1)}K_{II}^{(2)}) + \frac{1}{\mu}K_{III}^{(1)}K_{III}^{(2)}. \tag{C.6}$$

Let state 2 be the pure mode I asymptotic fields with $K_I^{(2)} = 1$, $K_{II}^{(2)} = 0$ (and for 3D $K_{III} = 0$) and K_I in real state 1 can be found as

$$K_I^{(1)} = \frac{2}{E'}M^{(1,\text{ mode } I)} \tag{C.7}$$

The K_{II} (and K_{III} in 3D case) can be given in a similar fashion.

C.3 The auxiliary fields for M integral

The auxiliary stress field $\sigma_{ij}^{(2)}$ and displacement field $u_j^{(2)}$ are given as:

$$
\begin{aligned}
\sigma_{xx}(r,\theta) &= \frac{K_I^{(2)}}{\sqrt{2\pi r}}\cos\frac{\theta}{2}\Big(1-\sin\frac{\theta}{2}\sin\frac{3\theta}{2}\Big) - \frac{K_{II}^{(2)}}{\sqrt{2\pi r}}\sin\frac{\theta}{2}\Big(2+\cos\frac{\theta}{2}\cos\frac{3\theta}{2}\Big)\\
\sigma_{yy}(r,\theta) &= \frac{K_I^{(2)}}{\sqrt{2\pi r}}\cos\frac{\theta}{2}\Big(1+\sin\frac{\theta}{2}\sin\frac{3\theta}{2}\Big) + \frac{K_{II}^{(2)}}{\sqrt{2\pi r}}\sin\frac{\theta}{2}\cos\frac{\theta}{2}\cos\frac{3\theta}{2}\\
\tau_{xy}(r,\theta) &= \frac{K_I^{(2)}}{\sqrt{2\pi r}}\sin\frac{\theta}{2}\cos\frac{\theta}{2}\cos\frac{3\theta}{2} + \frac{K_{II}^{(2)}}{\sqrt{2\pi r}}\cos\frac{\theta}{2}\Big(1-\sin\frac{\theta}{2}\sin\frac{3\theta}{2}\Big)\\
u_x(r,\theta) &= \frac{K_I}{2\mu}\sqrt{\frac{r}{2\pi}}\cos\frac{\theta}{2}\left(\kappa-1+2\sin^2\frac{\theta}{2}\right)\\
&\quad + \frac{(1+\nu)K_{II}}{E}\sqrt{\frac{r}{2\pi}}\sin\frac{\theta}{2}\left(\kappa+1+2\cos^2\frac{\theta}{2}\right)\\
u_y(r,\theta) &= \frac{K_I}{2\mu}\sqrt{\frac{r}{2\pi}}\sin\frac{\theta}{2}\left(\kappa+1-2\cos^2\frac{\theta}{2}\right)\\
&\quad + \frac{(1+\nu)K_{II}}{E}\sqrt{\frac{r}{2\pi}}\cos\frac{\theta}{2}\left(1-\kappa+2\sin^2\frac{\theta}{2}\right)
\end{aligned}
\tag{C.8}
$$

where (r,θ) are the crack tip polar coordinates and

$$
\mu = \frac{E}{2(1+\nu)} \tag{C.9}
$$

$$
\kappa = \begin{cases} 3-4\nu, & \text{Plane strain} \\ (1-\nu)/(3+\nu), & \text{Plane stress} \end{cases} \tag{C.10}
$$

And for 3D, the auxiliary stress field $\sigma_{ij}^{(2)}$ and displacement field $u_j^{(2)}$ are given as:

$$
\begin{aligned}
\sigma_{xx} &= \frac{K_I^{(2)}}{\sqrt{2\pi r}}\cos\frac{\theta}{2}\Big(1-\sin\frac{\theta}{2}\sin\frac{3\theta}{2}\Big) - \frac{K_{II}^{(2)}}{\sqrt{2\pi r}}\sin\frac{\theta}{2}\Big(2+\cos\frac{\theta}{2}\cos\frac{3\theta}{2}\Big)\\
\sigma_{yy} &= \frac{K_I^{(2)}}{\sqrt{2\pi r}}\cos\frac{\theta}{2}\Big(1+\sin\frac{\theta}{2}\sin\frac{3\theta}{2}\Big) + \frac{K_{II}^{(2)}}{\sqrt{2\pi r}}\sin\frac{\theta}{2}\cos\frac{\theta}{2}\cos\frac{3\theta}{2},\\
\tau_{xy} &= \frac{K_I^{(2)}}{\sqrt{2\pi r}}\sin\frac{\theta}{2}\cos\frac{\theta}{2}\cos\frac{3\theta}{2} + \frac{K_{II}^{(2)}}{\sqrt{2\pi r}}\cos\frac{\theta}{2}\Big(1-\sin\frac{\theta}{2}\sin\frac{3\theta}{2}\Big),\\
\tau_{yz} &= \frac{K_{III}^{(2)}}{\sqrt{2\pi r}}\cos\frac{\theta}{2},\\
\tau_{zx} &= -\frac{K_{III}^{(2)}}{\sqrt{2\pi r}}\sin\frac{\theta}{2},\\
\tau_{zz} &= \nu(\sigma_{xx}+\sigma_{yy}),\\
u_x &= \frac{K_I}{2\mu}\sqrt{\frac{r}{2\pi}}\cos\frac{\theta}{2}\left(\kappa-1+2\sin^2\frac{\theta}{2}\right)\\
&\quad + \frac{(1+\nu)K_{II}}{E}\sqrt{\frac{r}{2\pi}}\sin\frac{\theta}{2}\left(\kappa+1+2\cos^2\frac{\theta}{2}\right),\\
u_y &= \frac{K_I}{2\mu}\sqrt{\frac{r}{2\pi}}\sin\frac{\theta}{2}\left(\kappa+1-2\cos^2\frac{\theta}{2}\right)\\
&\quad + \frac{(1+\nu)K_{II}}{E}\sqrt{\frac{r}{2\pi}}\cos\frac{\theta}{2}\left(1-\kappa+2\sin^2\frac{\theta}{2}\right),\\
u_z &= \frac{2K_{III}}{\mu}\sqrt{\frac{r}{2\pi}}\sin\frac{\theta}{2}.
\end{aligned}
\tag{C.11}
$$

The auxiliary strain field can be obtained by differentiating u_j with respect to the physical coordinate.

Appendix D

Theory of double-interpolation XFEM

D.1 2D approximation by double interpolation

As illustrated in Figure D.1, $\mathbf{x} = (x, y)$ denotes the point of interest in triangle IJK. Analogous to the derivation for the 1D formulation, the 2D double-interpolation approximation in a mesh of triangular element can be cosntructed as follows:

$$\mathbf{u}^h(\mathbf{x}) = \sum_{L \in \hat{\mathscr{N}}} \hat{N}_L(\mathbf{x}) \mathbf{u}^L, \tag{D.1}$$

$$\begin{aligned} \hat{N}_L(\mathbf{x}) =& \phi_I(\mathbf{x}) N_L(\mathbf{x}_I) + \psi_I(\mathbf{x}) \bar{N}_{L,x}(\mathbf{x}_I) + \varphi_I(\mathbf{x}) \bar{N}_{L,y}(\mathbf{x}_I) + \\ & \phi_J(\mathbf{x}) N_L(\mathbf{x}_J) + \psi_J(\mathbf{x}) \bar{N}_{L,x}(\mathbf{x}_J) + \varphi_J(\mathbf{x}) \bar{N}_{L,y}(\mathbf{x}_J) + \\ & \phi_K(\mathbf{x}) N_L(\mathbf{x}_K) + \psi_K(\mathbf{x}) \bar{N}_{L,x}(\mathbf{x}_K) + \varphi_K(\mathbf{x}) \bar{N}_{L,y}(\mathbf{x}_K), \end{aligned} \tag{D.2}$$

where $\mathbf{u}^L$ is the nodal displacement vector. In the following discussion the evaluation of the average derivative of the shape function at node $\mathbf{x}_I$ is considered. The average derivative of the shape function at node $\mathbf{x}_I$ can be written as:

$$\bar{N}_{L,x}(\mathbf{x}_I) = \sum_{e_{i,I} \in \Lambda_I} \omega_{e_{i,I}} N^{e_i}_{L,x}(\mathbf{x}_I), \tag{D.3a}$$

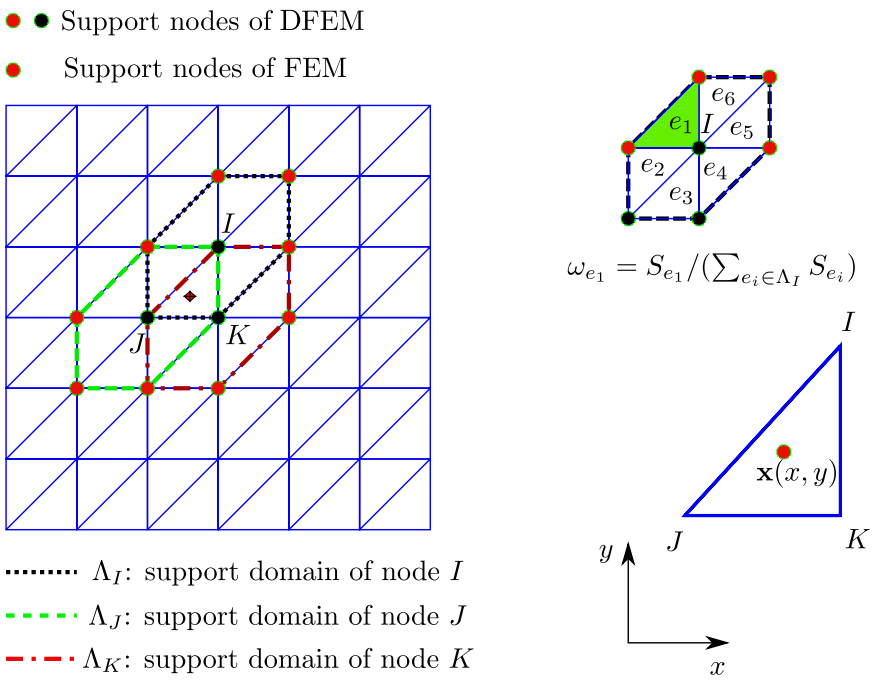

FIGURE D.1: Illustration for the support domain of DFEM

$$\bar{N}_{L,y}(\mathbf{x}_I) = \sum_{e_{i,I} \in \Lambda_I} \omega_{e_{i,I}} N^{e_i}_{L,y}(\mathbf{x}_I), \tag{D.3b}$$

where $\omega_{e_{i,I}}$ is the weight of element e_i in Λ_I and is computed by:

$$\omega_{e_{i,I}} = meas(e_i) / \sum_{e_i \in \Lambda_I} meas(e_i). \tag{D.4}$$

Here $meas(\cdot)$ denotes the area of a triangular element. An example of how to evaluate the weight of an element is presented in Figure D.1. ϕ_I, ψ_I and φ_I form the polynomial basis associated with $\mathbf{x}_I$, which satisfies the following interpolating conditions:

$$\begin{aligned} &\phi_I(\mathbf{x}_L) = \delta_{IL}, \quad \phi_{I,x}(\mathbf{x}_L) = 0 \quad , \quad \phi_{I,y}(\mathbf{x}_L) = 0, \\ &\psi_I(\mathbf{x}_L) = 0 \quad , \quad \psi_{I,x}(\mathbf{x}_L) = \delta_{IL}, \quad \psi_{I,y}(\mathbf{x}_L) = 0, \\ &\varphi_I(\mathbf{x}_L) = 0 \quad , \quad \varphi_{I,x}(\mathbf{x}_L) = 0 \quad , \quad \varphi_{I,y}(\mathbf{x}_L) = \delta_{IL}. \end{aligned} \tag{D.5}$$

And these polynomial basis functions are given by:

$$\begin{aligned} \phi_I(\mathbf{x}) =& L_I(\mathbf{x}) + (L_I(\mathbf{x}))^2 L_J(\mathbf{x}) + (L_I(\mathbf{x}))^2 L_K(\mathbf{x}) \\ &- L_I(\mathbf{x}) (L_J(\mathbf{x}))^2 - L_I(\mathbf{x}) (L_K(\mathbf{x}))^2 , \end{aligned} \tag{D.6a}$$

$$\begin{aligned}\psi_I(\mathbf{x}) = &- c_J \left(L_K(\mathbf{x}) \left(L_I(\mathbf{x})\right)^2 + \frac{1}{2} L_I(\mathbf{x}) L_J(\mathbf{x}) L_K(\mathbf{x}) \right) + \\ &c_K \left(\left(L_I(\mathbf{x})\right)^2 L_J(\mathbf{x}) + \frac{1}{2} L_I(\mathbf{x}) L_J(\mathbf{x}) L_K(\mathbf{x}) \right),\end{aligned} \tag{D.6b}$$

$$\begin{aligned}\varphi_I(\mathbf{x}) = &b_J \left(L_K(\mathbf{x}) \left(L_I(\mathbf{x})\right)^2 + \frac{1}{2} L_I(\mathbf{x}) L_J(\mathbf{x}) L_K(\mathbf{x}) \right) - \\ &b_K \left(\left(L_I(\mathbf{x})\right)^2 L_J(\mathbf{x}) + \frac{1}{2} L_I(\mathbf{x}) L_J(\mathbf{x}) L_K(\mathbf{x}) \right).\end{aligned} \tag{D.6c}$$

Note that the polynomial basis functions $\phi_J, \psi_J, \varphi_J, \phi_K, \psi_K$ and φ_K can be obtained by the above definitions via cyclic permutation of indices I, J and K. In the above equations, L_I, L_J and L_K are the area coordinates of the point of interest x in triangle IJK. For the point of interest x in Figure D.1, the L_I, a_I, b_I and c_I are presented as follows:

$$L_I(\mathbf{x}) = \frac{1}{2\bigtriangleup}(a_I + b_I x + c_I y), \tag{D.7a}$$

$$a_I = x_J y_K - x_K y_J, \tag{D.7b}$$

$$b_I = y_J - y_K, \tag{D.7c}$$

$$c_I = x_K - x_J, \tag{D.7d}$$

where $\bigtriangleup$ is the area of triangle IJK. Further, L_J, L_K, a_J,b_J, b_K, a_I, c_J and c_K can be obtained using the above definitions via cyclic permutations of indices I, J and K.

When the point of interest lies on one of the edges, for example on edge IJ, the basis functions will boil down to 1D basis functions and will be consistent with the 1D form presented in the preceding section.

The DFEM shape functions posess the properties such as linear completeness, partition of unity and Kronecker delta property. In addition, the 2D DFEM possesses C^1 continuity at the nodes and C^0 continuity on edges. Compared to 3-noded triangular elements, the DFEM basis functions can achieve a higher-order convergence rate without the introduction of additional nodes, which will be seen the numerical examples in the next section. However, this attractive feature comes with the price of an increased bandwidth as the neighboring nodes are used to obtain the nodal gradients

necessary for the second interpolation. The details of such computational costs will be discussed in the section devoted to numerical examples.

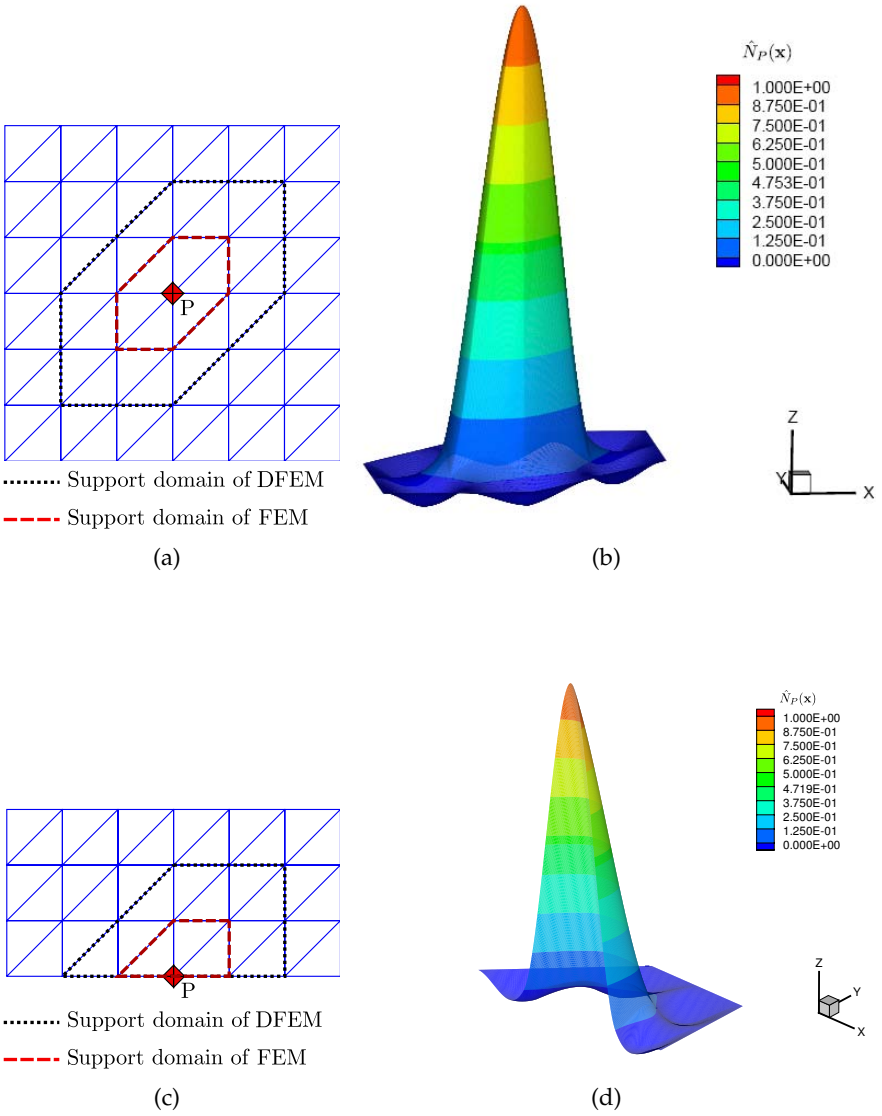

FIGURE D.2: The shape functions of DFEM in 2D

D.2 Modification of the nodal gradients

When C^0 continuity of the primal field at a node is needed, for instance on the nodes along a material interface, it is useful to modify the calculation of the average nodal gradient as discussed below. The calculation of the nodal gradient can be performed as follows:

$$\bar{N}_{L,x}(\mathbf{x}_I) = N^e_{L,x}(\mathbf{x}_I). \tag{D.8}$$

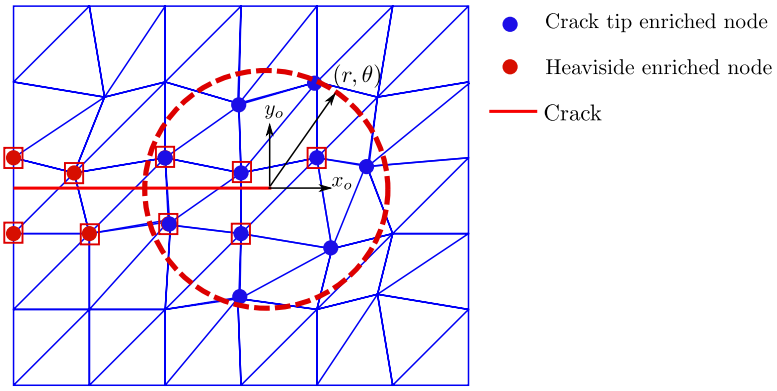

FIGURE D.3: Nodal enrichment in XDFEM; the nodes encircled by red box are degenerated to C^0, see section 2.3

The right hand side is the derivative of N_L computed in element e, in which the point of interest $\mathbf{x}$ is located. This is easily done in the implementation by replacing the average derivative with the derivative in the element of interest. It can be observed that nodes at the endpoint of a 1D bar automatically satisfy the above equation. All the Heaviside and topological enriched nodes in XFEM (the nodes circled by red boxes in Figure D.3 and Figure D.4) have been relaxed to C^0 as well due to the fact that during the calculation of average gradients in Equation (D.3), the contribution from split elements cannot be computed directly as from continuous elements in an area weighted manner (Equation (D.4)) due to the discontinuity. This is similar to difficulties encountered in smoothing enriched approximations [139][31].

D.3 The enriched 2D double-interpolation approximation

The crack can be described in XFEM by enriching the standard displacement approximation as follows:

$$\mathbf{u}^h(\mathbf{x}) = \sum_{I \in \mathcal{N}_I} \hat{N}_I(\mathbf{x})\mathbf{u}^I + \sum_{J \in \mathcal{N}_J} \hat{N}_J(\mathbf{x})H(\mathbf{x})\mathbf{a}^J + \sum_{K \in \mathcal{N}_K} \hat{N}_K(\mathbf{x}) \sum_{\alpha=1}^{4} f_\alpha(\mathbf{x})\mathbf{b}^{K\alpha}, \tag{D.9}$$

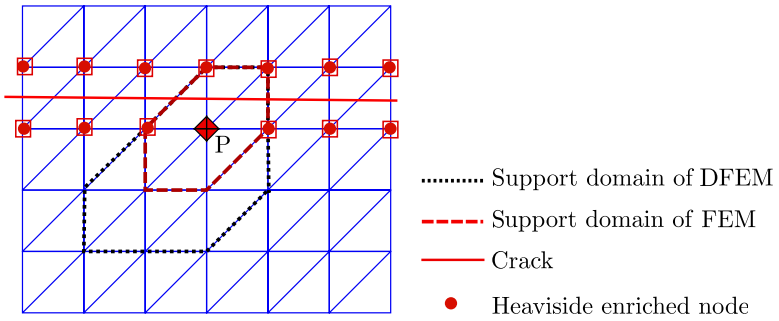

FIGURE D.4: The support domain of enriched DFEM; the nodes encircled by red box are degenerated to C^0, see section 2.3

where $\mathbf{u}^I$ are the regular DOFs, $\mathbf{a}^J$ are the additional Heaviside enriched DOFs, and $\mathbf{b}^{K\alpha}$ are the additional crack tip enriched DOFs. $\mathscr{N}_I$,$\mathscr{N}_J$ and $\mathscr{N}_K$ are the collections of regular non-enriched nodes, Heaviside enriched nodes and crack tip enriched nodes, respectively. $H(\cdot)$ is the Heaviside function. The crack tip enrichment functions are defined as:

$$\{f_\alpha(r,\theta), \alpha = 1,4\} = \left\{\sqrt{r}\sin\frac{\theta}{2}, \sqrt{r}\cos\frac{\theta}{2}, \sqrt{r}\sin\frac{\theta}{2}\sin\theta, \sqrt{r}\cos\frac{\theta}{2}\sin\theta\right\}, \tag{D.10}$$

where (r,θ) are the polar coordinates of the crack tip (Figure D.3). Figure D.5 compares the Heaviside enriched shape functions obtained with XFEM and XDFEM which are defined in Figure D.4.

D.4 Weak form and discretized formulations

For an elastic body as in Figure D.6 defined by Hooke's tensor $\mathbf{C}$ and undergoing small strains and small displacements, the equilibrium equations and boundary conditions for the Cauchy stress $\boldsymbol{\sigma}$ and the displacement field $\mathbf{u}$ write:

$$\begin{aligned} \nabla\cdot\boldsymbol{\sigma} &= \mathbf{0} \quad \text{in} \quad \Omega, \\ \boldsymbol{\sigma}\cdot\mathbf{n} &= \bar{\mathbf{t}} \quad \text{on} \quad \Gamma_t, \\ \mathbf{u} &= \bar{\mathbf{u}} \quad \text{on} \quad \Gamma_u. \end{aligned} \tag{D.11}$$

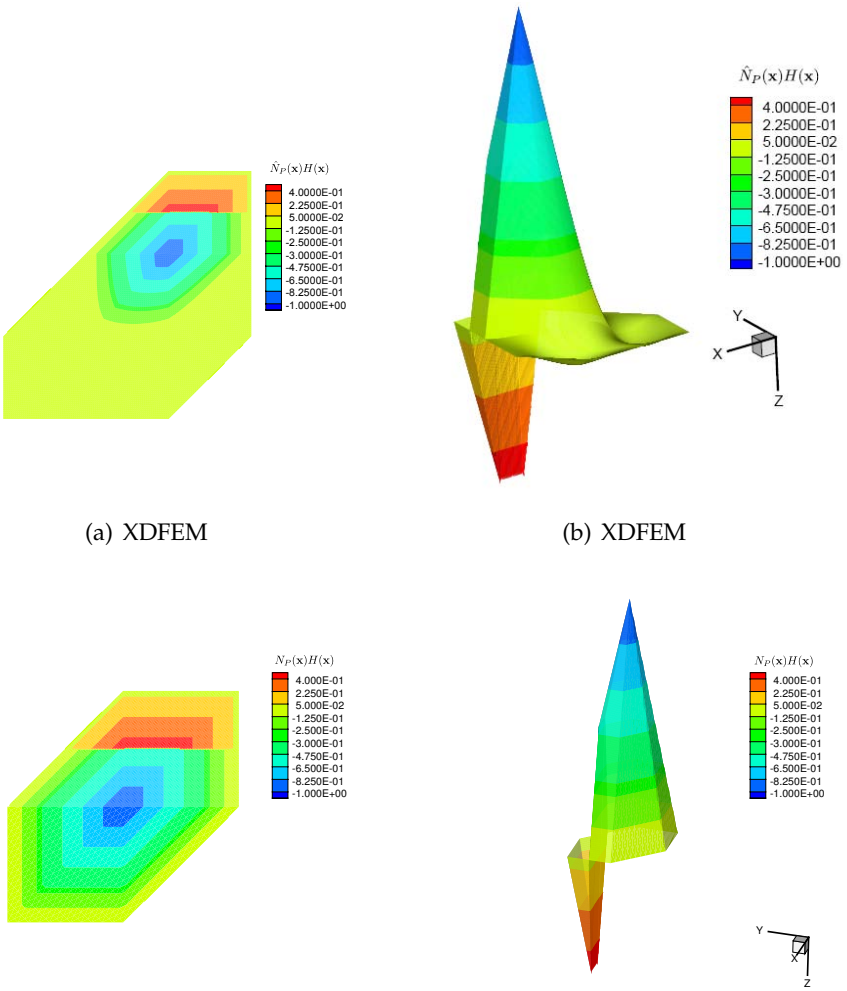

(a) XDFEM (b) XDFEM

(c) XFEM (d) XFEM

FIGURE D.5: Contour plot of Heaviside enriched shape functions

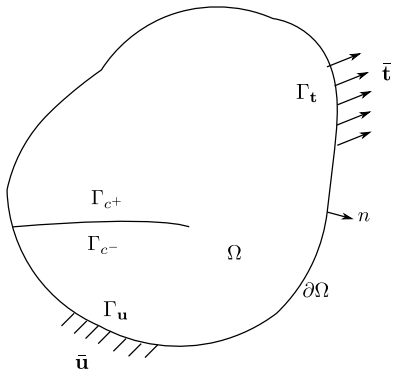

FIGURE D.6: Elastic body with a crack, $\partial\Omega = \Gamma_{\mathbf{u}} \cup \Gamma_{\mathbf{t}}, \Gamma_{\mathbf{u}} \cap \Gamma_{\mathbf{t}} = \emptyset$

Here $\bar{\mathbf{t}}$ is the traction imposed on boundary Γ_t. Further, assuming traction free crack faces:

$$\boldsymbol{\sigma} \cdot \mathbf{n} = \mathbf{0} \qquad \text{on} \quad \Gamma_{c^+} \text{ and } \Gamma_{c^-}, \tag{D.12}$$

where $\Gamma_{c^+}, \Gamma_{c^-}$ are the upper and lower crack surfaces respectively. The strain-displacement relation and the constitutive law are respectively as:

$$\boldsymbol{\epsilon} = \frac{1}{2}\left(\nabla + \nabla^{\mathrm{T}}\right) \otimes \mathbf{u}, \tag{D.13a}$$

$$\boldsymbol{\sigma} = \mathbf{C} : \boldsymbol{\epsilon}. \tag{D.13b}$$

Using a Bubnov-Galerkin weighted residual formulation based on Lagrange test and trial spaces, substituting the trial and test functions into the weak form of Equation (D.11), and using the arbitrariness of nodal variations, the discretized equations can be written:

$$\mathbf{K}\mathbf{u} = \mathbf{f}, \tag{D.14}$$

where $\mathbf{u}$ is the nodal vector of the unknown displacements and $\mathbf{K}$ is the stiffness matrix. The elemental form of $\mathbf{K}$ for element e is given by:

$$\mathbf{K}_{IJ}^{e} = \begin{bmatrix} \mathbf{K}_{IJ}^{uu} & \mathbf{K}_{IJ}^{ua} & \mathbf{K}_{IJ}^{ub} \\ \mathbf{K}_{IJ}^{au} & \mathbf{K}_{IJ}^{aa} & \mathbf{K}_{IJ}^{ab} \\ \mathbf{K}_{IJ}^{bu} & \mathbf{K}_{IJ}^{ba} & \mathbf{K}_{IJ}^{bb} \end{bmatrix}. \tag{D.15}$$

The external force vector $\mathbf{f}$ is defined as

$$\mathbf{f}_I = \{\mathbf{f}_I^u \quad \mathbf{f}_I^a \quad \mathbf{f}_I^{b^1} \quad \mathbf{f}_I^{b^2} \quad \mathbf{f}_I^{b^3} \quad \mathbf{f}_I^{b^4}\}. \tag{D.16}$$

The submatrices and vectors in Equations (D.15) and (D.16) are:

$$\mathbf{K}_{IJ}^{rs} = \int_{\Omega^e} (\mathbf{B}_I^r)^T \mathbf{C} \mathbf{B}_J^s \mathrm{d}\Omega \qquad (r, s = u, a, b), \tag{D.17a}$$

$$\mathbf{f}_I^u = \int_{\partial\Omega_t^h \cap \partial\Omega^e} \hat{N}_I \bar{\mathbf{t}} \mathrm{d}\Gamma, \tag{D.17b}$$

$$\mathbf{f}_I^a = \int_{\partial\Omega_t^h \cap \partial\Omega^e} \hat{N}_I H \bar{\mathbf{t}} \mathrm{d}\Gamma, \tag{D.17c}$$

$$\mathbf{f}_I^{b^\alpha} = \int_{\partial\Omega_t^h \cap \partial\Omega^e} \hat{N}_I f_\alpha \bar{\mathbf{t}} \mathrm{d}\Gamma \qquad (\alpha = 1, 2, 3, 4). \tag{D.17d}$$

In Equation (D.17a), $\mathbf{B}_I^u, \mathbf{B}_I^a$ and $\mathbf{B}_I^{b^\alpha}$ are given by

$$\mathbf{B}_I^u = \begin{bmatrix} \hat{N}_{I,x} & 0 \\ 0 & \hat{N}_{I,y} \\ \hat{N}_{I,y} & \hat{N}_{I,x} \end{bmatrix}, \tag{D.18a}$$

$$\mathbf{B}_I^a = \begin{bmatrix} \left(\hat{N}_I(H - H_I)\right)_{,x} & 0 \\ 0 & \left(\hat{N}_I(H - H_I)\right)_{,y} \\ \left(\hat{N}_I(H - H_I)\right)_{,y} & \left(\hat{N}_I(H - H_I)_{,x}\right. \end{bmatrix}, \tag{D.18b}$$

$$\mathbf{B}_I^b = \begin{bmatrix} \mathbf{B}_I^{b^1} & \mathbf{B}_I^{b^2} & \mathbf{B}_I^{b^3} & \mathbf{B}_I^{b^4} \end{bmatrix}, \tag{D.18c}$$

$$\mathbf{B}_I^{b^\alpha} = \begin{bmatrix} \left(\hat{N}_I(f_\alpha - f_{\alpha I})\right)_{,x} & 0 \\ 0 & \left(\hat{N}_I(f_\alpha - f_{\alpha I})\right)_{,y} \\ \left(\hat{N}_I(f_\alpha - f_{\alpha I})\right)_{,y} & \left(\hat{N}_I(f_\alpha - f_{\alpha I})\right)_{,x} \end{bmatrix} \quad (\alpha = 1 - 4). \tag{D.18d}$$

In order to obtain the nodal displacements in a more straightforward manner, the shifted-basis is adopted in the above equations. More details regarding XFEM implementation can be found in [137].

The strategies of numerical integration for XDFEM is similar to standard XFEM. A simple subdivision for Heaviside enriched elements and tip enriched elements is performed for quadrature as in Figure D.7. Due to the introduction of higher-order polynomials in the basis functions of XDFEM, 4 Gauss points are adopted for each regular element whilst only 1 Gauss point in standard XFEM. And the Gauss quadrature is outlined briefly as

- regular elements: 1 Gauss point in XFEM and 4 Gauss points in XDFEM;
- Heaviside enriched elements: 1 Gauss point for each sub-cell in XFEM and 4 Gauss points for each sub-cell in XDFEM;

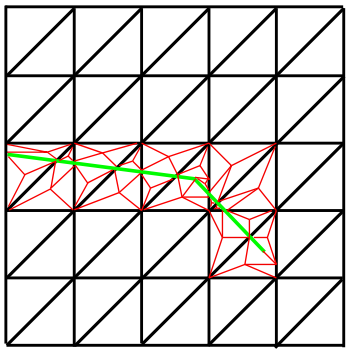

FIGURE D.7: Elements subdivision for quadrature in XFEM and XDFEM

- Tip blending elements: 7 Gauss points for each element in both XFEM and XDFEM;
- Tip enriched elements: 16 Gauss points for each sub-cell in both XFEM and XDFEM;

Bibliography

[1] Zdenek P Bazant and Milan Jirásek. Nonlocal integral formulations of plasticity and damage: survey of progress. *Journal of Engineering Mechanics*, 128(11):1119–1149, 2002.

[2] Zdenek P Bazant and Feng-Bao Lin. Nonlocal smeared cracking model for concrete fracture. *Journal of Structural Engineering*, 114(11):2493–2510, 1988.

[3] R de Borst, A Benallal, and O. M Heeres. A Gradient-Enhanced Damage Approach to Fracture. *Le Journal de Physique IV*, 06(C6):C6–491–C6–502, oct 1996.

[4] N Moës, C Stolz, P E Bernard, and N Chevaugeon. A level set based model for damage growth: The thick level set approach. *International Journal for Numerical Methods in Engineering*, 86(3):358–380, apr 2011.

[5] N Moës, J Dolbow, and T Belytschko. A finite element method for crack growth without remeshing. *International Journal for Numerical Methods in Engineering*, 46(1):131–150, 1999.

[6] S Bordas and B Moran. Enriched finite elements and level sets for damage tolerance assessment of complex structures. *Engineering Fracture Mechanics*, 73(9):1176–1201, 2006.

[7] X P Xu and A Needleman. Numerical simulations of fast crack growth in brittle solids. *Journal of the Mechanics and Physics of Solids*, 42(9):1397–1434, sep 1994.

[8] C J J Remmers, de R Borst, and A Needleman. A cohesive segments method for the simulation of crack growth. *Computational Mechanics*, 31(1):69–77, 2003.

[9] N Moës and T Belytschko. Extended finite element method for cohesive crack growth. *Engineering Fracture Mechanics*, 69(7):813–833, may 2002.

[10] J F Unger, S Eckardt, and C Könke. Modelling of cohesive crack growth in concrete structures with the extended finite element method. *Computer Methods in Applied Mechanics and Engineering*, 196(41-44):4087–4100, sep 2007.

[11] G Ferté, P Massin, and N Moës. 3D crack propagation with cohesive elements in the extended finite element method. *Computer Methods in Applied Mechanics and Engineering*, 300:347–374, mar 2016.

[12] G A Francfort and J J Marigo. Revisiting brittle fracture as an energy minimization problem. *Journal of the Mechanics and Physics of Solids*, 46(8):1319–1342, aug 1998.

[13] P Dumstorff and G Meschke. Crack propagation criteria in the framework of X-FEM-based structural analyses. *International Journal for Numerical and Analytical Methods in Geomechanics*, 31(2):239–259, feb 2007.

[14] G Meschke and P Dumstorff. Energy-based modeling of cohesive and cohesionless cracks via X-FEM. *Computer Methods in Applied Mechanics and Engineering*, 196(21-24):2338–2357, apr 2007.

[15] B R Davis, P A Wawrzynek, and A R Ingraffea. 3-D simulation of arbitrary crack growth using an energy-based formulation – Part I: Planar growth. *Engineering Fracture Mechanics*, 115:204–220, jan 2014.

[16] B R Davis, P A Wawrzynek, B J Carter, and A R Ingraffea. 3-D simulation of arbitrary crack growth using an energy-based formulation – Part II: Non-planar growth. *Engineering Fracture Mechanics*, 154:111–127, mar 2016.

[17] C Miehe, M Hofacker, and F Welschinger. A phase field model for rate-independent crack propagation: Robust algorithmic implementation based on operator splits. *Computer Methods in Applied Mechanics and Engineering*, 199(45-48):2765–2778, nov 2010.

[18] F Amiri, D Millán, M Arroyo, M Silani, and T Rabczuk. Fourth order phase-field model for local max-ent approximants applied to crack propagation. *Computer Methods in Applied Mechanics and Engineering*, feb 2016.

[19] M J Borden, Thomas J R Hughes, Chad M Landis, and C V Verhoosel. A higher-order phase-field model for brittle fracture: Formulation and analysis within the isogeometric analysis framework. *Computer Methods in Applied Mechanics and Engineering*, 273:100–118, may 2014.

[20] L F Martha, P A Wawrzynek, and A R Ingraffea. Arbitrary crack representation using solid modeling. *Engineering with Computers*, 9(2):63–82, 1993.

[21] V Chiaruttini, V Riolo, and F Feyel. Advanced remeshing techniques for complex 3D crack propagation. In *ICF13*, 2013.

[22] A R Khoei, M Eghbalian, H Moslemi, and H Azadi. Crack growth modeling via 3D automatic adaptive mesh refinement based on modified-SPR technique. *Applied Mathematical Modelling*, 37(1):357–383, 2013.

[23] M Schöllmann, M Fulland, and H.A Richard. Development of a new software for adaptive crack growth simulations in 3D structures. *Engineering Fracture Mechanics*, 70(2):249–268, jan 2003.

[24] A R Maligno, S Rajaratnam, S B Leen, and E J Williams. A three-dimensional (3D) numerical study of fatigue crack growth using remeshing techniques. *Engineering Fracture Mechanics*, 77(1):94–111, 2010.

[25] R Branco, F V Antunes, and J D Costa. A review on 3D-FE adaptive remeshing techniques for crack growth modelling. *Engineering Fracture Mechanics*, 141:170–195, jun 2015.

[26] N Sukumar, N Moës, B Moran, and T Belytschko. Extended finite element method for three-dimensional crack modelling. *International Journal for Numerical Methods in Engineering*, 48(11):1549–1570, 2000.

[27] N Sukumar, D L Chopp, E Béchet, and N Moës. Three-dimensional non-planar crack growth by a coupled extended finite element and fast marching method. *International Journal for Numerical Methods in Engineering*, 76(5):727–748, 2008.

[28] A Gravouil, N Moës, and T Belytschko. Non-planar 3D crack growth by the extended finite element and level sets-Part II: Level set update. *International Journal for Numerical Methods in Engineering*, 53(11):2569–2586, 2002.

[29] N Moës, A Gravouil, and T Belytschko. Non-planar 3D crack growth by the extended finite element and level sets-Part I: Mechanical model. *International Journal for Numerical Methods in Engineering*, 53(11):2549–2568, 2002.

[30] K Agathos, E Chatzi, S P. A. Bordas, and D Talaslidis. A well-conditioned and optimally convergent XFEM for 3D linear elastic fracture. *International Journal for Numerical Methods in Engineering*, 105(9):643–677, aug 2015.

[31] S P A Bordas and M Duflot. Derivative recovery and a posteriori error estimate for extended finite elements. *Computer Methods in Applied Mechanics and Engineering*, 196(35-36):3381–3399, 2007.

[32] E Wyart, M Duflot, D Coulon, P Martiny, T Pardoen, J.-F. Remacle, and F Lani. Substructuring FE–XFE approaches applied to three-dimensional crack propagation. *Journal of Computational and Applied Mathematics*, 215(2):626–638, 2008.

[33] P Krysl and T Belytschko. The element free Galerkin method for dynamic propagation of arbitrary 3-D cracks. *International Journal for Numerical Methods in Engineering*, 44(6):767–800, 1999.

[34] T Belytschko, Y Y Lu, and L Gu. Element-free Galerkin methods. *International Journal for Numerical Methods in Engineering*, 37(2):229–256, 1994.

[35] G Ventura, J X Xu, and T Belytschko. A vector level set method and new discontinuity approximations for crack growth by EFG. *International Journal for Numerical Methods in Engineering*, 54(6):923–944, 2002.

[36] T Rabczuk, S Bordas, and G Zi. On three-dimensional modelling of crack growth using partition of unity methods. *Computers & Structures*, 88(23-24):1391–1411, dec 2010.

[37] S P A Bordas, T Rabczuk, and G Zi. Three-dimensional crack initiation, propagation, branching and junction in non-linear materials by an extended meshfree method without asymptotic enrichment. *Engineering Fracture Mechanics*, 75(5):943–960, 2008.

[38] V P Nguyen, T Rabczuk, S Bordas, and M Duflot. Meshless methods: A review and computer implementation aspects. *Mathematics and Computers in Simulation*, 79(3):763–813, 2008.

[39] H Hong and J Chen. Derivations of Integral Equations of Elasticity. *Journal of Engineering Mechanics*, 114(6):1028–1044, 1988.

[40] J T Chen and H K Hong. Review of dual boundary element methods with emphasis on hypersingular integrals and divergent series. *Appl. Mech. Rev.*, 52(1):17–33, 1999.

[41] A Portela, M H Aliabadi, and D P Rooke. The dual boundary element method: Effective implementation for crack problems. *International Journal for Numerical Methods in Engineering*, 33(6):1269–1287, 1992.

[42] Y Mi and M H Aliabadi. Dual boundary element method for three-dimensional fracture mechanics analysis. *Engineering Analysis with Boundary Elements*, 10(2):161–171, 1992.

[43] A P Cisilino and M H Aliabadi. Dual boundary element assessment of three-dimensional fatigue crack growth. *Engineering Analysis with Boundary Elements*, 28(9):1157–1173, 2004.

[44] A P Cisilino and M H Aliabadi. Three-dimensional boundary element analysis of fatigue crack growth in linear and non-linear fracture problems. *Engineering Fracture Mechanics*, 63(6):713–733, aug 1999.

[45] V Leitão, M H Aliabadi, and D P Rooke. The dual boundary element formulation for elastoplastic fracture mechanics. *International Journal for Numerical Methods in Engineering*, 38(2):315–333, 1995.

[46] P Fedelinski, M H Aliabadi, and D P Rooke. The dual boundary element method in dynamic fracture mechanics. *Engineering Analysis with Boundary Elements*, 12(3):203–210, jan 1993.

[47] S C Mellings and J M W Baynham. Automatic Fatigue Crack Growth. In *ASME 2009 Pressure Vessels and Piping Conference*, pages 1513–1523. American Society of Mechanical Engineers, 2009.

[48] B J Carter, P A Wawrzynek, and A R Ingraffea. Automated 3-D crack growth simulation. *International journal for numerical methods in engineering*, 47(1-3):229–253, 2000.

[49] S Li, M E Mear, and L Xiao. Symmetric weak-form integral equation method for three-dimensional fracture analysis. *Computer Methods in Applied Mechanics and Engineering*, 151(3–4):435–459, 1998.

[50] A Frangi. Fracture propagation in 3D by the symmetric Galerkin boundary element method. *International Journal of Fracture*, 116(4):313–330, 2002.

[51] A Frangi, G Novati, R Springhetti, and M Rovizzi. 3D fracture analysis by the symmetric Galerkin BEM. *Computational Mechanics*, 28(3-4):220–232, 2002.

[52] G P Nikishkov, J H Park, and S N Atluri. SGBEM-FEM alternating method for analyzing 3D non-planar cracks and their growth in structural components. *Computer Modeling in Engineering & Sciences*, 2(3):401–422, 2001.

[53] A Frangi and G Novati. BEM–FEM coupling for 3D fracture mechanics applications. *Computational Mechanics*, 32(4-6):415–422, 2003.

[54] R W Macek and S A Silling. Peridynamics via finite element analysis. *Finite Elements in Analysis and Design*, 43(15):1169–1178, 2007.

[55] S A Silling and R B Lehoucq. Peridynamic Theory of Solid Mechanics. In *Advances in Applied Mechanics*, volume 44, pages 73–168. 2010.

[56] U Kaczmarczyk, M M Nezhad, and C Pearce. Three-dimensional brittle fracture: configurational-force-driven crack propagation. *International Journal for Numerical Methods in Engineering*, 97(7):531–550, 2014.

[57] R Simpson and J Trevelyan. A partition of unity enriched dual boundary element method for accurate computations in fracture mechanics. *Computer Methods in Applied Mechanics and Engineering*, 200(1–4):1–10, 2011.

[58] S R Chidgzey and A J Deeks. Determination of coefficients of crack tip asymptotic fields using the scaled boundary finite element method. *Engineering Fracture Mechanics*, 72(13):2019–2036, 2005.

[59] S R Chidgzey, J Trevelyan, and A J Deeks. Coupling of the boundary element method and the scaled boundary finite element method for computations in fracture mechanics. *Computers & Structures*, 86(11):1198–1203, 2008.

[60] S Natarajan, J Wang, C Song, and C Birk. Isogeometric analysis enhanced by the scaled boundary finite element method. *Computer Methods in Applied Mechanics and Engineering*, 283:733–762, jan 2015.

[61] R D Henshell and K G Shaw. Crack tip finite elements are unnecessary. *International Journal for Numerical Methods in Engineering*, 9(3):495–507, 1975.

[62] Y Mi and M H Aliabadi. Discontinuous crack-tip elements: Application to 3D boundary element method. *International Journal of Fracture*, 67(3):R67–R71, 1994.

[63] J Martinez and J Dominguez. On the use of quarter-point boundary elements for stress intensity factor computations. *International Journal for Numerical Methods in Engineering*, 20(10):1941–1950, 1984.

[64] S K Chan, I S Tuba, and W K Wilson. On the finite element method in linear fracture mechanics. *Engineering Fracture Mechanics*, 2(1):1–17, jul 1970.

[65] B L Karihaloo and Q Z Xiao. Accurate determination of the coefficients of elastic crack tip asymptotic field by a hybrid crack element with p-adaptivity. *Engineering Fracture Mechanics*, 68(15):1609–1630, 2001.

[66] N G Zamani and W Sun. A direct method for calculating the stress intensity factor in BEM. *Engineering Analysis with Boundary Elements*, 11(4):285–292, 1993.

[67] T K Hellen. On the method of virtual crack extensions. *International Journal for numerical methods in engineering*, 9(1):187–207, 1975.

[68] C G Hwang, P A Wawrzynek, and A R Ingraffea. On the virtual crack extension method for calculating the derivatives of energy release rates for a 3D planar crack of arbitrary shape under mode-I loading. *Engineering Fracture Mechanics*, 68(7):925–947, may 2001.

[69] B R Davis, P A Wawrzynek, and A R Ingraffea. 3-D simulation of arbitrary crack growth using an energy-based formulation – Part I: Planar growth. *Engineering Fracture Mechanics*, 115:204–220, 2014.

[70] B R Davis, P A Wawrzynek, and A R Ingraffea. Simulation of Arbitrary Mixed-Mode Crack Growth Using an Energy-Based Approach. In Jay Carroll and Samantha Daly, editors, *Fracture, Fatigue, Failure, and Damage Evolution, Volume 5*, Conference Proceedings of the Society for Experimental Mechanics Series, pages 1–9. Springer International Publishing, 2015.

[71] D Sutula, S P A Bordas, P Kerfriden, and A Barthelemy. Global Energy Minimization for Multi-crack Growth in Linear Elastic Fracture using the Extended Finite Element Methods. *11th. World Congress on Computational Mechanics (WCCM XI)*, Barcelona, 2014.

[72] R Krueger. Virtual crack closure technique: history, approach, and applications. *Applied Mechanics Reviews*, 57(2):109–143, 2004.

[73] J R Rice. A path independent integral and the approximate analysis of strain concentration by notches and cracks. *Journal of applied mechanics*, 35(2):379–386, 1968.

[74] M Stern, E B Becker, and R S Dunham. A contour integral computation of mixed-mode stress intensity factors. *International Journal of Fracture*, 12(3):359–368, 1976.

[75] J F Yau, S S Wang, and H T Corten. A mixed-mode crack analysis of isotropic solids using conservation laws of elasticity. *Journal of Applied Mechanics*, 47:333–341, 1980.

[76] P H Wen, M H Aliabadi, and D P Rooke. A contour integral for the evaluation of stress intensity factors. *Applied mathematical modelling*, 19(8):450–455, 1995.

[77] I Babuška and A Miller. The post-processing approach in the finite element method. Part 2: The calculation of stress intensity factors.

International Journal for numerical methods in Engineering, 20(6):1111–1129, 1984.

[78] J P Pereira and C A Duarte. Extraction of stress intensity factors from generalized finite element solutions. *Engineering Analysis with Boundary Elements*, 29(4):397–413, apr 2005.

[79] R H Rigby and M H Aliabadi. Mixed-mode J-integral method for analysis of 3D fracture problems using BEM. *Engineering Analysis with Boundary Elements*, 11(3):239–256, 1993.

[80] J H Chang and D J Wu. Stress intensity factor computation along a non-planar curved crack in three dimensions. *International Journal of Solids and Structures*, 44(2):371–386, 2007.

[81] G P Nikishkov and S N Atluri. Calculation of fracture mechanics parameters for an arbitrary three-dimensional crack, by the 'equivalent domain integral' method. *International Journal for Numerical Methods in Engineering*, 24(9):1801–1821, 1987.

[82] K N Shivakumar and I S Raju. An equivalent domain integral method for three-dimensional mixed-mode fracture problems. *Engineering Fracture Mechanics*, 42(6):935–959, 1992.

[83] O Huber, J Nickel, and G Kuhn. On the decomposition of the J-integral for 3D crack problems. *International Journal of Fracture*, 64(4):339–348, 1993.

[84] R H Rigby and M H Aliabadi. Decomposition of the mixed-mode J-integral—revisited. *International Journal of Solids and Structures*, 35(17):2073–2099, 1998.

[85] M Gosz and B Moran. An interaction energy integral method for computation of mixed-mode stress intensity factors along non-planar crack fronts in three dimensions. *Engineering Fracture Mechanics*, 69(3):299–319, 2002.

[86] A P Cisilino and J Ortiz. Boundary element analysis of three-dimensional mixed-mode cracks via the interaction integral. *Computer Methods in Applied Mechanics and Engineering*, 194(9-11):935–956, mar 2005.

[87] T J R Hughes, J A Cottrell, and Y Bazilevs. Isogeometric analysis: CAD, finite elements, NURBS, exact geometry and mesh refinement. *Computer Methods in Applied Mechanics and Engineering*, 194(39–41):4135–4195, 2005.

[88] I Akkerman, Y Bazilevs, V M Calo, T J R Hughes, and S Hulshoff. The role of continuity in residual-based variational multiscale modeling of turbulence. *Computational Mechanics*, 41(3):371–378, 2008.

[89] Y Bazilevs, V M Calo, Y Zhang, and T J R Hughes. Isogeometric Fluid–structure Interaction Analysis with Applications to Arterial Blood Flow. *Computational Mechanics*, 38(4-5):310–322, 2006.

[90] F Auricchio, L B da Veiga, C Lovadina, and A Reali. The importance of the exact satisfaction of the incompressibility constraint in nonlinear elasticity: mixed FEMs versus NURBS-based approximations. *Computer Methods in Applied Mechanics and Engineering*, 199(5–8):314–323, 2010.

[91] D J Benson, Y Bazilevs, M C Hsu, and T J R Hughes. Isogeometric shell analysis: The Reissner–Mindlin shell. *Computer Methods in Applied Mechanics and Engineering*, 199(5–8):276–289, 2010.

[92] M J Borden, C V Verhoosel, M A Scott, T J R Hughes, and C M Landis. A phase-field description of dynamic brittle fracture. *Computer Methods in Applied Mechanics and Engineering*, 217–220(0):77–95, 2012.

[93] Y Bazilevs, V M Calo, J A Cottrell, J A Evans, T J R Hughes, S Lipton, M A Scott, and T W Sederberg. Isogeometric analysis using T-splines. *Computer Methods in Applied Mechanics and Engineering*, 199(5–8):229–263, 2010.

[94] M A Scott, X Li, T W Sederberg, and T J R Hughes. Local refinement of analysis-suitable T-splines. *Computer Methods in Applied Mechanics and Engineering*, 213–216(0):206–222, 2012.

[95] J Deng, F Chen, X Li, C Hu, W Tong, Z Yang, and Y Feng. Polynomial splines over hierarchical T-meshes. *Graphical Models*, 70(4):76–86, jul 2008.

[96] T Dokken, T Lyche, and K F Pettersen. Polynomial splines over locally refined box-partitions. *Computer Aided Geometric Design*, 30(3):331–356, mar 2013.

[97] E De Luycker, D J Benson, T Belytschko, Y Bazilevs, and M C Hsu. X-FEM in isogeometric analysis for linear fracture mechanics. *International Journal for Numerical Methods in Engineering*, 87(6):541–565, 2011.

[98] S Ghorashi, N Valizadeh, and S Mohammadi. Extended isogeometric analysis for simulation of stationary and propagating cracks. *International Journal for Numerical Methods in Engineering*, 89(9):1069–1101, 2012.

[99] V P Nguyen, C Anitescu, S P A Bordas, and T Rabczuk. Isogeometric analysis: An overview and computer implementation aspects. *Mathematics and Computers in Simulation*, 117:89–116, jun 2015.

[100] N. Nguyen-Thanh, N. Valizadeh, M.N. Nguyen, H. Nguyen-Xuan, X. Zhuang, P. Areias, G. Zi, Y. Bazilevs, L. De Lorenzis, and T. Rabczuk. An extended isogeometric thin shell analysis based on Kirchhoff–Love theory. *Computer Methods in Applied Mechanics and Engineering*, 284:265–291, feb 2015.

[101] C V Verhoosel, M A Scott, R de Borst, and T J R Hughes. An isogeometric approach to cohesive zone modeling. *International Journal for Numerical Methods in Engineering*, 87(1-5):336–360, 2011.

[102] V P Nguyen, P Kerfriden, and S P A Bordas. Two- and three-dimensional isogeometric cohesive elements for composite delamination analysis. *Composites Part B: Engineering*, 60:193–212, apr 2014.

[103] M J Choi and S Cho. Isogeometric shape design sensitivity analysis of stress intensity factors for curved crack problems. *Computer Methods in Applied Mechanics and Engineering*, 279:469–496, sep 2014.

[104] A. Tambat and G. Subbarayan. Isogeometric enriched field approximations. *Computer Methods in Applied Mechanics and Engineering*, 245-246:1–21, oct 2012.

[105] K. Upreti, T. Song, A. Tambat, and G. Subbarayan. Algebraic distance estimations for enriched isogeometric analysis. *Computer Methods in Applied Mechanics and Engineering*, 280:28–56, oct 2014.

[106] J W Jeong, H S Oh, S Kang, and H Kim. Mapping techniques for isogeometric analysis of elliptic boundary value problems containing singularities. *Computer Methods in Applied Mechanics and Engineering*, 254:334–352, feb 2013.

[107] H S Oh, H Kim, and J W Jeong. Enriched isogeometric analysis of elliptic boundary value problems in domains with cracks and/or corners. *International Journal for Numerical Methods in Engineering*, 97(3):149–180, jan 2014.

[108] L Liu, Y Zhang, T J R Hughes, M A Scott, and T W Sederberg. Volumetric T-spline construction using Boolean operations. *Engineering with Computers*, 30(4):425–439, 2013.

[109] G Xu, B Mourrain, R Duvigneau, and A Galligo. Analysis-suitable volume parameterization of multi-block computational domain in isogeometric applications. *Computer-Aided Design*, 45(2):395–404, feb 2013.

[110] G Xu, B Mourrain, R Duvigneau, and A Galligo. Constructing analysis-suitable parameterization of computational domain from

CAD boundary by variational harmonic method. *Journal of Computational Physics*, 252:275–289, nov 2013.

[111] M A Scott, R N Simpson, J A Evans, S Lipton, S P A Bordas, T J R Hughes, and T W Sederberg. Isogeometric boundary element analysis using unstructured T-splines. *Computer Methods in Applied Mechanics and Engineering*, 254(0):197–221, 2013.

[112] R N Simpson, S P A Bordas, J Trevelyan, and T Rabczuk. A two-dimensional Isogeometric Boundary Element Method for elastostatic analysis. *Computer Methods in Applied Mechanics and Engineering*, 209–212(0):87–100, 2012.

[113] R N Simpson, M A Scott, M Taus, D C Thomas, and H Lian. Acoustic isogeometric boundary element analysis. *Computer Methods in Applied Mechanics and Engineering*, page accepted, 2013.

[114] J Gu, J Zhang, and G Li. Isogeometric analysis in BIE for 3-D potential problem. *Engineering Analysis with Boundary Elements*, 36(5):858–865, 2012.

[115] K Li and X Qian. Isogeometric analysis and shape optimization via boundary integral. *Computer-Aided Design*, 43(11):1427–1437, 2011.

[116] C Politis, A I Ginnis, P D Kaklis, K Belibassakis, and C Feurer. An isogeometric BEM for exterior potential-flow problems in the plane. In *2009 SIAM/ACM Joint Conference on Geometric and Physical Modeling*, SPM '09, pages 349–354, New York, NY, USA, 2009. ACM.

[117] A I Ginnis, K V Kostas, C G Politis, P D Kaklis, K A Belibassakis, Th.P. Gerostathis, M.A. Scott, and T.J.R. Hughes. Isogeometric boundary-element analysis for the wave-resistance problem using T-splines. *Computer Methods in Applied Mechanics and Engineering*, 279:425–439, sep 2014.

[118] K V Kostas, A I Ginnis, C G Politis, and P D Kaklis. Ship-hull shape optimization with a T-spline based BEM–isogeometric solver. *Computer Methods in Applied Mechanics and Engineering*, 284:611–622, feb 2015.

[119] M J Peake, J Trevelyan, and G Coates. Extended isogeometric boundary element method (XIBEM) for two-dimensional Helmholtz problems. *Computer Methods in Applied Mechanics and Engineering*, 259(0):93–102, 2013.

[120] M.J. Peake, J. Trevelyan, and G. Coates. Extended isogeometric boundary element method (XIBEM) for three-dimensional medium-wave acoustic scattering problems. *Computer Methods in Applied Mechanics and Engineering*, 284:762–780, feb 2015.

[121] G Beer, B Marussig, and J Zechner. A simple approach to the numerical simulation with trimmed CAD surfaces. *Computer Methods in Applied Mechanics and Engineering*, 285:776–790, mar 2015.

[122] Y Wang, D J Benson, and A P Nagy. A multi-patch nonsingular isogeometric boundary element method using trimmed elements. *Computational Mechanics*, 56(1):173–191, 2015.

[123] B Marussig, J Zechner, G Beer, and T P Fries. Fast isogeometric boundary element method based on independent field approximation. *Computer Methods in Applied Mechanics and Engineering*, 284:458–488, 2015.

[124] M Feischl, G Gantner, and D Praetorius. Reliable and efficient a posteriori error estimation for adaptive {IGA} boundary element methods for weakly-singular integral equations. *Computer Methods in Applied Mechanics and Engineering*, 290:362–386, 2015.

[125] A Aimi, M Diligenti, M L Sampoli, and A Sestini. Isogemetric analysis and symmetric Galerkin BEM: A 2D numerical study. *Applied Mathematics and Computation*, pages –, 2015.

[126] M Taus, G J Rodin, and T J R Hughes. Isogeometric analysis of boundary integral equations. *ICES report 15-12*, 2015.

[127] M Guiggiani, G Krishnasamy, T J Rudolphi, and F J Rizzo. A General Algorithm for the Numerical Solution of Hypersingular Boundary Integral Equations. *Journal of Applied Mechanics*, 59(3):604–614, 1992.

[128] M Guiggiani. Formulation and numerical treatment of boundary integral equations with hypersingular kernels. *Singular integrals in boundary element methods*, pages 85–124, 1998.

[129] L Piegl and W Tiller. The NURBS book. *springer*, 1995.

[130] J C F Telles. A self-adaptive co-ordinate transformation for efficient numerical evaluation of general boundary element integrals. *International Journal for Numerical Methods in Engineering*, 24(5):959–973, 1987.

[131] T J Rudolphi. The use of simple solutions in the regularization of hypersingular boundary integral equations. *Math. Comput. Model.*, 15(3-5):269–278, jan 1991.

[132] Y Liu and T J Rudolphi. Some identities for fundamental solutions and their applications to weakly-singular boundary element formulations. *Engineering Analysis with Boundary Elements*, 8(6):301–311, 1991.

[133] E Lutz, A R Ingraffea, and L J Gray. Use of 'simple solutions' for boundary integral methods in elasticity and fracture analysis. *International Journal for Numerical Methods in Engineering*, 35(9):1737–1751, 1992.

[134] Y X Mukherjee, K Shah, and S Mukherjee. Thermoelastic fracture mechanics with regularized hypersingular boundary integral equations. *Engineering Analysis with Boundary Elements*, 23(1):89–96, 1999.

[135] M Tanaka, V Sladek, and J Sladeck. Regularization Techniques Applied to Boundary Element Methods. *Applied Mechanics Reviews*, 47(10):457–499, 1994.

[136] J M Melenk and I Babuška. The partition of unity finite element method: Basic theory and applications. *Computer Methods in Applied Mechanics and Engineering*, 139(1-4):289–314, 1996.

[137] S Bordas, P V Nguyen, C Dunant, A Guidoum, and H Nguyen-Dang. An extended finite element library. *International Journal for Numerical Methods in Engineering*, 71(6):703–732, 2007.

[138] J J Ródenas, O A González-Estrada, J E Tarancón, and F J Fuenmayor. A recovery-type error estimator for the extended finite element method based on singular+smooth stress field splitting. *International Journal for Numerical Methods in Engineering*, 76(4):545–571, 2008.

[139] M Duflot and S P A Bordas. A posteriori error estimation for extended finite elements by an extended global recovery. *International Journal for Numerical Methods in Engineering*, 76(8):1123–1138, 2008.

[140] O A González-Estrada, J J Ródenas, E Nadal, S P A Bordas, and P Kerfriden. Equilibrated patch recovery for accurate evaluation of upper error bounds in quantities of interest. Adaptive Modeling and Simulation. *Proceedings of V ADMOS*, 2011.

[141] K M Liew, Y Cheng, and S Kitipornchai. Analyzing the 2D fracture problems via the enriched boundary element-free method. *International Journal of Solids and Structures*, 44(11–12):4220–4233, 2007.

[142] F Auricchio, L B D Veiga, T J R Hughes, A Reali, and G Sangalli. Isogeometric collocation methods. *Mathematical Models and Methods in Applied Sciences*, 20(11):2075–2107, 2010.

[143] P A Martin and F J Rizzo. Hypersingular integrals: how smooth must the density be? *International Journal for Numerical Methods in Engineering*, 39(4):687–704, 1996.

[144] J W Eischen. An improved method for computing the J2 integral. *Engineering Fracture Mechanics*, 26(5):691–700, 1987.

[145] F Erdogan and G Sih. On the crackextension in plates under plane loading and transverse shear. *Journal of Basic Engineering*, 85:519–527, 1963.

[146] R LaGreca, M Daniel, and A Bac. Local deformation of NURBS curves. *Mathematical methods for curves and surfaces, Tromso 2004*, pages 243–252, 2005.

[147] A Paluszny and R W Zimmerman. Numerical fracture growth modeling using smooth surface geometric deformation. *Engineering Fracture Mechanics*, 108(0):19–36, 2013.

[148] H M Westergaard. Bearing pressures and cracks. *Journal of Applied Mechanics*, 6:A49–A53, 1939.

[149] D J Smith, M R Ayatollahi, and M J Pavier. The role of T-stress in brittle fracture for linear elastic materials under mixed-mode loading. *Fatigue & Fracture of Engineering Materials & Structures*, 24(2):137–150, 2001.

[150] A Sutradhar and G H Paulino. Symmetric Galerkin boundary element computation of T-stress and stress intensity factors for mixed-mode cracks by the interaction integral method. *Engineering Analysis with Boundary Elements*, 28(11):1335–1350, 2004.

[151] B Cotterell and J R Rice. Slightly curved or kinked cracks. *International Journal of Fracture*, 16(2):155–169, 1980.

[152] A R Ingraffea and M Grigoriu. Probabilistic fracture mechanics: A validation of predictive capability. *Department of Structure Engineering, Cornell University*, Rep. 90-8, 1990.

[153] Y J Wang and D J Benson. Multi-patch nonsingular isogeometric boundary element analysis in 3D. *Computer Methods in Applied Mechanics and Engineering*, 293:71–91, aug 2015.

[154] J Rong, L Wen, and J Xiao. Efficiency improvement of the polar coordinate transformation for evaluating BEM singular integrals on

curved elements. *Engineering Analysis With Boundary Elements*, 38:83–93, 2014.

[155] S Osher and R Fedkiw. *Level set methods and dynamic implicit surfaces*, volume 153. Springer Science & Business Media, 2006.

[156] N Moës, M Cloirec, P Cartraud, and J F Remacle. A computational approach to handle complex microstructure geometries. *Computer Methods in Applied Mechanics and Engineering*, 192(28-30):3163–3177, jul 2003.

[157] T J Barth and J A Sethian. Numerical Schemes for the Hamilton–Jacobi and Level Set Equations on Triangulated Domains. *Journal of Computational Physics*, 145(1):1–40, sep 1998.

[158] D L Chopp and N Sukumar. Fatigue crack propagation of multiple coplanar cracks with the coupled extended finite element/fast marching method. *International Journal of Engineering Science*, 41(8):845–869, may 2003.

[159] T P Fries and M Baydoun. Crack propagation with the extended finite element method and a hybrid explicit–implicit crack description. *International Journal for Numerical Methods in Engineering*, 89(12):1527–1558, 2012.

[160] A Paluszny and R W Zimmerman. Numerical simulation of multiple 3D fracture propagation using arbitrary meshes. *Computer Methods in Applied Mechanics and Engineering*, 200(9-12):953–966, feb 2011.

[161] J Garzon, P O'Hara, C A Duarte, and W G Buttlar. Improvements of explicit crack surface representation and update within the generalized finite element method with application to three-dimensional crack coalescence. *International Journal for Numerical Methods in Engineering*, 97(4):231–273, 2014.

[162] L A de Lacerda and L C Wrobel. Dual boundary element method for axisymmetric crack analysis. *International Journal of Fracture*, 113(3):267–284, 2002.

[163] M K Kassir and G Sih. Three-Dimensional Stress Distribution Around an Elliptical Crack Under Arbitrary Loadings. *Journal of Applied Mechanics*, 33(3):601–611, 1966.

[164] T N Farris and M Liu. Boundary element crack closure calculation of three-dimensional stress intensity factors. *International journal of fracture*, 60(1):33–47, 1993.

[165] N Sukumar, D L Chopp, and B Moran. Extended finite element method and fast marching method for three-dimensional fatigue crack propagation. *Engineering Fracture Mechanics*, 70(1):29–48, jan 2003.

[166] U S Product Data Association and Others. Initial Graphics Exchange Specification IGES 5.3. *ANSI. Retrieved July*, 12:2008, 1996.

[167] R Schmidt, R Wüchner, and K U Bletzinger. Isogeometric analysis of trimmed NURBS geometries. *Computer Methods in Applied Mechanics and Engineering*, 241-244:93–111, oct 2012.

[168] H J Kim, Y D Seo, and S K Youn. Isogeometric analysis for trimmed CAD surfaces. *Computer Methods in Applied Mechanics and Engineering*, 198(37-40):2982–2995, aug 2009.

[169] H J Kim, Y D Seo, and S K Youn. Isogeometric analysis with trimming technique for problems of arbitrary complex topology. *Computer Methods in Applied Mechanics and Engineering*, 199(45-48):2796–2812, nov 2010.

[170] R Sevilla, S Fernández-Méndez, and A Huerta. NURBS-enhanced finite element method (NEFEM). *International Journal for Numerical Methods in Engineering*, 76(1):56–83, 2008.

[171] T Rabczuk, G Zi, A Gerstenberger, and W A Wall. A new crack tip element for the phantom node method with arbitrary cohesive cracks. *International Journal for Numerical Methods in Engineering*, 75(5):577–599, jul 2008.

[172] A Hansbo and P Hansbo. A finite element method for the simulation of strong and weak discontinuities in solid mechanics. *Computer Methods in Applied Mechanics and Engineering*, 193(33-35):3523–3540, aug 2004.

[173] J. Mergheim, E. Kuhl, and P. Steinmann. A finite element method for the computational modelling of cohesive cracks. *International Journal for Numerical Methods in Engineering*, 63(2):276–289, may 2005.

[174] T Chau-Dinh, G Zi, P S Lee, T Rabczuk, and J H Song. Phantom-node method for shell models with arbitrary cracks. *Computers & Structures*, 92-93:242–256, feb 2012.

[175] W Ye. A new transformation technique for evaluating nearly singular integrals. *Computational mechanics*, 42(3):457–466, 2008.

[176] K Hayami and H Matsumoto. A numerical quadrature for nearly singular boundary element integrals. *Engineering Analysis with Boundary Elements*, 13(2):143–154, jan 1994.

[177] K Hayami. Variable transformations for nearly singular integrals in the boundary element method. *Publications of the Research Institute for Mathematical Sciences*, 41(4):821–842, 2005.

[178] I S Raju and J C Newman Jr. Three dimensional finite-element analysis of finite-thickness fracture specimens. *NASA TN D-8414*, 1977.

[179] J Zechner, B Marussig, G Beer, and T P Fries. The Isogeometric Nystr\" om Method. *arXiv preprint arXiv:1506.03914*, 2015.